DEPARTMENT OF PHYSICS
UNIVERSITY OF JYVÄSKYLÄ
RESEARCH REPORT No. 8/2016

FABRICATION, ELECTRICAL CHARACTERIZATION AND 1/F NOISE STUDY OF SUBMICRON-SIZED SUPERCONDUCTING TUNNEL JUNCTIONS

BY
JUHANI JULIN

Academic Dissertation
for the Degree of
Doctor of Philosophy

To be presented, by permission of the
Faculty of Mathematics and Science
of the University of Jyväskylä,
for public examination in Auditorium FYS1 of the
University of Jyväskylä on August 5, 2016
at 12 o'clock noon

Jyväskylä, Finland
August, 2016

Preface

The work presented in this thesis has been carried out at the Department of Physics and Nanoscience Center at the University of Jyväskylä.

I wish to thank my supervisor Professor Ilari Maasilta for the opportunity to work with him in his group, his guidance has been of the most important in completing this work. I am grateful to all present and former members of our group and other people I had pleasure to work with. Special thanks to Dr. Saumyadip Chaudhuri, Mr. Zhuoran Geng, Dr. Tero Isotalo, Dr. Panu Koppinen, Dr. Minna Nevala, Ms. Yaolan Tian and Mr. Andrii Torgovkin for collaboration and fruitful discussions. Technical support from the laboratory engineers Dr. Kimmo Kinnunen and Mr. Tarmo Suppula has been essential. Financial support from the Finnish Cultural Foundation is acknowledged.

Finally, my warmest gratitude to my love, Pauliina, for the all.

Jyväskylä, August 2016

Juhani Julin

Abstract

Julin, Juhani Kristian
Fabrication, electrical characterization and $1/f$ noise study of submicron-sized superconducting tunnel junctions
Jyväskylä: University of Jyväskylä, 2016
(Research report/Department of Physics, University of Jyväskylä,
ISSN 0075-465X; 8/2016)
ISBN 978-951-39-6678-2 (paper copy)
ISBN 978-951-39-6679-9 (online PDF)
diss.

This thesis presents results focused on fabrication and electrical characterization of superconducting tunnel junctions and Josephson junctions, e.g. measuring the current–voltage response and $1/f$ noise from different samples at different temperatures. Junctions were fabricated inside a vacuum chamber where metal evaporation through a resist mask was used to create submicron-sized junctions. The tunneling barrier was common between all different samples, i.e. in-situ oxidized aluminium between the metal depositions.

Different material combinations were used, e.g. Al–AlO_x–Al, Al–AlO_x–Al:Mn and Al–AlO_x–Nb. The manganese doping in aluminium (Al:Mn) suppresses the superconductivity making the Al:Mn parts normal, while pure aluminium is superconducting, creating a normal metal–insulator–superconductor (NIS) device.

The qualities of junctions were improved, if possible, by vacuum thermal annealing at 400 °C, which was found both to stabilize aluminium and aluminium–manganese based junctions and to reduce the characteristic $1/f$ noise in them. These results are desired, since for most applications it is important to have a junction with stable parameters over long time and $1/f$ noise is limiting the sensitivity of many devices. However, the procedure is not for granted, since most other NIS material combinations didn't survive the annealing treatment.

We studied Al–AlO_x–Nb junctions at cryogenic temperatures ($\approx$ 100 mK) either as an SIS' device, or as an NIS device by suppressing the superconductivity of aluminium with magnetic field, and observed excess sub-gap current, which could not be explained by standard tunneling theory with the Dynes model.

Keywords Low temperature physics, nanofabrication, tunnel junctions, Josephson junctions, NIS/SIS tunneling, supercurrent, superconductor, cryogenics, noise, $1/f$ noise, annealing, negative absolute resistance, niobium-based superconducting devices

FIGURE 1 University of Jyväskylä, Department of Physics. The photo taken by the author sometime around 2004-2005, soon after opening of the brand new NanoScience Center and the beginning of the author's undergraduate studies.

Author's address Juhani Julin
Department of Physics
Nanoscience Center
University of Jyväskylä
Finland

Supervisor Professor Ilari Maasilta
Department of Physics
Nanoscience Center
University of Jyväskylä
Finland

Reviewers Associate Professor Tapio Niemi
Optoelectronics Research Centre
Tampere University of Technology
Finland

Dr. Joonas Peltonen
Department of Applied Physics
Aalto University School of Science
Finland

Opponent Dr. Clemens Winkelmann
Université Grenoble Alpes / Institut Néel
France

List of Publications

The main results of this thesis have been reported in the following articles:

A.I. J.K. JULIN, P.J. KOPPINEN AND I.J. MAASILTA, *Reduction of low-frequency 1/f noise in Al–AlO_x–Al tunnel junctions by thermal annealing*. Appl. Phys. Lett. **97**, 152501 (2010).

A.II. J.K. JULIN, S. CHAUDHURI, M. LAITINEN, T. SAJAVAARA AND I.J. MAASILTA, *Stability, sub-gap current, $1/f$ noise, and elemental depth profiling of annealed Al:Mn–AlO_x–Al normal metal-insulator-superconducting tunnel junctions*. Submitted for publication.

A.III. J.K. JULIN AND I.J. MAASILTA, *Applications and non-idealities of submicron Al–AlO_x–Nb tunnel junctions*. Superconductor Science and Technology, in press.

A.IV. J. GOVENIUS, R.E. LAKE, K.Y. TAN, V. PIETILÄ, J.K. JULIN, I.J. MAASILTA, P. VIRTANEN AND M. MÖTTÖNEN., *Microwave nanobolometer based on proximity Josephson junctions*. Phys. Rev. B **90**, 064505 (2014).

Author's contribution

The author of this thesis has written the first drafts of articles A.I. - A.III., and fabricated, measured and analyzed all the samples they involve. The author has participated in maintaining and repairing the ^{3}He–^{4}He dilution fridge cryostats used in measurements, as well as building other experimental setups. The author has written a code using Octave language to theoretically simulate current–voltage response in NIS and SIS' junctions. The author fabricated the Nb–AuPd–Nb SNS junctions used in article A.IV.

Other publications to which the author has contributed

B.I. S. RAHAMAN, V.-V. ELOMAA, T. ERONEN, J. HAKALA, A. JOKINEN, J. JULIN, A. KANKAINEN, A. SAASTAMOINEN, J. SUHONEN, C. WEBER, J. ÄYSTÖ, *Q values of the 76Ge and 100Mo double-beta decays* . Physics Letters B, Volume 662, Issue 2, p. 111-116.

Contents

Chapter 1

Introduction

1.1 Superconductivity

The discovery of superconductivity in 1911 by Heike Kamerlingh Onnes opened an area of new physics whose real nature remained a mystery for a long time. Even though its name "super-conductivity" stands for perfect conductance, the real phenomenon is much more than zero resistivity, but also perfect diamagnetism and realization of macroscopic quantum mechanics [1].

The perfect diamagnetism arises from a screening current that as a supercurrent can permanently counteract an external magnetic field that tries to penetrate inside a superconductor. Only if a critical field is exceeded will the superconductor turn into a normal state and the field will penetrate. Because this so-called Meissner effect is an equilibrium phenomenon, it means that the field not only cannot penetrate, but is expelled when a superconductor is cooled below its critical temperature (Fig. 1.1).

However, not all superconductors respond to the magnetic field the same way. Most elemental superconductors (except Nb, Tc, and V), for example aluminium, are of type I, meaning that they have one specific critical magnetic field below which they show superconducting behavior [1]. Type II superconductors, e.g. all high temperature superconductors, on the other hand, have two critical magnetic field values [2]. Below the lower one, the superconductor is like type I, a perfect diamagnet without any field in its interior. Above the first critical field, but below the second, there is a phase where the external magnetic field has penetrated through the superconductor as quantized vortices, causing small normal state cores. This phase still shows perfect conductivity as long as the vortices are stationary. However, thin films of type I superconductors (e.g. Al) show type II behavior (intermediate state) in sufficiently high magnetic fields [3].

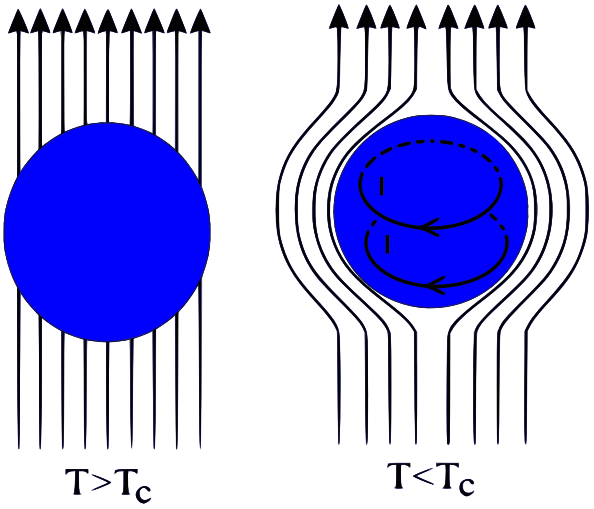

FIGURE 1.1 Below its transitions temperature T_C, superconductor completely expels the external magnetic field from its interior.

Vortex pinning is a phenomenon where the vortices are trapped or pinned into defects [4]. This flux trapping can invisibly anchor a permanent magnet and a superconductor to a specific distance as seen in Fig. 1.2.

After numerous experimental discoveries (e.g. charge carriers have a charge of $2e$, the Meissner effect, energy gap, critical temperature and magnetic field, heat capacity, isotope effect) [1] which gave theorists "hints" about the physics behind the obscure superconductivity, in the 1950's the theoretical research finally culminated in the Bardeen-Cooper-Schrieffer (BCS) theory introduced in 1957 [5]. It explained superconductivity with a microscopic theory based on phonon-mediated attractive interaction between two electrons creating a Cooper pair.

Two negatively charged electrons definitely don't like each other, so how can they pair up? Despite the pure quantum mechanical origin of superconductivity, one can try to get a rough classical idea of it by imagining electrons moving through a lattice of positive ions. If temperature is high, the lattice is vibrating heavily, and there is mostly scattering between the electrons and the lattice leading to resistance. At lower temperatures, the lattice vibrations are weaker and electrons can travel through the lattice more freely, leading to the lower resistance commonly seen in metals at colder temperatures. But superconductivity is not a low resistance, it has exactly zero resistance. That requires some sort of collective motion of the carriers, without scattering at all. The collective state, the BCS ground state, forms only at the coldest temperatures. It consists of a rigid collection of Cooper pairs forming a macroscopic coherent quantum state. This condensed quantum mechanical ground state is responsible for the strange properties of superconductivity.

The formation of a single Cooper pair can then be explained as follows: as the

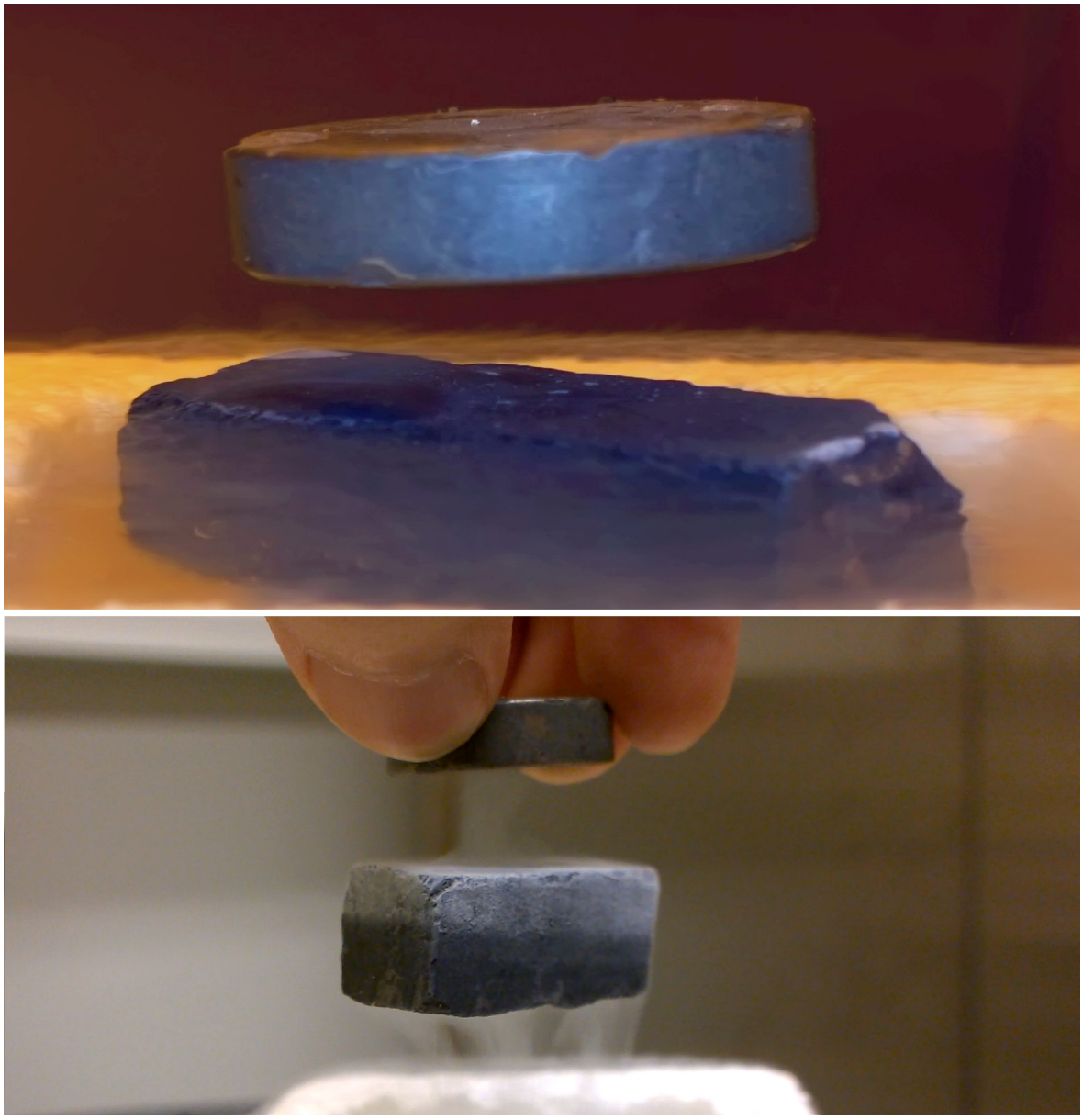

FIGURE 1.2 A permanent magnet (above) is magnetically coupled to a YBCO high temperature superconductor via flux trapping. The pinned field though the vortices of type II superconductor governs the distance between the objects. The magnet is not only levitating, but holding the distance when pulled to any direction. The experiment was done and photographed by the author.

first electron moves through the lattice it is attracting positively charged ions around it. The ions are vastly heavier than the electron so they don't respond quickly, but still they do move and create a bit more positively charged region behind the first electron. That charge will attract the second electron, hence leading to effective attraction and the pairing (see Fig. 1.3). Obviously this only works if the temperature

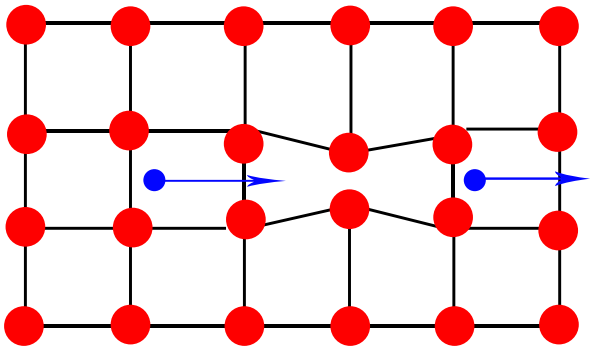

FIGURE 1.3 The attractive force between electrons in a Cooper pair is via lattice interaction. The first electron moving to the right is pulling positively charged nuclei towards it creating a slightly more positive charge concentration that will attract the second electron.

is low enough for superconductivity, i.e. the thermal energies won't mess up this fragile scene.

The pairing of electrons creates an energy gap, the energy required to break a Cooper pair. Obviously this pairing energy is very weak ($\approx$ meV range) and thermal energies can easily exceed it, thus superconductivity typically only exists at low temperatures. With different, stronger pairing mechanisms, high temperature superconductors can have critical temperatures exceeding 200 Kelvin [6].

1.2 Tunnel Junctions

This thesis concentrates on electrical properties seen in tunnel junctions, mainly in superconducting tunnel junctions. Tunneling is a purely quantum mechanical phenomenon emerging from a wave function nature of a particle, where there is a finite probability for the particle's wave function to extend on the other side of a classically impenetrable barrier (see Fig. 1.4). The square of the wave function represents the probability of the particle to be found at a specific location, giving thus the probabilities for tunneling events [7].

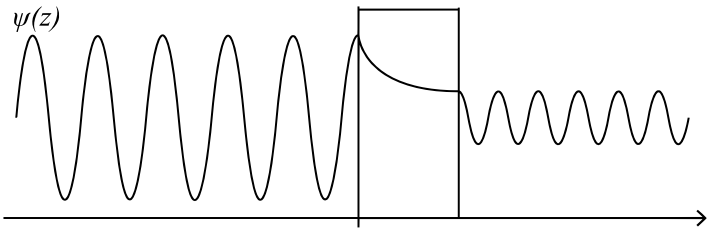

FIGURE 1.4 The quantum mechanical wave function $\Psi(z)$ of a particle is continuous also on the far side of a barrier making tunneling possible.

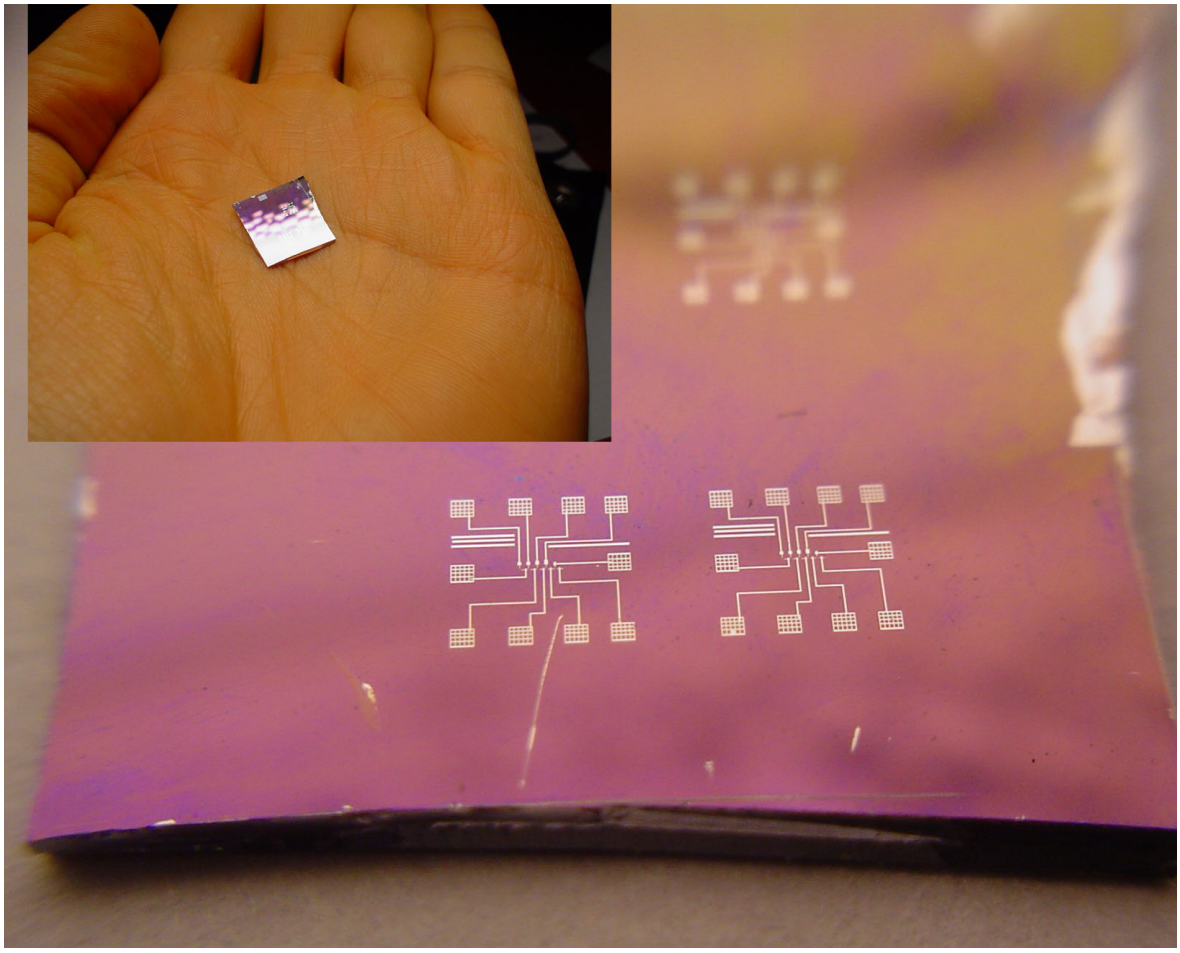

FIGURE 1.5 The very first chip the author has made. The "large" structures seen on the surface are bonding pads, the real tunnel junction is located in the middle where the wires converge and is invisible to the naked eye. The linewidth of the small structure is about the same as the wavelengths of visible light.

This quantum tunneling is classically incomprehensible, there is no large scale analogue seen in everyday life. There is no conventional "tunnel" through the barrier, and the tunneling event is not due to any high force impact, like a shot bullet penetrating though a target, but instead, in quantum tunneling the barrier is not destroyed or damaged.

Tunneling is actually quite a common phenomenon. In the microscopic world, e.g. in nuclear and particle physics, tunneling happens all the time, the fusion energy (the Sun) relies on tunneling [8], reverse bias current in diodes (Zener breakdown) is due to tunneling [9], and there are even dedicated tunneling diodes [9].

Transistors in modern microprocessors have got small enough that unwanted tunneling events (leakage current) are a significant issue in designing even smaller microelectronics [10]. On the other hand, SSD drives, memory cards and other non-

volatile flash storages are based on floating-gate MOSFETs where quantum tunneling is one method used to store information, i.e. pushing electrons into the isolated gate electrode. If there are excess electrons in the floating gate in a field-effect transistor, the negative charge shields the channel between the source and drain, and that can be measured without altering the charge trapped in the floating gate [11].

In this thesis, the tunneling phenomenon is utilized in tunnel junctions. A tunnel junction is simply a device where the conductivity is suppressed by a thin insulator (thickness preferably around ≈ 1 nm) between two electrodes. The tunneling area is typically also rather small, since the larger the area the more likely there are pinholes that bypass tunneling by ohmic contact. A photo of a silicon chip containing a set of tunnel junctions is illustrated in Fig. 1.5.

A practical way to create a nanoscale tunnel junction is by evaporating metal on a substrate, oxidizing its surface to create a thin tunneling barrier from the insulating oxide, and finalizing the junction by evaporating a second metal. Aluminium is commonly, and also here, used as the first metal because it is easily oxidized to create a high quality barrier.

Such a junction will have a significantly higher resistance than a metal wire of the same width without a junction would have, due to the tunneling resistance, which arises due to the small barrier penetration probability. The temperature dependence is also opposite compared to metals, because more electrons can tunnel at higher temperatures. Thus the tunneling rate decreases and resistance increases as the temperature drops (measured difference illustrated in Fig. 1.6). A relatively high tunneling resistance and a negative temperature coefficient are good indications of a working tunnel junction.

Two superconductors can also be coupled by a weak link (e.g. a normal metal or a thin insulator), thus creating a superconducting tunnel junction, a Josephson junction. Quasiparticle (electron) tunneling is still present, but the tunneling won't take place until there is enough energy to overcome the energy gap, i.e. break the Cooper pairs to Bogoliubov quasiparticles [1].

Cooper pairs can also tunnel through the barrier. Unlike in a conventional conductivity where voltage (electric field) drives current, in a Josephson junction there is a supercurrent even at zero bias voltage. This is called the DC Josephson effect, which predicts a DC current

$$I(t) = I_C \sin(\phi(t)), \tag{1.1}$$

where I_C is the critical current and $\phi(t)$ is the phase difference of the wave function across the junction of the superconducting condensate [12]. When voltage

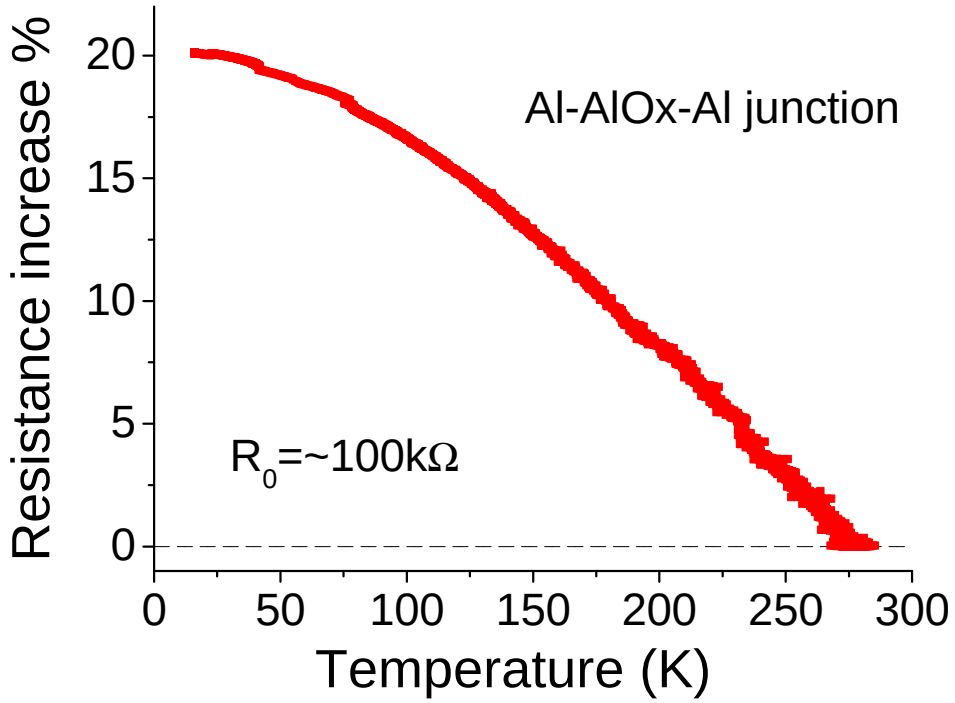

FIGURE 1.6 Measured increase of tunneling resistance as a function of temperature for an Al–AlO_x–Al sample.

biased, the phase will change according to equation

$$U(t) = \frac{\hbar}{2e}\frac{\partial \phi}{\partial t}. \tag{1.2}$$

This is the AC Josephson effect; if the voltage U is constant the phase will vary linearly, thus leading to an AC current of amplitude I_C and a frequency $f = 2eU/h$ from Eq. 1.1. This phenomenon can be used for example in metrology in defining the unit of voltage [13].

The requirement of low temperatures and thus the need of cryogenic coolers prevents normal-life household applications, but tunnel junctions have been found useful in many advanced devices. The strong temperature dependence in current–voltage characteristics of a normal metal–insulator–superconductor (NIS) junction makes it an accurate low temperature thermometer and the energy gap allows selective tunneling that can be used in solid state coolers [14]. A small isolated island between two serially connected normal state normal metal–insulator–normal metal (NIN) junctions will exhibit Coulomb blockade, whose electrical characteristics can be written to depend only on measured voltage and temperature, which is a primary thermometer [15]. By adding a gate electrode one can control the current at a single electron level, making a single-electron transistor [16]. A DC SQUID (superconducting quantum interference device) is a sensitive magnetometer that relies on

a behavior of supercurrent in a loop with two Josephson junctions in the presence of magnetic field [17]. An electromagnetic radiation sensor can be made out of a junction DC current biased close to the gap, where photon assisted tunneling will trigger the conductivity [18].

1.3 Quantum bit (Qubit)

A really fascinating application for superconducting tunnel junctions is in quantum computation [19]. Ordinary computers use binary electronics, where the information is stored and processed in bits. A bit can be either 0 or 1, which is usually realized as an amplitude (voltage) of a waveform, that can be easily further processed in CPU and stored in memory banks [20]. A quantum bit, qubit, is a superposition of two quantum states $|0\rangle$ and $|1\rangle$. According to quantum mechanics, an isolated system is in a superposed quantum state of all possible solutions until it is observed (measured) and it collapses to a single eigenstate. In a quantum computer n number of qubits are connected together to have a superposition of 2^n possible different states simultaneously. Dedicated algorithms dictate the time evolution of the system that can be used in calculations. Modern "classical" processors run at several GHz frequencies, but the increase of a clock rate is not possible forever because of limiting physical phenomena, e.g. a finite switching time of gates. Classical computers are indeed fast in serial arithmetics, but some problems could benefit of simultaneous parallel calculations in quantum computer.

In principle, any isolated 2-state quantum mechanical system can work as a qubit, but the challenge is to connect qubits together, initialization, and implementing a readout of the quantum state. Also, the quantum coherence must be maintained during the computation time, since any external influence on the quantum state causes decoherence (especially $1/f$ noise [21]). Superconductivity as a macroscopic quantum mechanical phenomenon is a promising method to construct a qubit, especially when included with Josephson junctions [22]. The non-linearity of the junction is needed to restrict the qubit to only two states from a system comprising of many states. Also, there exists a known technology for nanofabrication methods, coupling multiple qubits to a quantum register, and the number of qubits can be scaled up relatively straightforwardly.

Qubits based on superconducting Josephson junctions can be commonly realized in three different ways each possessing a different physical observable as quantum information state [23], see Fig. 1.7.

A phase qubit is current biased just below the critical current and operates in the zero voltage state. The quantum energy state is measured with an applied

microwave pulse, that will excite a transition to the next energy state. If the qubit is in the $|1\rangle$ state the next $|2\rangle$ state is a voltage state, i.e. switch to normal.

A flux qubit is a loop interrupted by one or more Josephson junctions. A magnetic flux Φ through a superconducting loop is quantized due to the superconductor's wave function Ψ to be continuous over the loop. When externally applied a magnetic flux $\Phi_e = \Phi_0/2$, where the Φ_0 is the flux quantum, the generally asymmetrical potential becomes symmetrical facilitating two basic states of the device. The quantum mechanical state is a superposition from flux up $|\uparrow\rangle$ and flux down $|\downarrow\rangle$. A SQUID placed in parallel to the loop is used to measure its state.

A charge qubit, also called as a Cooper-pair box, has a small superconducting island confined between two Josephson junctions, where an electrostatic charging energy is required to place Cooper pairs on the island. The qubit states corresponds the number of $2e$ charges on the island.

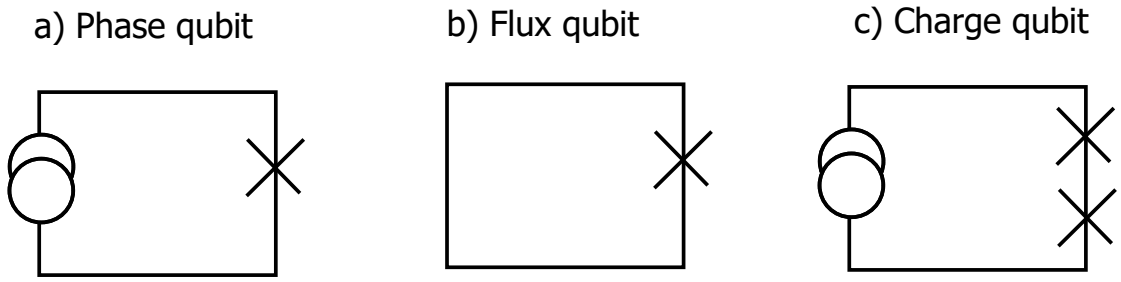

FIGURE 1.7 A schematic of a) Phase qubit, b) Flux qubit, and c) Charge qubit circuit. "X" symbols represent Josephson junctions.

1.4 Outline of chapters

This work is organized as follows: Chapter 2 is about theoretical models of quasiparticle tunneling in NIS and SIS' junctions where the physical and mathematical models are introduced to understand the current–voltage response of the devices. A brief introduction to noise theory and experimental methods in noise measurements are explained in Chapter 3. Fabrication of samples and the annealing process is explained in Chapter 4. Chapter 5 is a brief description about the low temperature experimental setups utilized in this work, including the ^{3}He–^{4}He dilution refrigerator. Chapter 6 shows the results of Al–AlO_x–Al $1/f$ noise measurements before and after annealing. Chapter 7 extends the $1/f$ noise study to NIS junctions made out of Al–AlO_x–Al:Mn, where the current–voltage response was also studied and the

material analysis was performed. Chapter 8 introduces a new Al–AlO_x–Nb sample that was measured in SIS′ and NIS states. The zero voltage supercurrent was also studied as a function of temperature and magnetic field. Chapter 9 summarizes the thesis as a conclusion.

Chapter 2

Tunneling theory

In this chapter the theoretical model for quasiparticle tunneling is explained both for normal metal–insulator–superconductor (NIS) junctions, as well as for asymmetric junction of two different superconducting electrodes superconductor$_1$–insulator–superconductor$_2$ (SIS') junctions [1]. Example calculations for $I - V$ characteristics are presented. The most important concepts are the energy gap for superconducting tunnel junctions and the density of states for quasiparticle excitations.

2.1 Superconducting energy gap

The superconducting energy gap Δ is defined to be the energy difference between the superconductor's ground state and the lowest single quasiparticle excitation. It is proportional to the critical temperature, because the energy gap is half of the Cooper-pair binding energy (two quasiparticles are formed if a Cooper pair is broken) and the critical temperature will dictate the thermal energy to break all the Cooper pairs. The BCS theory in the so-called weak-coupling limit predicts an approximate relation between $\Delta(0)$, the energy gap (at absolute zero) and the critical temperature of a material:

$$E_{gap}(0) = 2\Delta(0) = 3.528 k_B T_C, \tag{2.1}$$

where E_{gap} is the total energy gap, Δ is the gap per quasiparticle, $k_B \approx 1.38 \cdot 10^{-23}$ is the Boltzmann constant and T_C the critical temperature in Kelvin. Real superconductors have small deviations from the nominal factor 3.528, depending on how close or far from the weak-coupling limit they are.

At the absolute zero temperature all electrons are paired to Cooper pairs, but at finite temperatures there is an increasing number of thermally generated quasiparticles. The mixture of both Cooper pairs and quasiparticles won't affect the per-

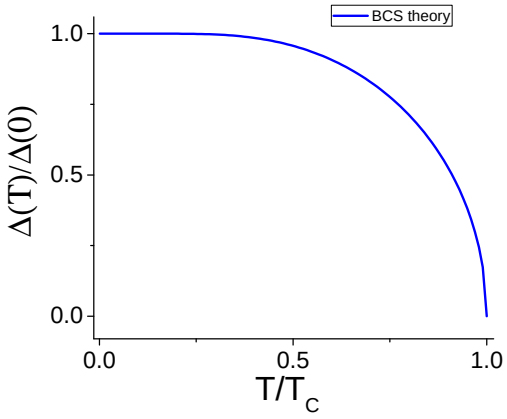

FIGURE 2.1 Suppression of the energy gap as a function of reduced temperature according to the BCS theory Eq. 2.2.

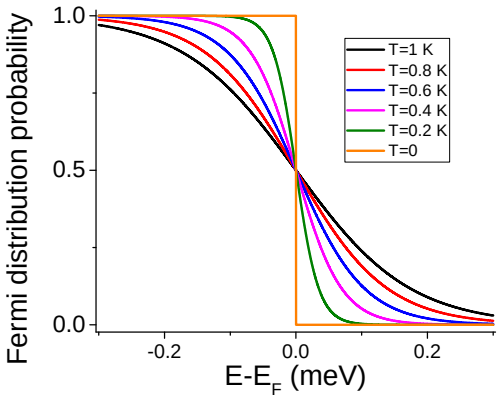

FIGURE 2.2 The Fermi-Dirac distribution at different temperatures.

fect conductivity below the superconductor's critical temperature, but the gap will decrease as the temperature approaches the critical temperature. The temperature dependent energy gap $\Delta(T)$ can be numerically calculated from the following equation in the weak-coupling limit [24]:

$$\int_0^\infty \left[\frac{\tanh(\epsilon')}{\epsilon'} - \frac{\tanh\left(\sqrt{\epsilon'^2 + \left(\frac{1.764\Delta(T)/\Delta(0)}{2(T/T_C)}\right)^2}\right)}{\sqrt{\epsilon'^2 + \left(\frac{1.764\Delta(T)/\Delta(0)}{2(T/T_C)}\right)^2}} \right] d\epsilon' = -\ln\frac{T}{T_C}. \tag{2.2}$$

The resulting temperature dependence is plotted in Fig. 2.1. The relative gap $\Delta(T)/\Delta(0)$ remains quite constant till almost $T/T_C = 0.5$, and then starts to decrease rapidly reaching zero at critical temperature.

2.2 Fermi-Dirac distribution

Tunneling can also be affected by temperature. The Fermi-Dirac distribution describes the occupancy probability of electron or quasiparticle states at energies around the Fermi level E_F, and is given by [25]

$$f(E,T) = \frac{1}{e^{(E-E_F)/k_BT} + 1}. \tag{2.3}$$

Some Fermi distributions are plotted in Fig. 2.2 for different temperatures T.

The 0 Kelvin graph shows a sharp step function, i.e. energy states up to Fermi energy E_F are filled and all above it are empty. Increased temperature smoothens the distribution.

2.3 Density of states (DOS)

The BCS theory describes the density of states n_s for quasiparticles in a superconductor as a function of energy to be [1]

$$n_s(E) = \frac{N_s(E)}{N(0)} = \begin{cases} \frac{|E|}{\sqrt{E^2-\Delta^2}}, & |E| > \Delta \\ 0, & |E| < \Delta \end{cases}, \tag{2.4}$$

where $N_S(E)$ is the quasiparticle density of states of the metal in the superconducting state, $N_N(0)$ in the normal metal state at the Fermi energy, and E is the energy measured from $E_F = 0$.

It has been found experimentally that this simple model for DOS with a singularity is not realistic for several reasons, for example due to environmentally (e.g. photon) assisted tunneling that introduces a sub-gap current [26]. A more appropriate theory to describe the density of states is the Dynes model, where a new empirical, sample-specific Dynes parameter Γ' is introduced to broaden the DOS inside the energy gap. According to this model

$$n_S(E,T) = \left| \mathrm{Re}\left(\frac{E + i\Gamma'}{\sqrt{(E+i\Gamma')^2 - \Delta(T)^2}} \right) \right|, \tag{2.5}$$

where $\Delta(T)$ is the energy gap at the prevailing temperature, and Γ' is the Dynes parameter [27, 28]. The Dynes parameter is often given in reduced units $\Gamma = \Gamma'/\Delta(0)$.

The difference between the DOS functions based on simple BCS theory and the Dynes model is illustrated in Fig. 2.3, where it can be seen that especially inside the gap the difference is clear, but at smaller Dynes values the difference is getting smaller, especially outside the gap. The difference in varying Γ is plotted on a semilogarithmic scale in Fig. 2.4.

2.4 Semiconductor model of tunneling

Tunneling dependence on the energy of the quasiparticles can be modeled using the so-called semiconductor model [1] where, in contrast to a normal metal with a constant density of states occupied up to the Fermi level, the superconductor has

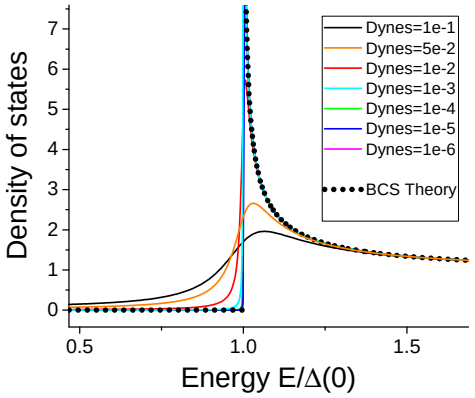

FIGURE 2.3 The difference between the density of states according to the BCS model and the Dynes model, with varying Dynes parameter Γ.

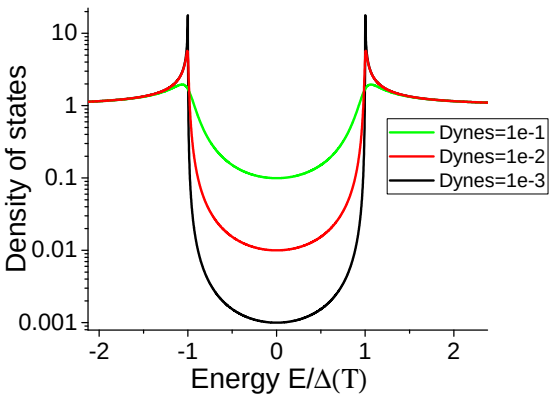

FIGURE 2.4 The density of states (DOS) as a function of energy with different Dynes parameters Γ.

an energy gap 2Δ around its Fermi energy with quasiparticle DOS occupied below the gap and empty above. In Fig. 2.5 we illustrate the schematics of the density of states for normal metal–insulator–superconductor (NIS) (left) and superconductor$_1$–insulator–superconductor$_2$ (SIS') junctions (right) where the NIS junction is at zero temperature, and the SIS' at $T > 0$ with some thermally excited quasiparticles and holes. Occupied states are denoted with a yellow color and empty states with green. The junctions are voltage biased to $eV \simeq \Delta$ and $eV = \Delta_2 - \Delta_1$, respectively.

Within this model the tunneling occurs horizontally, as an elastic process, i.e. it is a constant energy transition that requires that there exists both occupied and empty energy states on both sides of the barrier, which may be facilitated by thermally excited electron states. First order single-particle tunneling is only considered, which is a reasonable assumption since in this work junction resistances are large and higher order tunneling is proportional to $1/R_T^2$ [29]. In addition, no evidence of higher order tunneling [30] at zero bias has been seen experimentally in our samples.

In NIS devices the conductance increases rapidly as the bias voltage exceeds the energy gap of the superconducting electrode. A similar increase in current is seen in SIS' junctions when biased over the combined gap $\Delta_1 + \Delta_2$. At finite temperatures $T > 0$, there is another (but smaller) conductance peak at a lower voltage corresponding to $\Delta_2 - \Delta_1$ since at that voltage thermally excited quasi-particles in superconductor$_1$ can tunnel into the empty density of states in superconductor$_2$ (Fig. 2.5).

Both the finite temperature (smoothing by the Fermi-function) and the smear-

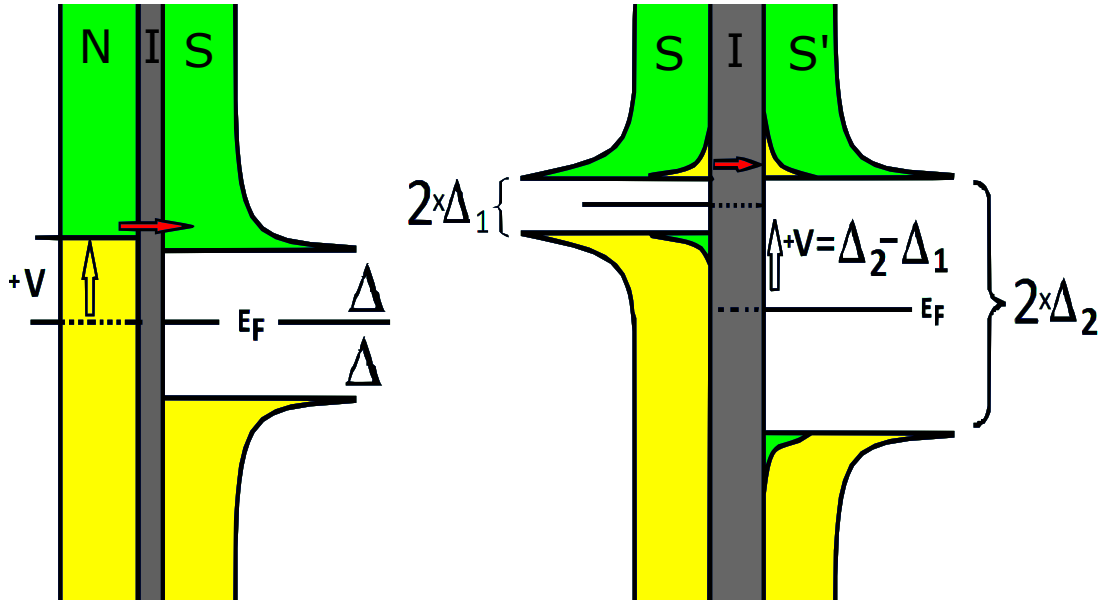

FIGURE 2.5 A semiconductor model describing electron tunneling in NIS (left, at $T = 0$) and SIS' (right, at $T > 0$) junctions. Density of states is plotted horizontally and energy vertically. Yellow depicts occupied states and green empty states. Tunneling though the barrier can take place horizontally (constant energy) if there are both occupied and empty states available on both sides, which may be facilitated by thermal excitations.

ing of the density of states (Dynes model) will introduce some leakage or subgap current seen as a finite conductance at voltages below the Δ/e.

2.5 NIS tunneling

The previously explained theories for the gap function, the Fermi-Dirac distribution and the density of states will come useful in calculating the tunneling current as a function of bias voltage. The equation for single particle tunneling current in an NIS junction is [1]

$$I_{NIS} = \frac{1}{eR_T}\int_{-\infty}^{\infty} n_N(E)n_S(E+eV)(f_N(E) - f_S(E+eV))dE, \tag{2.6}$$

where e is the elementary charge, R_T is the asymptotic tunneling resistance at higher bias voltage ($V > \Delta/e$), f_N and f_S are Fermi distributions for normal metal and superconductor respectively, and $n_S(E)$ is the superconductor density of states, where the Dynes model should be used, with the temperature dependence of the gap also taken into account. In the case of an NIS junction the normal metal density of states function simplifies as $n_N(E) = 1$.

The behavior of the current–voltage relation at different temperatures ($\Gamma =$

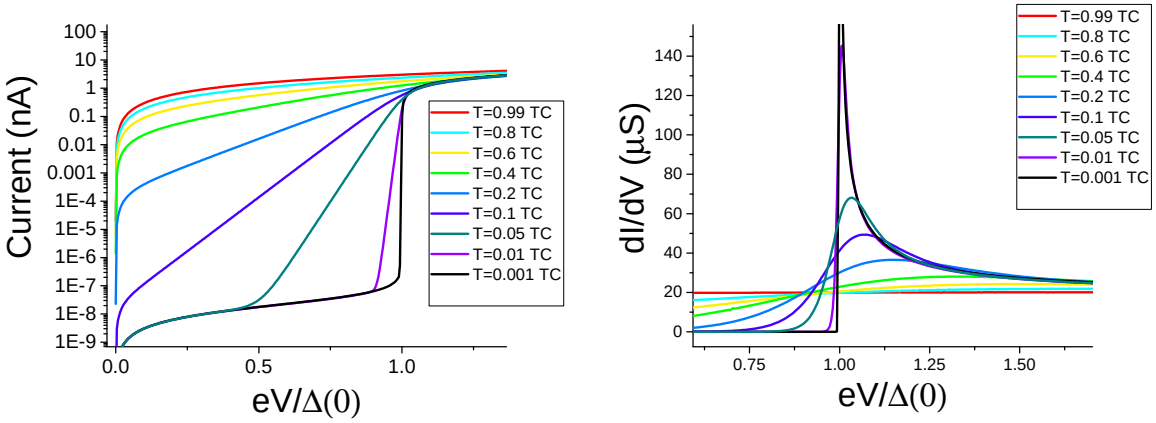

FIGURE 2.6 Calculated current–voltage characteristics at different temperatures (T/T_C) for a single NIS junction. The same simulation is plotted as $I-V$ data on the left and as the differential conductance $dI/dV-V$ on the right. The parameters used in the simulations are $R_T = 50$ kΩ, $\Gamma = 1\cdot 10^{-8}$, $T_C = 1$ K and $\Delta(0) = 1.764 k_B \cdot 1$ K $= 0.15$ meV.

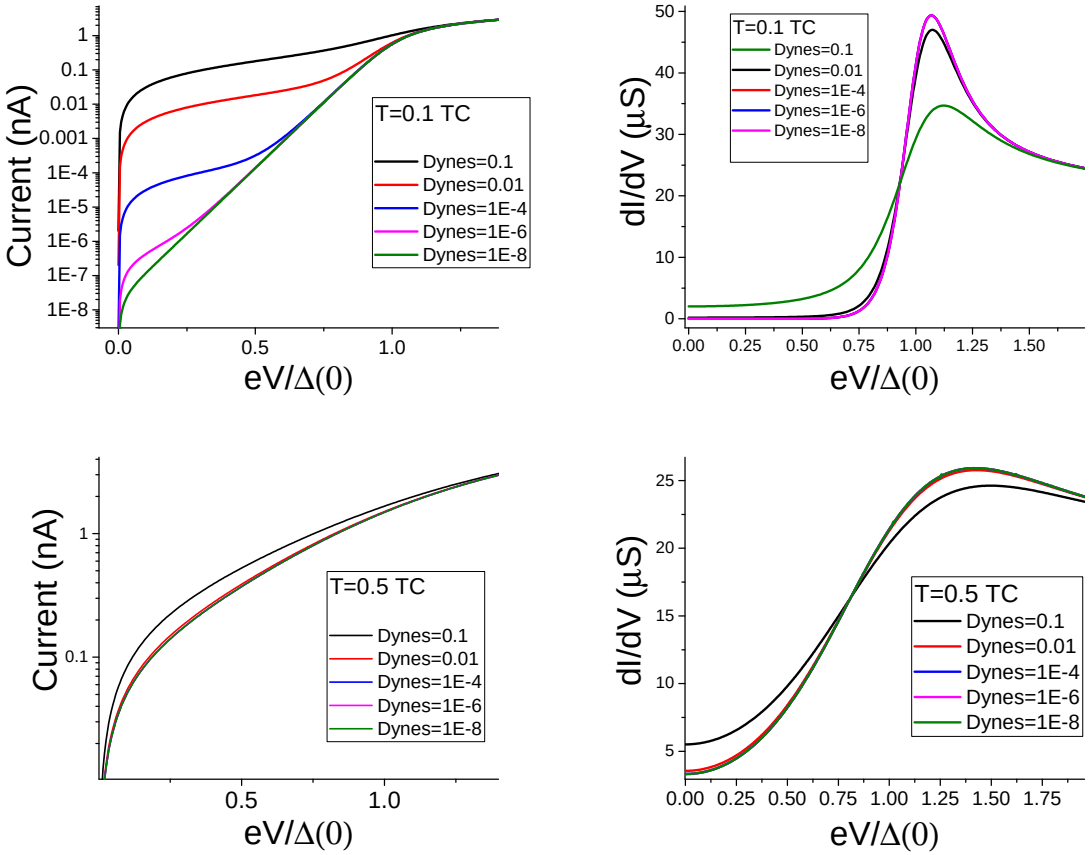

FIGURE 2.7 Calculated current–voltage characteristics in an NIS junction using different Dynes parameters (Γ) at two different temperatures; $T = 0.1T_C$ (top panels) and $T = 0.5T_C$ (bottom panels). The same data is plotted in as $I-V$ (on the left) and dI/dV (on the right).

10^{-8}, $T_C = 1$ K and $R_T = 50$ kΩ) is illustrated in Fig. 2.6 and, as a function of the Dynes parameter at two different temperatures in Fig. 2.7. At higher temperatures, lowering Γ makes no difference anymore since the thermal response is dominating. In experiments, one thus needs to determine the Dynes parameter from the lowest temperature data.

All these theoretical plots for both NIS and SIS' junctions were simulated using an Octave code written by the author where no thermal modeling is used, i.e. $T_e = T_s = T_{bath} = T$, albeit in real life situations the normal metal and superconductor can possess different temperatures than the bath temperature. This can happen at very low cryogenic temperatures where cooling powers of the sample are rather weak [31].

2.6 SIS' tunneling

The function to calculate the quasiparticle current in an SIS' junction won't differ much from the case of NIS tunneling; the only difference is that now the normal metal is replaced by another superconductor that has its own energy dependent DOS. The junction current is

$$I_{SIS'} = \frac{1}{eR_T}\int_{-\infty}^{\infty} n_{S_1}(E)n_{S_2}(E+eV)(f_{S_1}(E) - f_{S_2}(E+eV))dE, \tag{2.7}$$

where one must remember that the gap and Dynes parameters are not necessarily the same for the two superconductors.

Theoretical simulations for an SIS' junction with different gaps (and thus critical temperatures) and Dynes parameters were calculated. The results with different varying parameters are plotted in Fig. 2.8. Let's start the analysis with panel a) where the temperature was varied. One can easily see the sharp current steps at $V \approx 0.225$ mV and $V \approx 1.425$ mV, due to the two gaps at $eV = \Delta_1$ and $eV = \Delta_1$+Δ_2. Their appearances are obviously more pronounced at lower temperatures. In addition we would like to especially point out the feature at $eV \approx \Delta_1$, which is often ignored in discussions [1, 32]. Besides the gaps there is the famous "singularity matching" high conductance bump at $eV = \Delta_2$-Δ_1. As it is thermally excited tunneling, the feature will disappear at low temperatures. The horizontal positions of the gap features change noticeably because of the temperature dependence of the gap.

In panel b) we see that by changing the smaller gap value, the steps will only shift the Δ_1 and Δ_1+Δ_2 features horizontally. If the temperature was higher, then the conductance peak at $eV = \Delta_2$-Δ_1 would be visible also.

In panel c) the Dynes parameter Γ for the superconductor with a smaller gap

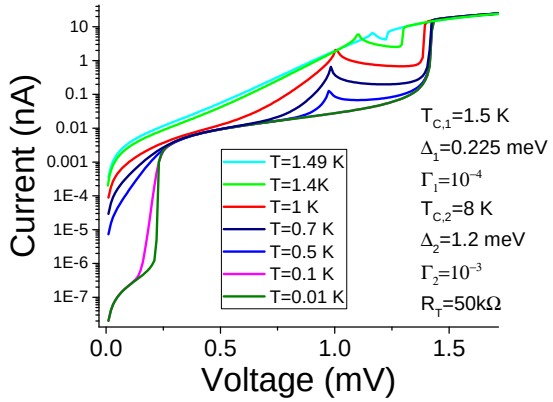

a) Varying the bath temperature.

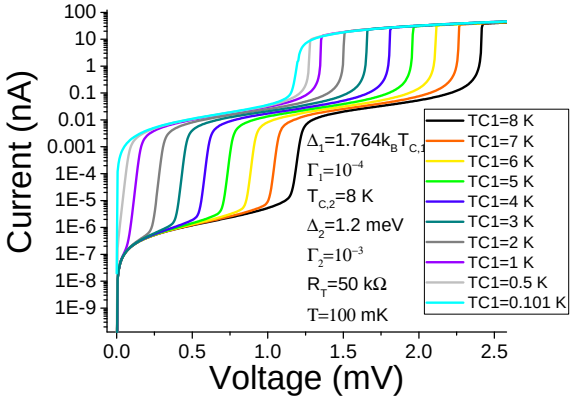

b) Varying the smaller gap.

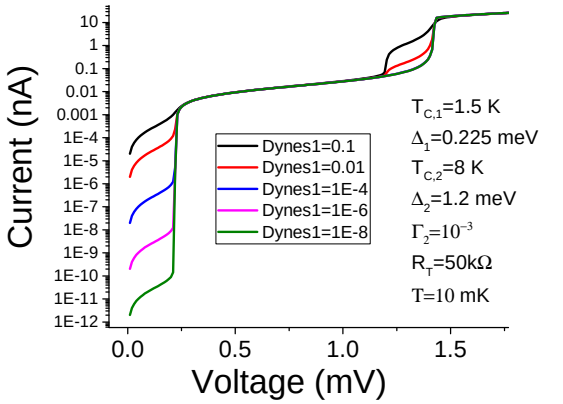

c) Varying the Dynes for SC1.

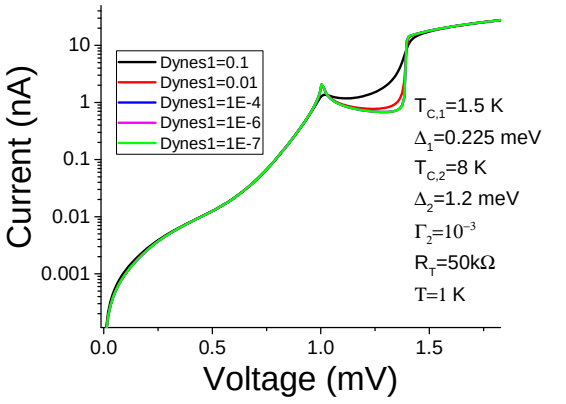

d) Varying the Dynes for SC1 at higher T.

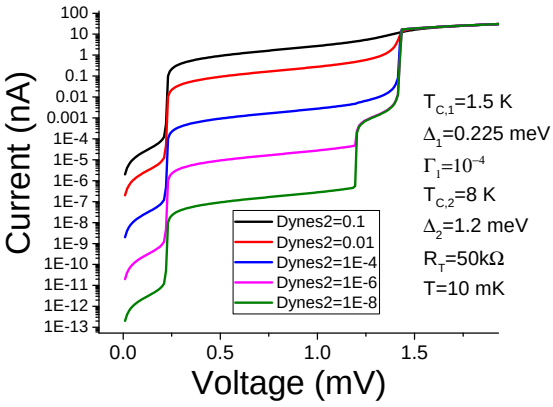

e) Varying the Dynes for SC2.

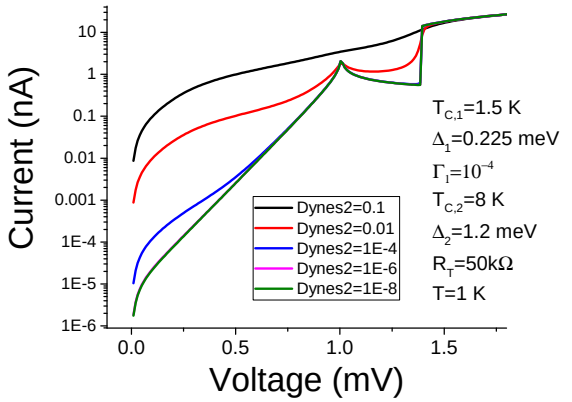

f) Varying the Dynes for SC2 at higher T.

FIGURE 2.8 Calculated current–voltage ($I-V$) characteristics for a single SIS′ junction tunneling when varying different parameters.

was varied. Clearly Γ_1 plays an important role inside the gap of the corresponding superconductor$_1$ when $eV < \Delta_1$, but also when $\Delta_2 - \Delta_1 < eV < \Delta_1 + \Delta_2$, since at this voltage region the conductivity depends on the DOS of both superconductors.

A higher temperature, shown in panel d), kills off the Γ_1 dependency at low voltages, but the conductance between $eV = \Delta_2 - \Delta_1$ and $eV = \Delta_2 + \Delta_1$ will again emerge and shows its contribution dependency on Γ_1.

In panel e) Γ_1 was fixed to a reasonable value while varying Γ_2. Because of the really low temperature (10 mK) compared to the critical temperature of the corresponding superconductors (8 K), the $I - V$ characteristic shifts vertically at voltages below the combined gap $\Delta_2 + \Delta_1$.

The same calculation with varying Γ_2 but at higher temperature in plot f) shows a saturation at low values of Γ_2 because the thermal smearing dominates. Also, the presence of the conductance peak at $eV = \Delta_2 - \Delta_1$ will be obscured at higher Γ_2 parameter values.

2.7 Thermal models

By allowing different temperatures in the two electrodes (superconductors and/or normal metals) the shape of current–voltage characteristics will change, especially because the device temperature is also a function of the bias voltage in that case. In the calculations, presented in Chapters 2.5 and 2.6, was assumed that the whole sample is at the same temperature, which often isn't true, since tunneling will either heat up or cool down the junction due to the tunneling of quasiparticles of different energies that will contribute to self heating or cooling. In addition, Cooper pairs carry neither entropy nor heat, making a superconductor a poor heat conductor (phonons and quasiparticles still carry heat). This can leave the normal metal thermally rather isolated in some cases.

An NIS or an SIS' junction can also operate as an electron cooler via selective tunneling, i.e. when properly biased just below the gap such that only the most energetic electrons tunnel from the normal metal's Fermi tail cooling down the normal metal [14]. The cooling power depends on many parameters; there is typically only a small window where effective cooling is possible, and outside those specs the normal metal will most likely only heat up [33].

Thermal modeling in SINIS devices was studied in several papers [34–36]. Here we use the expression from Chaudhuri *et al.* [37] for two asymmetric junctions where the voltage drop across each junction (V_L, V_R) differ.

The heat currents $\dot{Q}_i$ through each junctions ($i = L, R$) are given by equations:

$$\dot{Q}_L = \frac{1}{e^2 R_L} \int_{-\infty}^{\infty} (E + eV_L) n_S(E)(f_S(E) - f_N(E + eV_L))dE, \tag{2.8}$$

$$\dot{Q}_R = \frac{1}{e^2 R_R} \int_{-\infty}^{\infty} (E) n_S(E + eV_R)(f_N(E) - f_S(E + eV_R))dE. \tag{2.9}$$

Hence the total cooling power of a SINIS junction is

$$P_T = -\dot{Q}_L + \dot{Q}_R. \tag{2.10}$$

In the thermal model, the cooling power of the junction P_T has to be calculated by solving a power balance equation that includes all relevant heat flows into and out of the normal metal:

$$P_T = B(T_{bath}^n - T_N^n) + \beta[(P_T + I(V_L + V_R)] + I^2 R_N. \tag{2.11}$$

The first term describes thermalization of normal metal electrons to phonons where $B = \Sigma\Omega$ is the electron-phonon coupling strength inside the normal metal, where Σ is the material-specific electron-phonon coupling constant and Ω is the normal metal electron gas volume. Here the heat transfer from phonons of the film to the substrate phonons is assumed to be effective enough to be insignificant compared to electron-phonon coupling in the film. Phonon-phonon coupling between the substrate (bath) and the normal metal is assumed to be large compared to other effects. The exponent n depends on the sample material, its quality and geometry [38], but is typically 5 for thick (> 30 nm) films [37]. With a really large B, the sample is perfectly thermalized and the resulting plots equal the simple model without thermal modeling.

The second term describes the indirect backflow of heat from the superconducting electrodes back to the normal metal, with a phenomenological coefficient $0 \leq \beta \leq 1$ governing the fraction of the total deposited heat backflow to normal metal [39].

The final term describes a simple Joule heating in a normal metal with resistance R_N.

Chapter 3

Noise

3.1 Noise definition

Noise is commonly defined as an unwanted disturbance that interferes with the measurement signal [40]. It originates from different sources, and not only from different devices but from different physical phenomena. A particular noise mechanism will show up as the same, random fluctuations hindering e.g. wired and wireless broadcasts and other signals. Figure 3.1 illustrates a huge noise that is almost completely obscuring a sinusoidal AC signal, monitored in the screen of an oscilloscope.

Because noise is random it can't be predicted in advance and thus can not be totally eliminated. One can only reduce it with shielding and filtering, but those techniques cannot be used to the fullest, otherwise the signal would be eliminated, as well.

Noise is usually something to get rid of to be able to measure signals properly, but sometimes noise is the signal to be measured. Studying noise is important in understanding its fundamental sources, and maybe by understanding it one can find ways to reduce it by better electrical designing. Noise limits the smallest signal one can measure; it limits the sensitivity of a sensor. For example, in modern digital cameras noise looks similar to grains found in film photographs, which are mostly visible at low-light photographs with high ISO-speeds when the sensor battles to detect some of the dim light with lots of electrical amplification. The same principle applies to other detectors. Random noise spikes can trigger switches that can make digital electronics to fail because of faulty triggers. Noise reduction with electronic circuits is sometimes possible for some noise types, e.g. such a random noise spikes, but not for fundamental noise sources such as thermal noise.

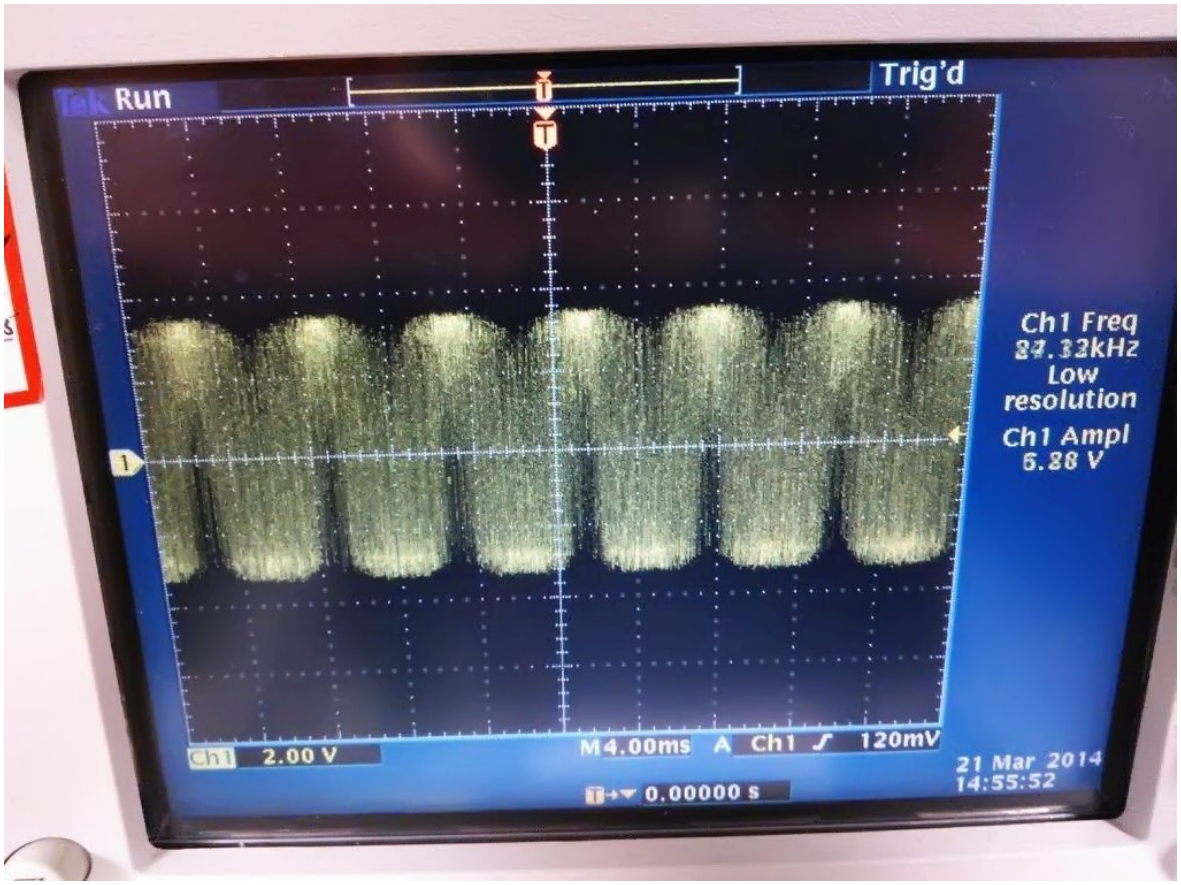

FIGURE 3.1 A strong noise obscuring a sinusoidal AC signal seen on an oscilloscope's screen.

3.2 Thermal noise

Thermal noise, also known as Johnson-Nyquist noise, or simply Johnson noise, originates from thermal motion of electrons similar to Brownian motion of particles [40]. There is no net DC current due to this motion, but there are voltage fluctuations at all frequencies that can also be seen as a current fluctuations in a circuit.

Noise is commonly expressed in terms of spectral density, i.e. the noise content per 1 Hz bandwidth ($\Delta f = 1$ Hz). The spectral density is acuired from time-domain voltage signal using a fourier trasform in a spectrum analyzer. Thermal noise exists without any biasing so it is originally voltage noise that has spectral density units of V^2/Hz. The equation for thermal noise is [41]

$$S_V(f) = E_V^2(f)/\Delta f = 4k_BTR(hf/k_BT)(e^{(hf/k_BT)} - 1)^{-1}, \tag{3.1}$$

where k_B is Boltzmann's constant, h is Planck's constant, T is the temperature,

and R denotes the sample resistance. In the low frequency limit, $hf \ll k_B T$ the equation simplifies to a frequency independent spectral density (white noise)

$$S_V(f) \overset{hf/k_BT \ll 1}{=\!=\!=} 4k_BTR. \qquad \text{V}^2/\text{Hz} \tag{3.2}$$

The classical approximation $hf \ll k_B T$ gives a limit $f \ll 2$ GHz at 0.1 K, so we see that a typical low-frequency experiment is in the classical limit.

Johnson-Nyquist noise is a fundamental noise source, it depends on the sample resistance and temperature and can't be changed without altering those two parameters.

3.3 Addition of noise and equivalent circuits

If two sinusoidal signals have the same frequency and phase, their amplitudes can be summed arithmetically. If the phase difference is 180 degrees, equal amplitudes cancel each other, and any other phase difference between those extremes will have some different contribution. The equation for the addition of amplitudes V_1 and V_2 is

$$V_{tot}^2 = V_1^2 + V_2^2 + 2CV_1V_2, \tag{3.3}$$

where C is the correlation coefficient that can have all the values between -1 and $+1$. $C = +1$ means signals are completely correlated, that leads to $V_{tot}^2 = (V_1 + V_2)^2$ and $C = -1$ means fully uncorrelated signals $V_{tot}^2 = (V_1 - V_2)^2$.

Addition of noise sources is done using the same principles as for an arbitrary signal: The voltage in Eq. 3.3 is replaced by a noise voltage

$$E = \sqrt{S_V \Delta f} \qquad \text{V}, \tag{3.4}$$

leading to the equation

$$E_{tot}^2 = E_1^2 + E_2^2 + 2CE_1E_2. \tag{3.5}$$

Commonly noise is random, the frequency is random and the phase is random, thus the correlation constant $C = 0$ and the rms summation $E_{tot}^2 = E_1^2 + E_2^2$ of noise voltages should be used. Partially correlated noise is however possible, e.g. if the noise arises from a common source.

Although Johnson noise is a pure voltage noise source, it can be modeled as a current source in parallel with a noiseless resistor leading to the current noise

equation for thermal noise:

$$S_I(f) = S_V(f)/R^2 = 4k_BT/R. \tag{3.6}$$

The basic principle in the addition of noise sources states that the strength of thermal noise in connected resistors equals noise from the single resistor with the equivalent resistance of the circuit, e.g. two resistors R_1 and R_2 in parallel have a noise

$$S_V = 4k_BTR_{||} = 4k_BT\frac{R_1R_2}{R_1+R_2}. \tag{3.7}$$

The analysis gets a bit more complicated if resistors are at different temperatures, e.g. a sample R_S is at very low cryogenic temperatures but ballast resistor R_B is located at room temperature, as illustrated in Fig. 3.2. This can be calculated by modeling the thermal noise S_V in a resistor R_B at a temperature T_B as a current source S_I that is flowing through both resistors that are connected in parallel. The equation for thermal noise from the resistor R_B is

$$S_V = S_IR_{\mathrm{II}}^2 = (\frac{4k_BT_B}{R_B})(\frac{R_BR_S}{R_B+R_S})^2. \tag{3.8}$$

By calculating the same equation for resistor R_S we get the sum of noises from both resistors that simplifies to Eq. 3.7 if both resistors are at the same temperature:

$$S_{V,Total} = (\frac{4k_BT}{R_S})(\frac{R_BR_S}{R_B+R_S})^2 + (\frac{4k_BT}{R_B})(\frac{R_BR_S}{R_B+R_S})^2 = 4k_BT\frac{R_SR_B}{R_S+R_B}. \tag{3.9}$$

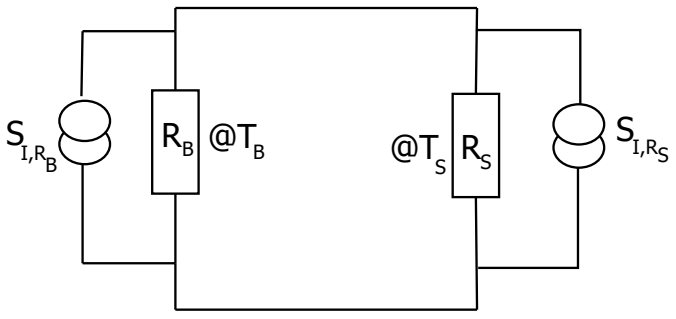

FIGURE 3.2 Thermal noise from two resistors (R_B and R_S) at different temperatures is modeled by creating an equivalent current noise source S_I from resistor R_B driving both resistors in parallel, and the same for R_S.

3.4 Excess noise and shot noise

In addition to fundamental thermal noise there can also be additional excess noise if current is flowing. Shot noise is a current noise caused by the electrons (or other charge carriers) not moving smoothly but as pulses of current. It arises due to charge fluctuation. It is a current noise with units of A^2/Hz and has a power spectral density

$$S_I(f) = 2eI, \tag{3.10}$$

where e is the electron's charge and I is the current flowing through the specimen [40].

Equation 3.10 seems simple and straightforward to use, but it doesn't always apply, since shot noise is only present when the current is flowing through a barrier or otherwise heavily congested conductance channel [41]. For tunnel junctions specifically, Eq. 3.10 applies if current is high enough. In an ordinary metallic wire the shot noise is not present, or is at least heavily suppressed [42].

For tunnel junctions, one can combine thermal noise and shot noise into one function. The current spectral density for combined Johnson and shot noise is given by [43]

$$S_{I,J+S}(f) = 2eI \coth\left(\frac{eV}{2k_BT}\right), \tag{3.11}$$

which gives the shot noise in the high voltage limit:

$$S_{I,S}(f) = \lim_{eV \gg k_BT}\left[2eI \coth\left(\frac{eV}{2k_BT}\right)\right] = 2eI, \tag{3.12}$$

and Johnson noise at zero bias voltage:

$$S_{I,J}(f) = \lim_{V \to 0}\left[2e\frac{V}{R}\coth\left(\frac{eV}{2k_BT}\right)\right] = 4k_BT/R, \tag{3.13}$$

as $\coth(x) \sim \frac{1}{x}$ when $x \ll 1$.

3.5 1/f noise

$1/f$ noise is an excess noise, just like shot noise, and it also shows only when flowing current though a medium. Unlike shot noise, $1/f$ noise doesn't have any microscopic mathematical theory to predict the noise level, but experimental results indicate it can originate, for example, from carrier generation and recombination,

and defects such as oscillating two-state systems, like an impurity atom in a lattice [41]. It is called $1/f$ noise because the spectrum is typically quite close to a function $S_I(f) = Af^{\alpha}$, with $\alpha \approx -1$. Sometimes all low-frequency noise that has an increasing spectrum at low frequencies is loosely called as $1/f$ noise, even if the exponent is, for example, closer to $\alpha = -2$. Sometimes names like flicker noise and pink noise are also used.

$1/f$ type low-frequency noise is not only present in electrical systems, but almost everywhere; such fluctuations are detected in other physical systems, technology, biology, astrophysics, geophysics, economics, psychology, language, traffic jams, and even music [44].

$1/f$ noise is quite strong in tunnel junctions, which may be a problem in many applications, for example, in the case of superconducting qubits, where low-frequency resistance fluctuations cause dephasing of qubits [45].

As it is always observed in tunnel junctions, we have focused in this thesis in its characterization and possible reduction in several different junction types [46] [A.I.] [A.II.].

3.6 Difficulties in noise measurements

Measuring a DC or AC signal is quite straightforward, the signal can be easily visually identified already on a computer's or an oscilloscope's screen, thus getting confirmation that everything is working. If there are, for example, bad cables or loose connectors noise will be introduced into the system, which will be seen around the signal, or in the worst case the signal is lost completely. Essentially, one will immediately notice that something is wrong and take proper actions.

Noise measurements are different. Now noise is the signal, so one can't easily see problems directly, because the noise spectra can also contain noise from other sources than the sample being examined. One can't separate the noise sources either, noise is always noise, completely random. This means that in measurements everything can be wrong: Broken cables, wrong amplifier settings, empty batteries, disconnected wires, forgotten groundings and even dead samples, but there will still be noise visible that the poor experimentalist spends the rest of the night trying to measure. The proper noise from the sample is confirmed only after the appropriate data analysis, e.g. in the simplest case subtracting all the other known noise sources.

3.7 Low frequency noise measurements, AC modulation bridge setup

Measuring a small signal such as noise requires amplification. Unfortunately, amplifiers itself are full of electronics creating noise of their own, which may obscure the noise being measured. Amplifier manufacturers do their best in designing as low noise amplifiers as possible, and they provide datasheets showing the measured voltage- and current noise at different frequencies and input impedance values that can be used in designing an experiment.

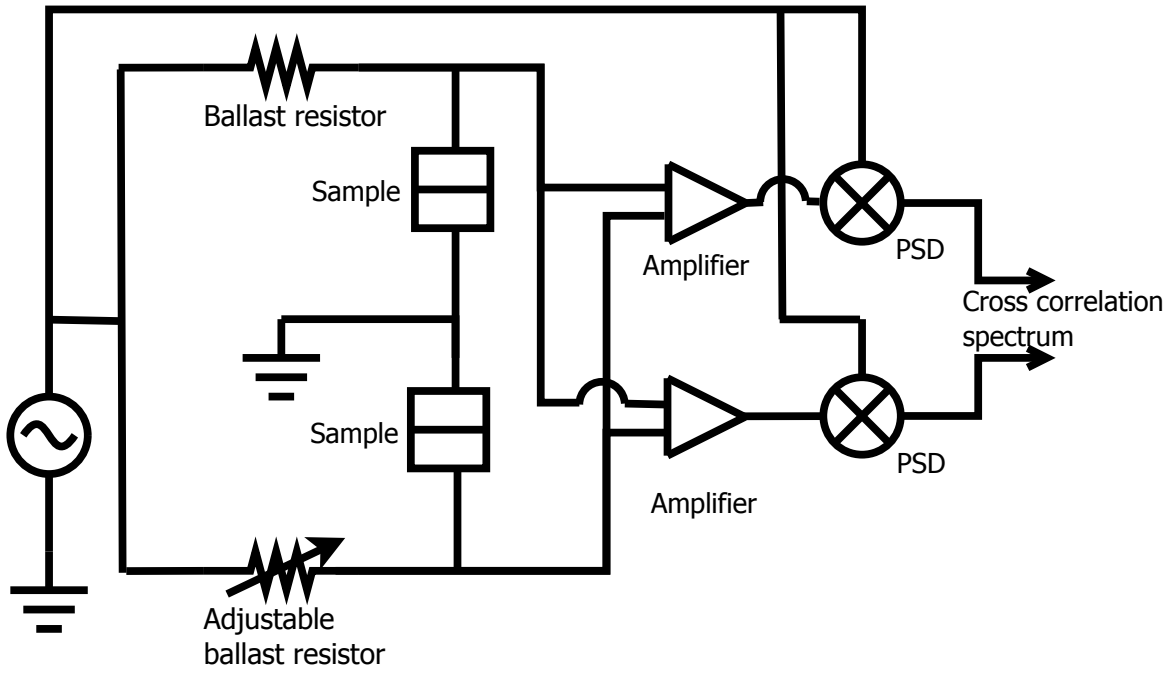

FIGURE 3.3 Schematics of the AC modulation bridge noise measurement setup with two pre- and lock-in amplifiers (PSD) and a cross-correlation spectrum analyzer. The fixed ballast resistor has a resistance of 1 MΩ, and the adjustable resistor (General Radio 1433B) is used to balance the bridge. Due to the bridge measurement technique both tunnel junctions are measured together.

In this thesis the studied noise is low-frequency $1/f$ noise in tunnel junctions. This introduces an issue that preamplifiers have a rather high low-frequency $1/f$ noise of their own that hinders detecting the input noise at the same frequencies. The author's Master's thesis [47] is also about noise measurements. There I explained with experimental results the basics about different techniques in low-frequency noise measurements, and various methods to get rid of the preamplifier noise. Here I discuss only the best measurement method, which was used in the experimental

part of this thesis.

The method utilizes an AC modulation bridge setup [48] that is illustrated in Fig. 3.3. The operation principle is to move the input noise into higher frequencies, into the AC excitation frequency, where preamplifiers won't have a high $1/f$ noise anymore, but instead the amplifier's noise minimum, which is seen usually at around 1 kHz. This shifting of frequencies is accomplished with a modulation, an AC voltage which is applied across the samples, where the *resistance* fluctuations of the samples modulate this carrier signal. The carrier signal with the modulated noise spectrum at favorable frequency is then amplified without introducing more noise into it. The excitation amplitude governs the current through the sample and thus the resistance noise level. Finally, a PSD (phase sensitive detection) in lock-in amplifiers [49, 50] is used to demodulate the noise signal back to original frequency range and measured by a spectrum analyzer.

One should keep in mind that the lock-in amplifier can't lock into the noise signal, so there is no automatic phase shift feature thus one must record the same data using all the possible phase shifts (0-180 deg), plot them and find the noise maximum from that dataset corresponding to the in-phase component, i.e. the noise from the sample.

The bridge setup is necessary, because without it the AC excitation voltage drop over the sample resistance would overload the amplifier input, thus making it impossible to have sensitivity to detect a faint noise signal. When the bridge is balanced, the AC voltage due to the two branches of the bridge (the two samples in Fig. 3.3) cancel, and there is only voltages due to the noise that allows the maximal sensitivity of preamplifiers. The high 1 MΩ low noise ballast resistance and the adjustable resistor are needed for amplifiers to see the sample, as from the preamplifiers' point of view the ballast resistors and junctions are in parallel and without them the amplifier input would be shorted by the voltage source.

Two preamplifiers and the cross correlation function in the spectrum analyzer should be used, since it will remove uncorrelated components from individual amplifiers that are not from the sample noise. The measured noise baseline difference between a single amplifier and cross correlation from two amplifiers was found to be at least an order of magnitude. That is a clear result, but not enough alone to get rid of the amplifier's strong $1/f$ noise at low frequencies, where already at 1 Hz frequency the excess $1/f$ noise is several orders of magnitudes more than the baseline. Thus the AC modulation setup is needed for good measurements.

3.8 Noise analysis and normalization

A spectrum analyzer will always output an amplified voltage spectrum

$$S_{meas.}(f) = A^2 \cdot S_V(f), \tag{3.14}$$

where A is the total amplification gain from pre- and lock-in amplifiers and S_V the real voltage noise from the sample. The noise level for excess noise, like $1/f$ noise, depends on current, so for consistency one would like to normalize it with the current flowing through the sample, thus getting it in the units of resistance noise

$$S_R(f) = \frac{S_{meas.}(f)}{A^2 I^2} = \frac{S_{meas.}(f) \cdot (R_B + R1_T)^2}{A^2 U_{exc}^2}, \tag{3.15}$$

where R_B is the ballast resistance, $R1_T$ a tunneling resistance of a single junction and U_{exc} is the excitation voltage. When balanced, the current through both branches of the bridge is the same, here we choose to calculate it using the branch with the ballast resistor. After this analysis all spectra from the same sample but with different excitation will have an equal noise level independent on the current through the sample.

But samples do vary, some have thicker insulator (tunneling barrier) and/or the tunneling area is of different size, changing the tunneling resistance. As mentioned before, excess noise is more pronounced in small samples with hindered conductivity, so it is also possible to check whether $1/f$ noise is a sample independent in tunnel junctions. The smaller the area or thicker the barrier means higher tunneling resistance, R_T, thus it can be used as an additional normalization parameter, squared since noise is in power spectrum units. The AC modulation bridge setup measures the noise from both junctions together, so the R_T is the combined resistance, $R1_T + R2_T$. The final formula used for calculating the sample normalized noise is then:

$$\frac{S_R(f)}{R_T^2} = \frac{S_{meas.}(f)(R_B + R1_T)^2}{A^2 U_{exc}^2 (R1_T + R2_T)^2}. \tag{3.16}$$

It was found to agree surprisingly well with the $1/f$ noise level of samples of different geometry. Moreover, by normalizing as above one can see changes in the intrinsic noise mechanism, for example, after annealing.

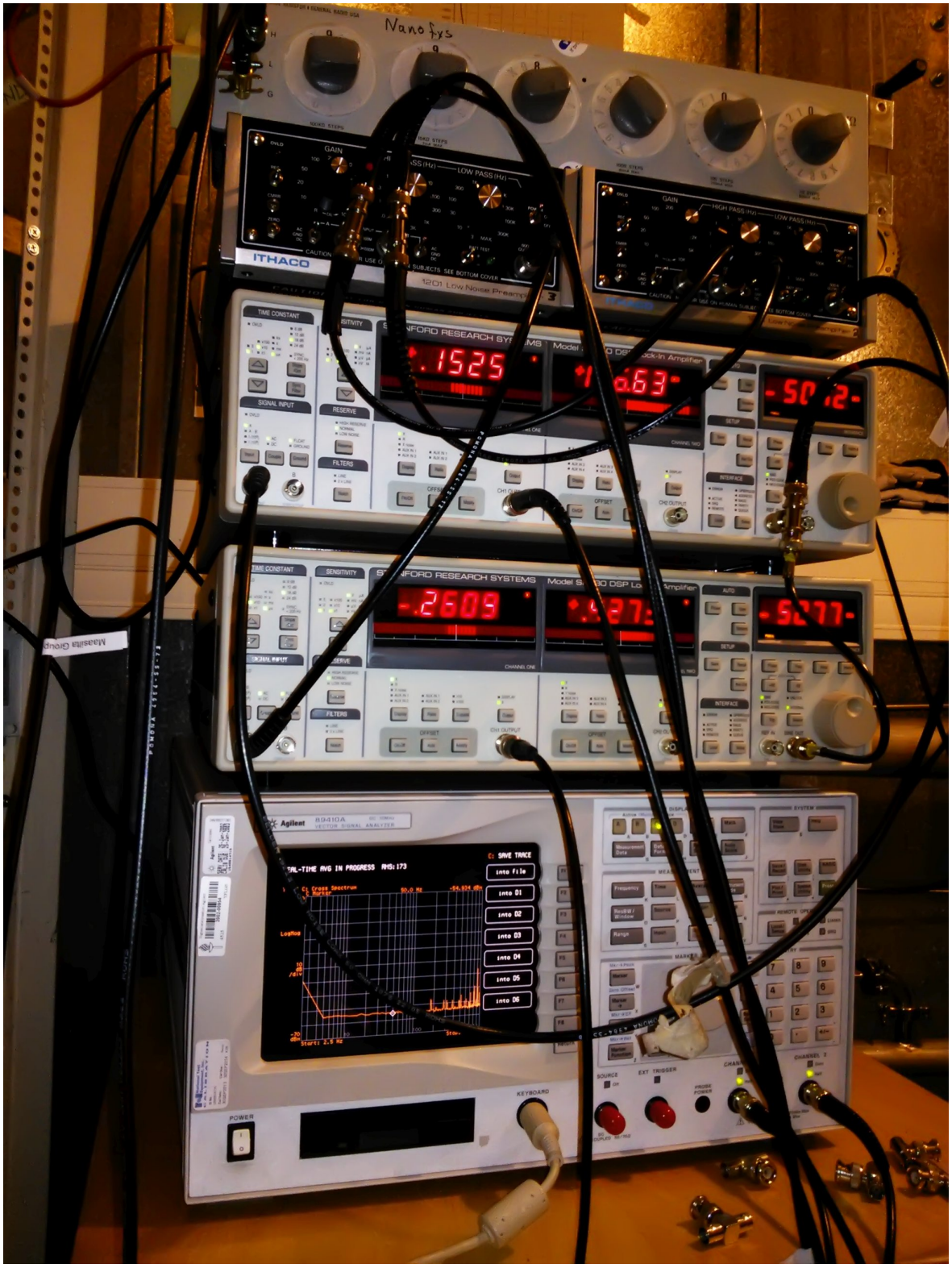

FIGURE 3.4 A photo of the noise measurement setup. Instruments from the bottom: spectrum analyzer (Agilent 89410A), two lock-in amplifiers (Stanford Research Systems SR830), two preamplifiers (Ithaco 1201) and adjustable resistor.

Chapter 4

Sample fabrication

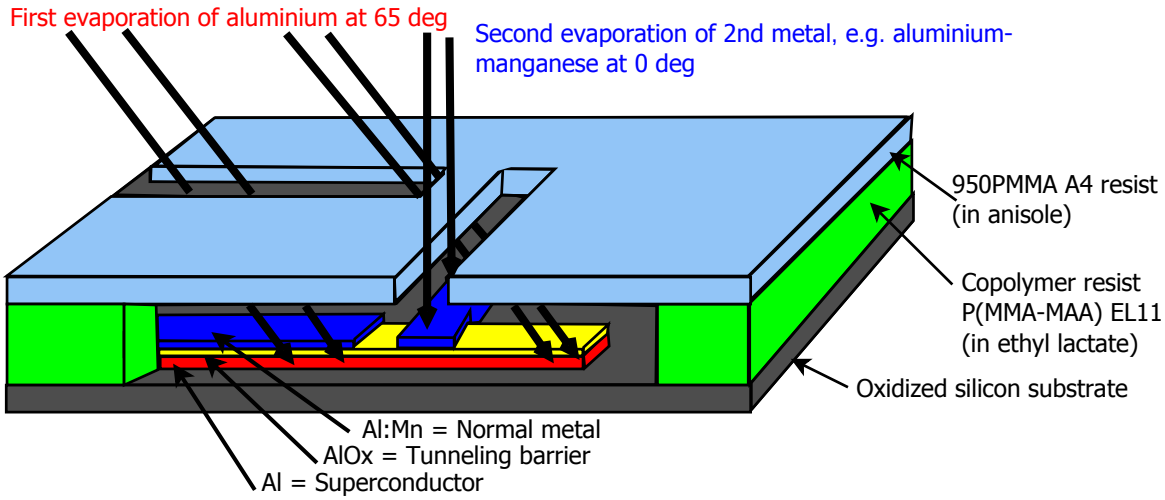

FIGURE 4.1 A schematic of the sample fabrication process using angle evaporation of metals though a mask. Electron beam lithography was used to expose dual resist layers (PMMA and copolymer), the dissolved opening allows metal to reach the surface of the silicon chip. In-situ oxidation of aluminium film grows the tunneling barrier between the two metal depositions.

The most straightforward way to fabricate a submicron sized tunnel junction involves angle evaporation of metals in a vacuum. It consists of a deposition of an easily oxidizable material e.g. aluminium on a substrate, oxidization of its surface to create a tunneling barrier and then deposition of another material on top of the oxide to create a junction (Fig. 4.1) [51, 52]. This method by its nature leads to good quality junctions, since in the fabrication process the vacuum is never broken and no additional materials are needed for the insulator. The method is also easy and straightforward to utilize because the lithography pattern is simple, only two angle evaporations are needed, there is no need for etching or additional lithography

processes with more resists layers and alignments.

It would be very difficult to evaporate the insulating barrier separately, since it is much thinner than metal films and in the limits of the accuracy of the thickness monitor. The in-situ oxidization at accurately controlled oxygen pressure is preferred method, to have a good consistency in barrier properties between all samples.

Another technique for junction fabrication is the so-called trilayer process [53] where the films are deposited first and the etching is used to define the junctions. It is, however, harder to integrate this trilayer process with more complex devices.

All the samples presented in this thesis were fabricated using electron beam lithography and angle-shadow evaporation of metals. Substrate was either oxidized or nitridized silicon, and the two resist layers were 950PMMA A4 (4% in anisole) on top of P(MMA-MAA) EL11 (11% in ethyl lactate). Prior to metal depositions, the chip was cleaned with O_2 plasma at 30-40 W power in a reactive ion etcher with a pressure of 40 mtorr and 50 sccm flow rate, to reduce the effect of PMMA resist contamination.

The principle of fabrication procedure is illustrated in Fig. 4.1 where the aluminium film is evaporated first from an angle, then the surface is oxidized in situ inside the vacuum chamber, by letting some amount of pure oxygen inside to create a good quality tunneling barrier made out of alumina, and finally the another metal is deposited from zero angle on top of the oxidized aluminium. The resist mask shadows the evaporation from different angles leading to metal deposition only at specific locations on the chip. A SEM image of a final tunnel junction is in the Fig. 4.2 and the same structure is illustrated as a scheme in Fig. 4.3. The bonding pad geometry is illustrated in Fig. 4.4.

Variations in samples in this thesis come from using different metals and different vacuum evaporators. Totally three different metal evaporators with differing base pressures were used. More importantly contamination of other particles is expected to be increased in evaporators where "dirty" materials were heavily used.

The model of the first evaporator is Edwards Auto 306 and the second is Balzers Baltec BAE 250. Chambers in both evaporators were pumped into a high vacuum ($\sim 10^{-5}$ mbar) region with their turbomolecular pumps, but the overall purity differed. Balzers is in heavy use and is then expected to be much dirtier than Edwards, which has been in negligible use in other than in this project. From now on they will be called evaporators HV1 (Edwards) and HV2 (Balzers), respectively. These evaporators don't have a separate loading chamber but rather have an easily opened evaporation chamber. The dirtiness of HV2 is sometimes witnessed immediately after clamping a plain clean silicon chip on the sample holder as dust collecting on the

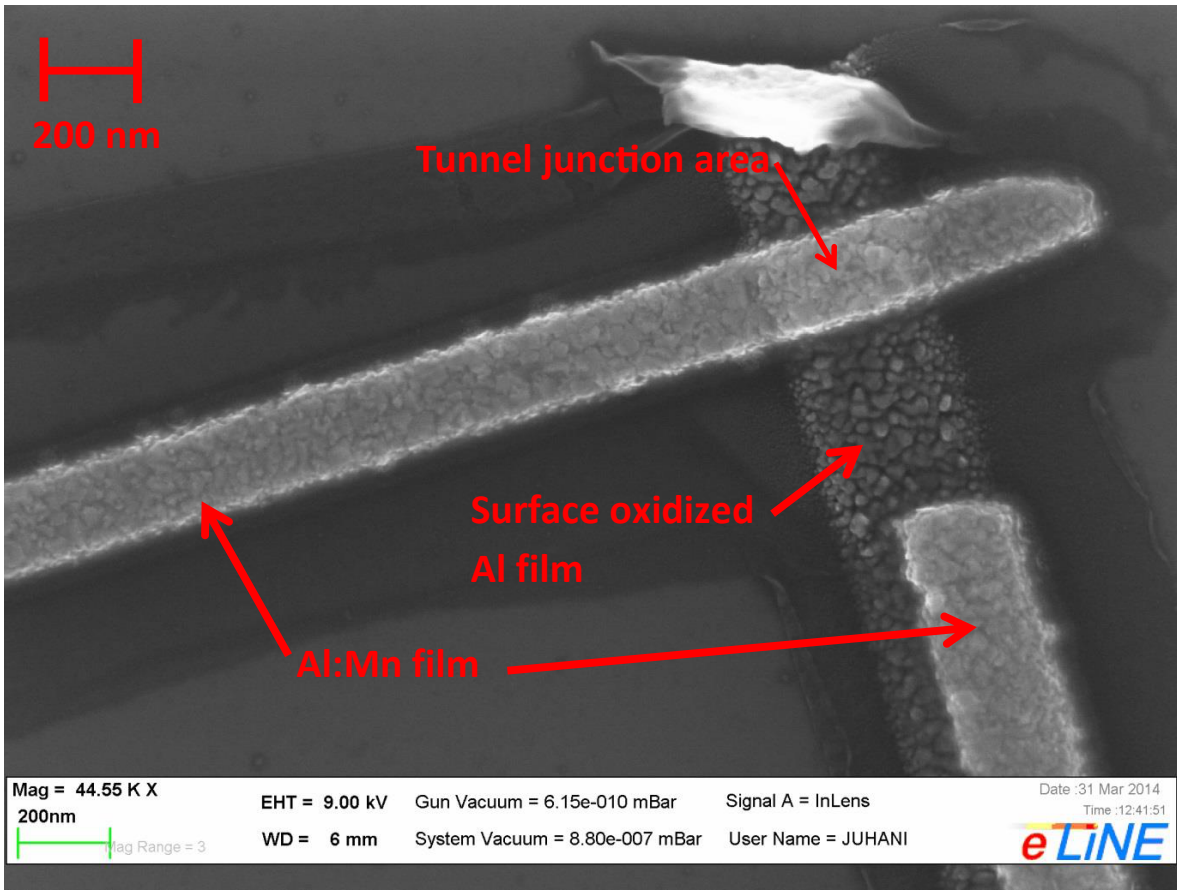

FIGURE 4.2 A SEM image of the junction area in an Al–AlO_x–Al:Mn sample. Tunneling takes place through the insulator between the intersection of the two materials.

surface of the chip.

The third evaporator is also based on electron beam heating, but is capable of pumping the chamber down to ultra-high-vacuum region ($\sim 10^{-9}$ mbar) with its turbomolecular pump and cryopump. A separate loading chamber is used to prevent unnecessary venting of the evaporation chamber and the set of evaporated materials was mostly limited to non-dirty ones, thus the cleanliness is expected to be superior. This evaporator will be called UHV. All niobium based junctions were fabricated in there since it's the only one having enough electron gun power to evaporate niobium.

4.1 Niobium-based samples

A drawback in aluminium-based superconducting devices is the necessity of low temperatures less than the critical temperature of ≈ 1.5 K, so an obvious improve-

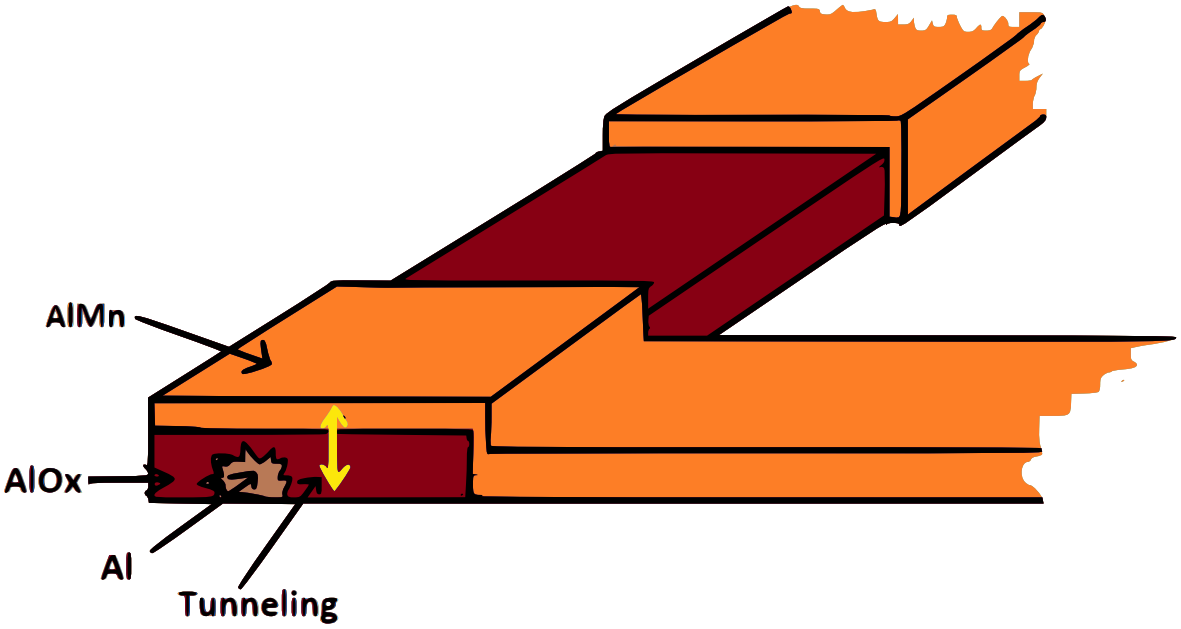

FIGURE 4.3 A schematic drawing of a tunnel junction similar to that in Fig. 4.2. The AlO_x layer completely covers the aluminium film beneath it only allowing electric current via tunneling.

ment is to move to niobium-based devices, since niobium has the highest critical temperature of all elemental superconductors. Another advantage in higher temperature superconductors is a larger energy gap ($\Delta \propto T_C$) that e.g. increases the cooling power in SINIS coolers [14].

The author fabricated Nb–AuPd–Nb superconductor–normal metal–superconductor (SNS) junction based bolometer devices used in article [A.IV.] (Ref. [54]). One of the used devices is illustrated in Fig. 4.5, where the normal metal (AuPd) nanowire in the middle is connected with three superconducting leads (Nb) thus creating two SNS Josephson junctions with different normal metal lengths. The longer junction is working as a resistive heater, while the other is short enough to support a non-dissipative supercurrent, i.e. Cooper pairs can diffuse though the normal part as a coherent supercurrent, where the measured critical current switching as a function of temperature can be used as a thermometer. The sample with superconducting leads made of Nb was studied since its larger energy gap and thus smaller quasiparticle heat conductivity.

Fabrication of niobium junctions with a thin tunneling barrier is, unfortunately, not so straightforward. Deposition of niobium is tricky because of its really high evaporation temperature, leading to problems when the evaporated niobium reaches the surface of other materials. For example, in fabrication of tunnel junctions, the hot niobium easily penetrates through the aluminium oxide supposed to be a tunneling

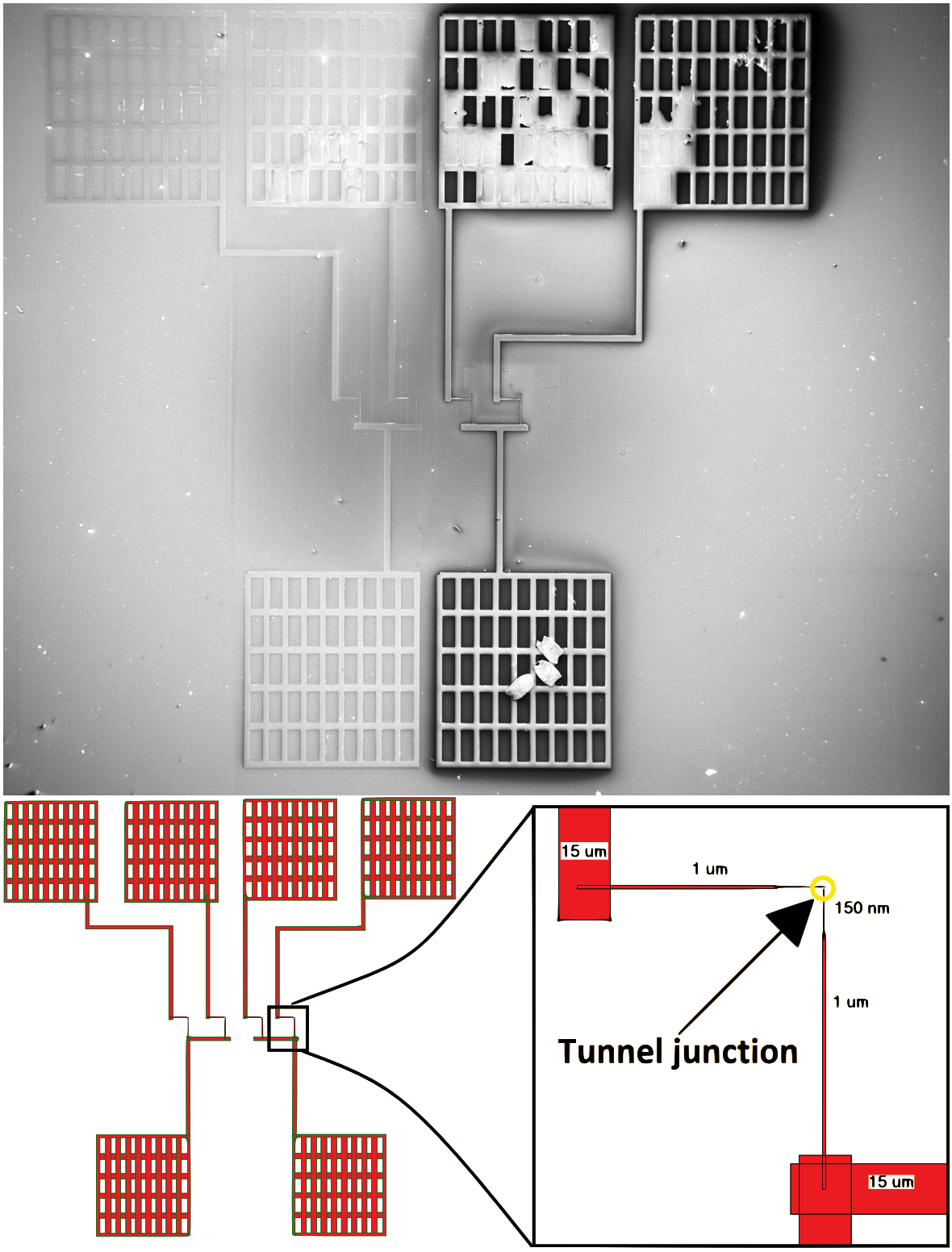

FIGURE 4.4 Top: SEM image of the sample geometry used in the noise bridge measurement setup (Fig. 3.3), where two junction are connected in series with a contact between them. The big rectangular boxes with a grid pattern are bonding pads. Tunnel junctions are too small to be visible in the picture. Bottom: The CAD pattern used in the electron beam lithography with an inset enlargement of the small structure around the tunnel junction.

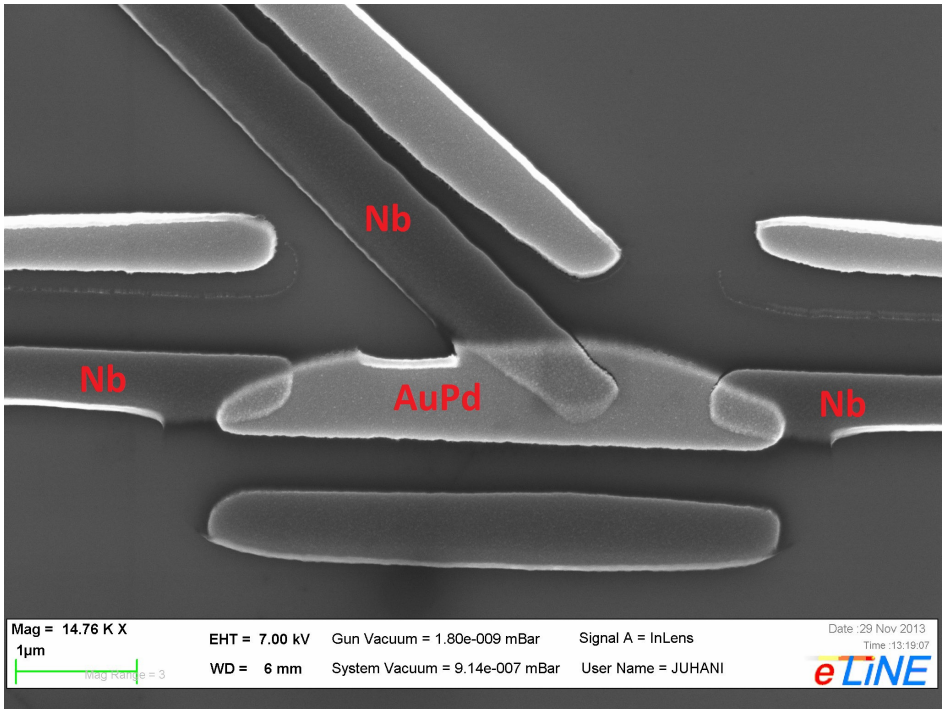

FIGURE 4.5 A scanning electron microscope (SEM) image of a superconducting bolometer device based on Nb–AuPd–Nb SNS junctions used in article [A.IV.]

barrier, leading to an ohmic contact through a junction. The barrier thickness increases as the oxygen pressure or oxidation time are increased, but it will also soon saturate. It was found that not even hours long oxidation is enough to create an oxide layer thick enough to sustain niobium evaporation.

One solution to overcome the issue of hot niobium penetrating the barrier is to deposit niobium first, and then to use multi layer evaporation to deposit directly aluminium and thermal oxide layer to cover the niobium within the tunneling area and finally evaporating another metal (e.g. Cu) on the top to have a Nb–Al–AlO_x–Cu junction [55]. However, I found that covering the niobium film properly with aluminium oxide was problematic and led to samples that showed a direct ohmic contact bypassing the oxide barrier. The reason for this failure was not clear, as similar idea was used before in our group successfully for Nb NIS-junctions fabrication [55]. Another drawback with depositing Nb first is that the barrier must be formed from AlO_x, requiring a $\sim$ 10 nm Al layer, forming a contact with Nb. This degrades the superconductivity properties at the junction due to proximity effect [55].

These difficulties were solved by a dual aluminium deposition and consequent oxidation fabrication protocol [56, 57] where niobium is evaporated last. First, two layers of aluminium were evaporated such that after both depositions the surface was oxidized. This produces one thick oxide layer that the evaporated niobium can-

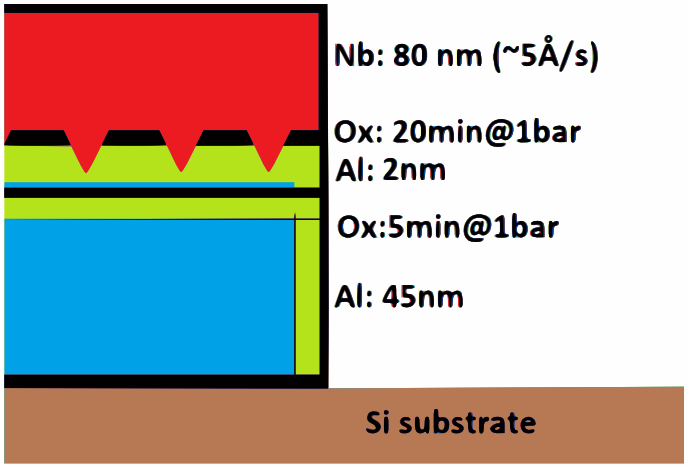

FIGURE 4.6 The receipt for successful Al–AlO_x–Nb sample fabrication; two aluminium film depositions with oxidizing them both leading to a thicker oxide layer that the evaporated niobium can't fully penetrate.

not completely penetrate, leading to a fully functional Al–AlO_x–Nb tunnel junction (see Fig. 4.6).

The thickness of the first aluminium deposition was 45 nm, which was then oxidized for 5 minutes in 1 bar pressure of pure oxygen. The second aluminum layer was 2 nm thin and oxidized for 20 minutes in 1 bar, assumed to be oxidized all through. The third deposition was 80 nm of niobium on top, with an evaporation speed of 0.5 nm/s. The linewidth was measured to be about 600 nm and tunneling resistance about 50 kΩ. This R_T is of the same order of magnitude than what was achieved with other similar, non-niobium junctions with a single oxidation method. This is an indication that the final effective tunneling barrier thickness is not much larger despite the dual oxidation. A SEM image of the sample is shown in Fig. 4.7.

4.2 Aging and annealing

Despite pure, high quality materials and vacuum conditions used in sample fabrication, standard AlO_x based junctions are not ideal and typically show aging (slow increase of tunneling resistance in time), due to the dynamics of interfacial electronic traps or other type of two-level systems with wide distribution of relaxation times [58]. Other groups have used, for example, epitaxially grown AlO_x barriers to improve their quality [59, 60] and use of molecular beam epitaxy [61] grown Al might also bring benefits.

It was shown before for Al–AlO_x–Al junctions [62] that thermal annealing speeds up this process and stabilizes junctions where a characteristic large increase

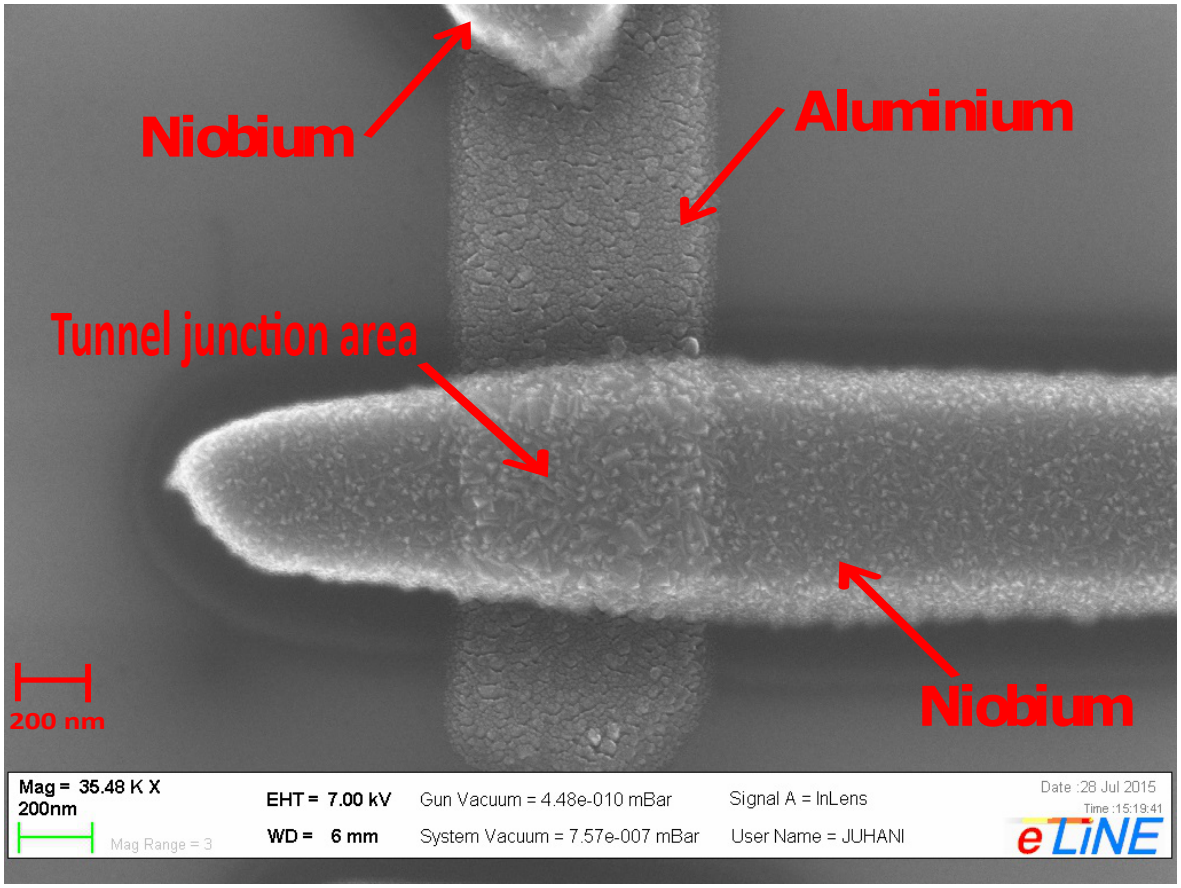

FIGURE 4.7 A scanning electron microscope (SEM) image of an Al–AlO_x–Nb tunnel junction.

in tunneling resistance was seen. Here, the same annealing method was used for similar Al–AlO_x–Al junctions as before, but also for NIS junctions where the normal material is not aluminium.

The annealing furnace (Fig. 4.8) is based on a tubular boron nitride resistive heating element located in a high vacuum chamber. The heater's temperature of 600 °C was maintained with a PID controller. The sample was connected to a manipulation rod (see Fig. 4.9) and pushed inside the heater while monitoring the sample stage's temperature with another thermocouple. After reaching the maximum temperature of 400 °C the sample was pulled out from the heater and left inside the vacuum chamber for cooling down. A typical temperature–time diagram of the process is illustrated in Fig. 4.10. In this kind of rapid thermal annealing treatment, it may be important to have a slow cooldown that allows time for the structure to relax into equilibrium.

In this thesis, the annealing furnace was physically different than the one used in Ref. [62], but with the same parameters, the results for the stabilization and char-

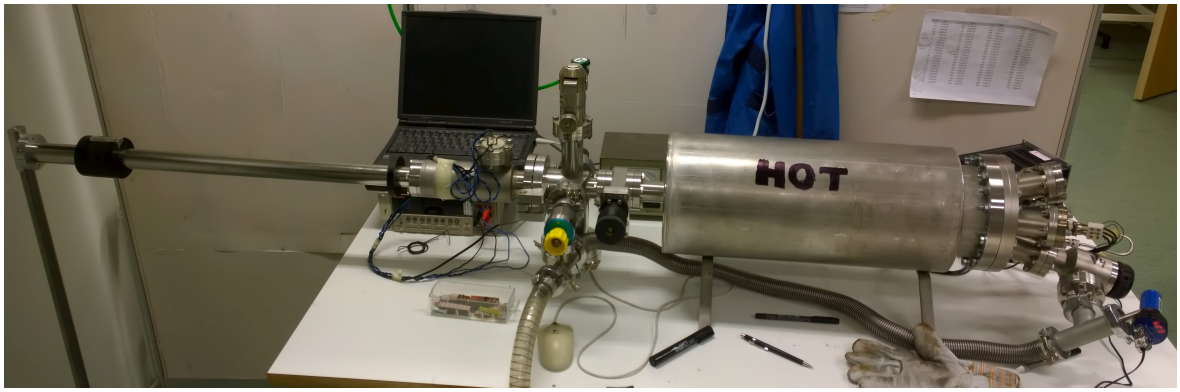

FIGURE 4.8 The annealing furnace. The loading chamber with actuating rod is in the left while the heater is inside the big vacuum chamber.

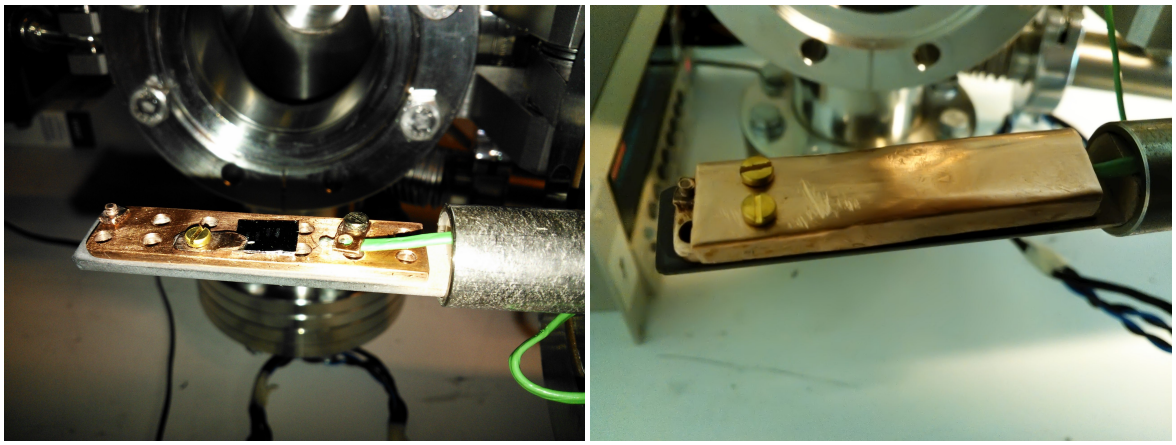

FIGURE 4.9 The sample clamped on a sample stage and covered with a shield in preparation to putting it into the annealing furnace. Under the copper plate in the sample stage is a ceramic mounting to the rod to minimize the thermal conductivity, i.e. extending the cooldown time.

acteristic tunneling resistance increase were reproduced for Al–AlO_x–Al junctions.

The annealing procedure at 400 °C was used for NIS junctions as well, with a few commonly used materials as the normal metal while still having the oxidized aluminium film as the first electrode underneath. The only accurate test for detecting the presence of a tunnel junction requires cooldown below the critical temperature of aluminium which was considered to be too time consuming for all the different material combinations. Thus, a simple analysis based on room temperature tunneling resistances were used. Within the used sample geometry and oxidation parameters, a room temperature tunneling resistances were normally > 7 kΩ, and a resistance less than a 1 kΩ was considered to be an ohmic contact, with resistance coming from the long narrow leads. In this simple test, resistances from approximately 5 kΩ to a few hundreds of kΩ were expected to represent a good tunnel

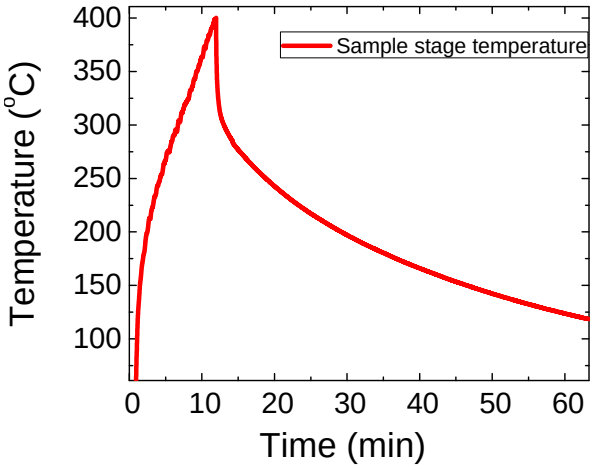

FIGURE 4.10 The annealing temperature as a function of time. The heater was set at constant 600°C and the sample heated up to 400°C before pulling it out.

TABLE 4.1 The resistivity change in ≈ 100 nm wide and ≈ 30-150 nm thick wires made out of different materials after annealing at 400 °C.

Material	Wire resistance change
AuPd	(1.6 ±0.6)%
Al:Mn	(65 ±5)%
Ag	(910 ±70)%
Au	(1060 ±80)%
Al	(-30 ±5)%
Cu	(218 ±8)%

junction.

Results varied a lot between different kinds of NIS samples. Annealing of Al–AlO_x–Cu devices lead to shorting of all the junctions, i.e. ohmic contact with no tunnel barrier. Annealed Al–AlO_x–Ag junctions had resistances > 5 MΩ or mostly open contacts. It should however be pointed out that there were similar open contacts in non-annealed silver junctions also. This can be a problem with adhesion of silver to AlO_x surface. The adhesion was also improved with a thin layer of titanium (~ 3 nm) between the insulator (AlO_x) and a normal metal (Ag). Using this technique, Al–AlO_x–Ti–Ag junctions were fabricated, but the annealing still resulted in a breakdown of the junctions, seen as either a shorted contact, or a really high resistance (open contact). Similarly Al–AlO_x–Ti–Cu samples showed a shorted contact with resistances much less than 1 kΩ.

A few Al–AlO_x–AuPd samples showed an almost promising resistance of approximately 2 kΩ after annealing, but since their resistances decreased when lowered into liquid nitrogen they were considered not as junctions (tunneling resistance increases at low temperatures). Al–AlO_x–Ti–AuPd devices produced the same results as the ones without the thin titanium layer.

Al–AlO_x–Au samples all ended up as open contacts after annealing. The adhesive layer of titanium was also used with gold, but Al–AlO_x–Ti–Au samples now resulted with a small resistances < 1 kΩ.

Aluminium itself was also tested as a thin (~ 3 nm) adhesive layer in Al–AlO_x–Al–Cu junctions. Also here junctions had their resistances drop < 1 kΩ after anneal-

ing.

The reason for all these negative results remains unknown, as we didn't pursue yet these issues further. We do know that annealing didn't destroy films without tunneling barriers, as shown in Table 4.1, albeit the change in resistance was interesting in many cases.

Only Al–AlO_x–Al:Mn based NIS junctions survived the annealing with almost a 100% yield. This is likely not a coincidence. Somehow a small concentration ($\sim 10\%$) of manganese is not making a big difference in what comes to the surfaces phenomenon in the heat treatment.

For the Al:Mn-junctions, there was an increase in tunneling resistance after annealing, just like for Al–AlO_x–Al junctions. The stabilization is quite successful since the tunneling resistance remained almost unchanged even when measured years after annealing, meanwhile non-annealed samples suffered from resistance increase. The aging was strongest in non-annealed HV1 fabricated samples and the second strongest predictably in non-annealed HV2 samples. The aging data is shown in Fig. 4.11 [A.II].

For comparison, UHV-fabricated Al–AlO_x–Al samples don't age so significantly even without annealing, that is because of the use of cleaner metal deposition environment. Interestingly, resistance decrease in time was detected in some annealed samples, but the change has been small.

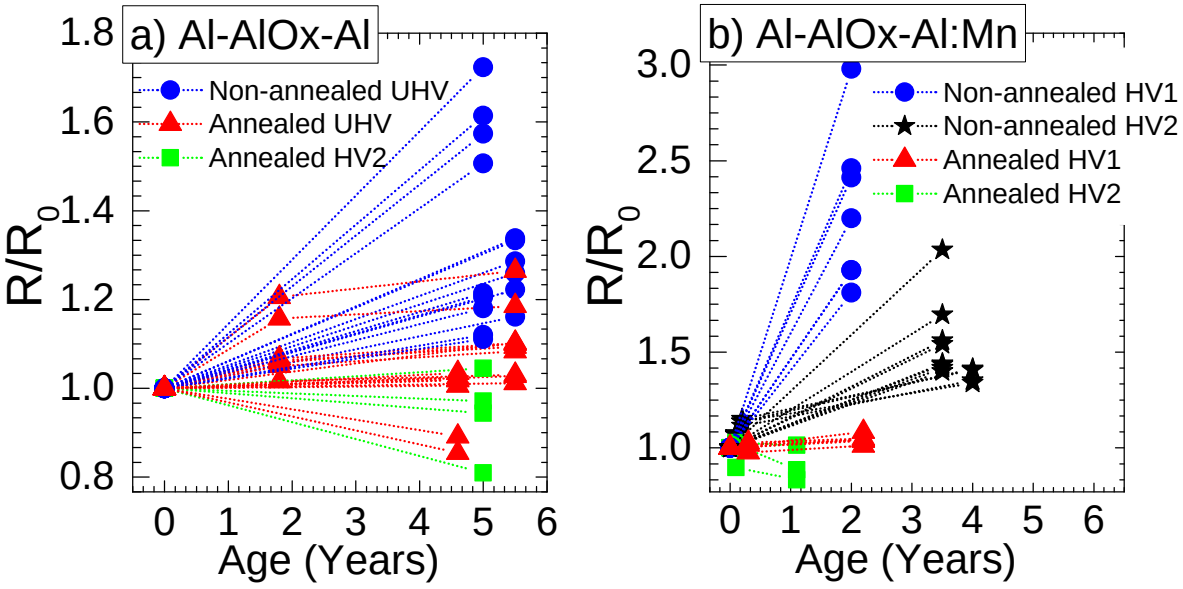

FIGURE 4.11 Measured room temperature tunneling resistance change as a function of time for a) Al–AlO_x–Al and b) Al–AlO_x–Al:Mn samples fabricated in UHV, HV1 and HV2 evaporators, with and without annealing. Here the aging of non-annealed samples is evident, although not that pronounced for UHV-fabricated Al–AlO_x–Al samples. On average, annealing reduces aging in all samples, but there is lots of dispersion in the data. Note: The data points are connected with lines to visualize the change, but the effect is not linear.

Chapter 5

Cryogenics

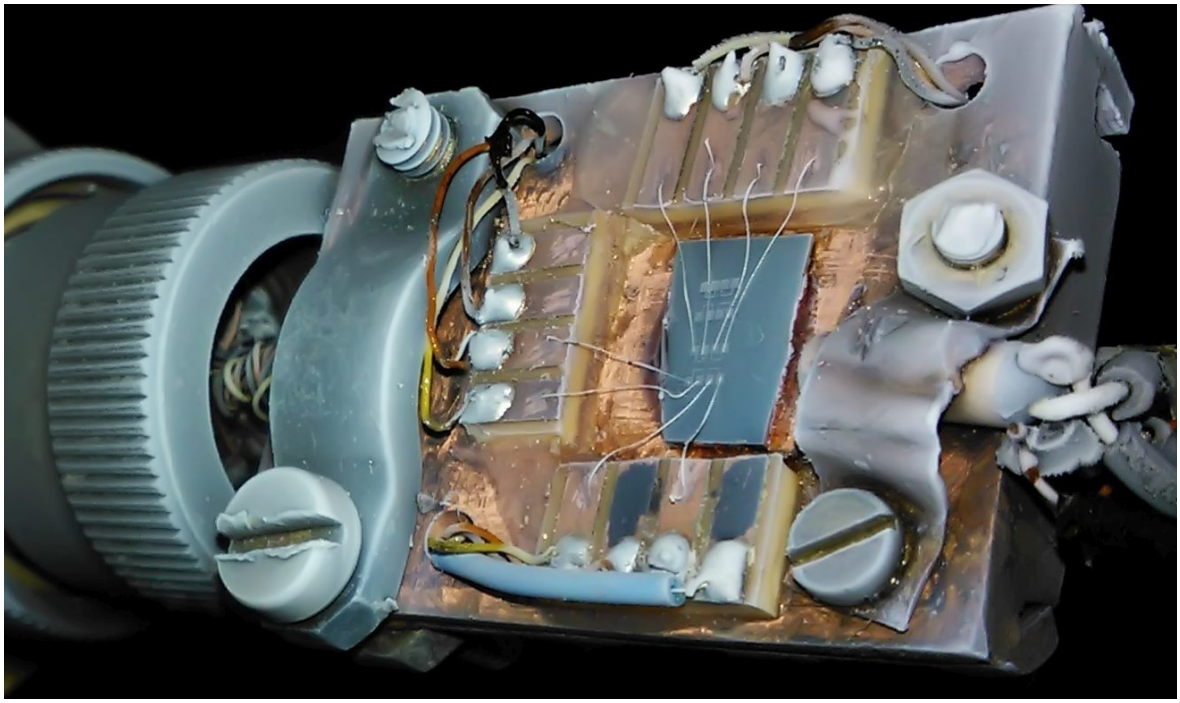

FIGURE 5.1 A chip attached to a sample stage. Thin aluminium wires, the bonding wires, electrically connects the device on the chip to the cryostat's wiring.

Samples were measured at temperatures varying from ≈ 50 mK to room temperature. Room temperature measurements were justified as $1/f$ noise is highly positively temperature dependent, thus a higher noise signal is seen at room temperature for accurate comparison between samples. In all other measurements cryogenics were largely involved.

The simplest cooling device is a dipstick with a sample and a thermometer attached at one end, as illustrated in Fig. 5.1. This rod is then lowered into liquid

helium at temperature of 4.2 K. Since the sample stage is not shielded from the refrigerant, it is in contact everywhere with the sample, thus thermalizing the sample well to that temperature. If higher temperatures are needed, the sample stage can be lifted upwards above the liquid surface, exploiting the temperature gradient of helium gas inside the dewar. There is also a resistive heater element mounted. The temperature of 4.2 K is enough to check for example niobium's critical temperature, but for most measurements much lower temperatures are needed.

Lower temperatures were achieved with a ^{3}He–^{4}He dilution refrigerator. This type of cryogenic cooler provides continuous cooling power at lowest temperatures due to the heat of mixing of ^{3}He and ^{4}He isotopes [63]. At temperatures below approximately 870 mK, the mixture spontaneously separates into two phases and forms both a ^{3}He rich and a ^{4}He rich phase. Because of a boundary between the phases, addition of energy is required for particles to go from one phase to another (endothermic process), thus the cooling power.

A cryostat, illustrated schematically in Fig. 5.2 and in real life in Fig. 5.3, consists of multiple precooling stages before a phase separation can initiate in the coldest part of the cryostat. The whole thing is first immersed into liquid helium, which is the 4.2 K cooling stage. After thermalization to that temperature, the vacuum jacket (not present in Fig. 5.3) is pumped to isolate the inner parts from the "hot" 4.2 K bath.

The next cooling step is achieved by pumping on a separate ^{4}He chamber called the pot, where the cooling is achieved due to the latent heat of the evaporated liquid. The lowest achievable temperature is limited by the decrease of vapour pressure, in the case of ^{4}He the pot temperature is lowest around 1.2 K. To make the evaporative cooling continuous, more ^{4}He liquid is fed into the pot through a small siphon.

Finally there is a mixing chamber, which connects to the sample stage, but the spontaneous phase separation requires lower starting temperatures than what the 1.2 K pot pumping can achieve. That's why the mixing chamber is connected to a still, another chamber that is also pumped to cool it down evaporatively, but now there is ^{3}He present, and since it has much higher vapor pressure than ^{4}He, it cools down to lower temperatures and the phase separation can start.

The pumped (mostly ^{3}He) gas from the still is recycled back to the mixing chamber to have a continuous operation. Before entering the mixing chamber, the ^{3}He gas is cooled down in heat exchangers in contact with all the precooling stages. Narrow diameter tubes, impedances, are used to adjust the flow rate of liquids between the different parts in the design that has a big effect on the cooling power.

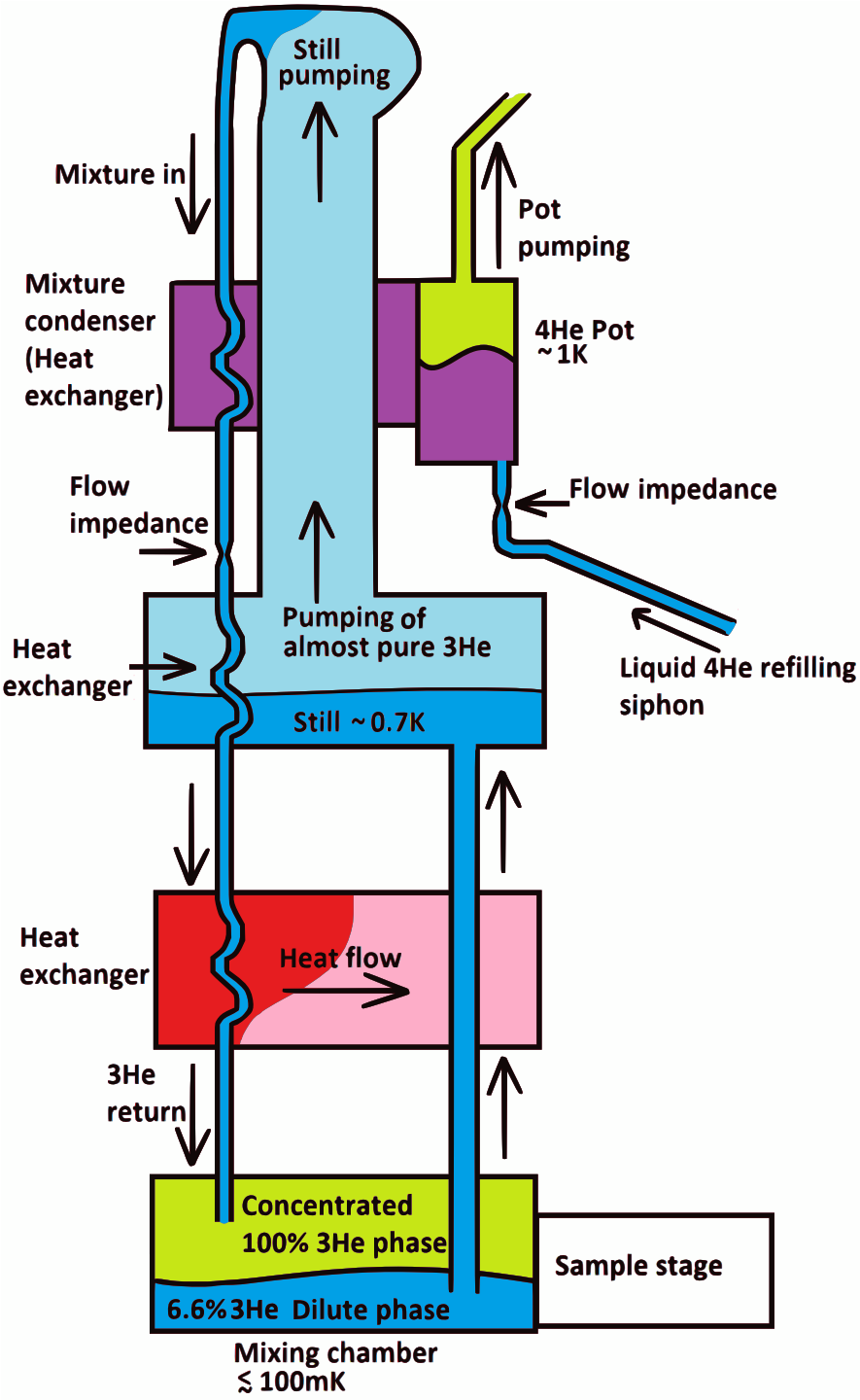

FIGURE 5.2 Schematics of a ^{3}He–^{4}He dilution refrigerator. The ^{3}He–^{4}He mixture has a special property at low temperatures where it separates into two phases. The practically pure ^{3}He phase is on top of a more dense ^{4}He rich dilute phase in the mixing chamber. Circulated ^{3}He atoms require energy to move through the phase boundary, that is taken from the environment, hence the cooling power.

FIGURE 5.3 A ^{3}He–^{4}He dilution refrigerator. A sample stage is the lowest part, that is covered inside a radiation shield. All the cooler technology, electrical wiring and pumping lines are tightly packed inside the body. A vacuum jacket is not in place.

Chapter 6

Effect of annealing on the 1/f noise in Al–AlO_X–Al tunnel junctions

The first article [A.I.] is about annealing of Al–AlO_x–Al junctions. These samples were fabricated in two different evaporators, HV2 and UHV. Two different substrates were used; oxidized and nitridized silicon, but no difference was found between the two in the measurements.

Annealing treatment at 400 °C was performed for samples as explained in Chapter 4.2. Also here the stabilization of junctions was demonstrated with a similar characteristic resistance increase as seen in the previous paper, Ref. [62]. The room temperature tunneling resistance increase after the annealing process varied between 10–45% for the UHV fabricated samples, and 200–300% for the HV2 fabricated samples.

Low-frequency $1/f$ noise was measured from HV2 and UHV fabricated samples, both before and after annealing. Several different samples were measured to achieve statistical consistency of the results. As explained in Chapter 3.8, the measured voltage noise was converted to resistance noise S_R and normalized with R_T^2, thus scaling the noise to be independent on the sample resistance. The S_R/R_T^2 noise from different samples depended only on the used evaporator and the annealing status (see Fig. 6.1). Unsurprisingly, the UHV fabricated samples showed a smaller noise level than the dirtier HV2 samples, but interestingly, after annealing noise from all the samples reduced to the same level. Reduction of $1/f$ noise in HV2 samples was expected, but clearly, there was room for improvements also for the UHV samples, even though they were fabricated in cleaner conditions.

Differential conductance measurements (Fig. 6.2) didn't show any significant difference before and after annealing. That makes the $1/f$ noise measurement an accurate way to probe the quality of the junction already at room temperature.

The temperature dependence of the $1/f$ noise was studied for non-annealed

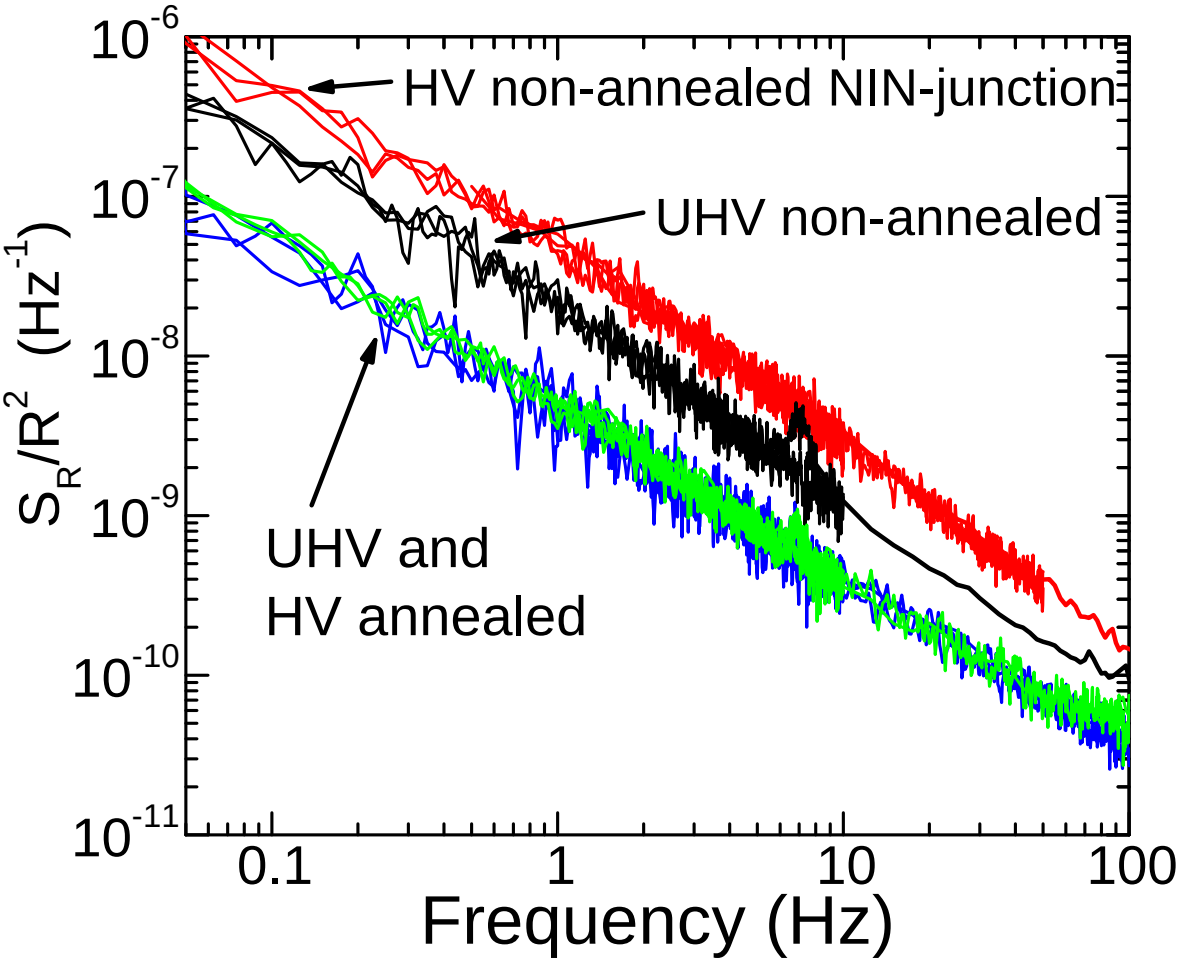

FIGURE 6.1 (a) Room temperature resistance noise spectral densities of four double tunnel junction samples fabricated in HV2 and UHV before ($R_T^{HV2} = 49\,\&\,59\,\mathrm{k\Omega}$, $R_T^{UHV} = 23\,\&\,21\,\mathrm{k\Omega}$) and after ($R_T^{HV2} = 155\,\&\,172\,\mathrm{k\Omega}$, $R_T^{UHV} = 33\,\&\,34\,\mathrm{k\Omega}$) annealing at $400\,^\circ$C. The data is normalized with R_T^2. After annealing, the spectra are well fitted by $S_R/R^2 = 0.45 \cdot 10^{-8} f^{-1.05}$ 1/Hz.

and annealed samples between liquid helium temperature (4.2 K) and room temperature, at various different temperatures. The average noise level (there is noise in the noise) at a frequency of 10 Hz, was studied. A lower frequency could have been used to measure a higher noise level, however capturing a low frequency spectrum takes longer time, and it is harder to keep the cryostat stable at higher temperatures. Therefore, quicker time series at higher frequencies was used. This may, however, show some error in the datapoints at the lowest temperatures around 4.2 K, since the $1/f$ noise is getting already quite flatter at those temperatures, see Fig. 6.3(a).

The temperature dependence is illustrated in Fig. 6.3(b), where a linear dependecy in $1/f$ noise level is clearly seen below 200 K, but changing to a strong increase at higher temperatures close to the room temperature. The result is in agreement

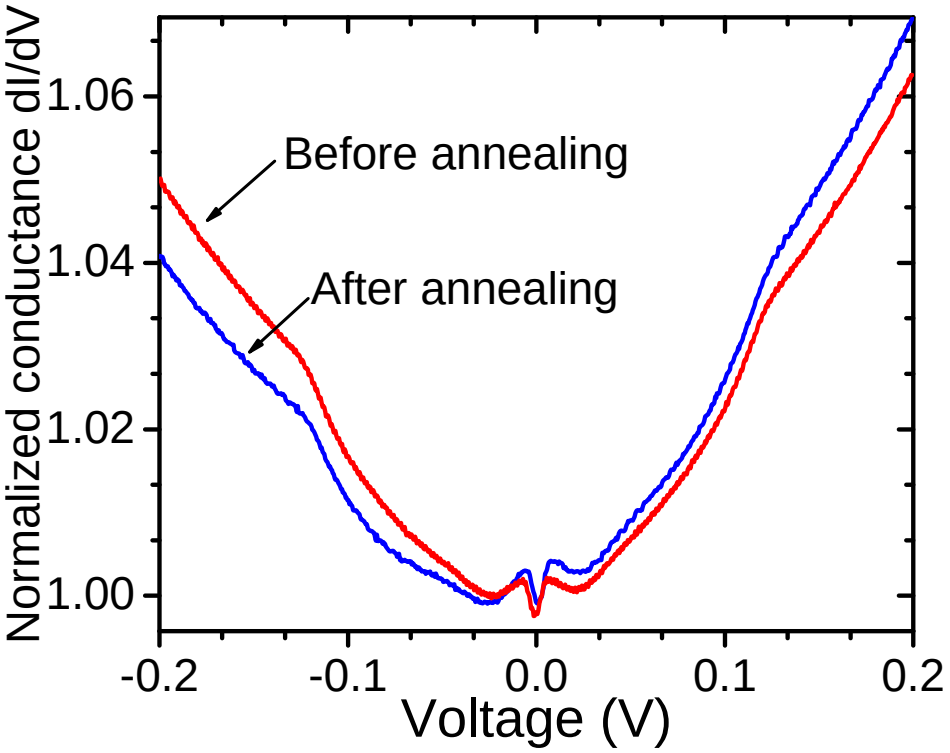

FIGURE 6.2 Conductance spectrum of a UHV sample before ($R_T = 12\,\mathrm{k}\Omega$) and after ($R_T = 18\,\mathrm{k}\Omega$) annealing, demonstrating minor changes in it. The sharp dip around $V = 0$ is due to Coulomb blockade at 4.2 K.

with other works [64, 65] on submicron Al–AlO_x–Al junctions, both in terms of the temperature dependence and the level of noise.

In Ref. [64] an empirical formula was suggested for the $1/f$ resistance noise in Al–AlO_x–Al junctions

$$S_R/R^2 \sim \frac{1}{A/\mu\mathrm{m}^2}\left(\frac{T}{1\mathrm{K}}\right) 1/f \cdot 10^{-13}\mathrm{Hz}^{-1}. \tag{6.1}$$

Although in rough agreement with our data, we point out our observations that the level of $1/f$ noise can change in annealing, that proves no universal formula exists.

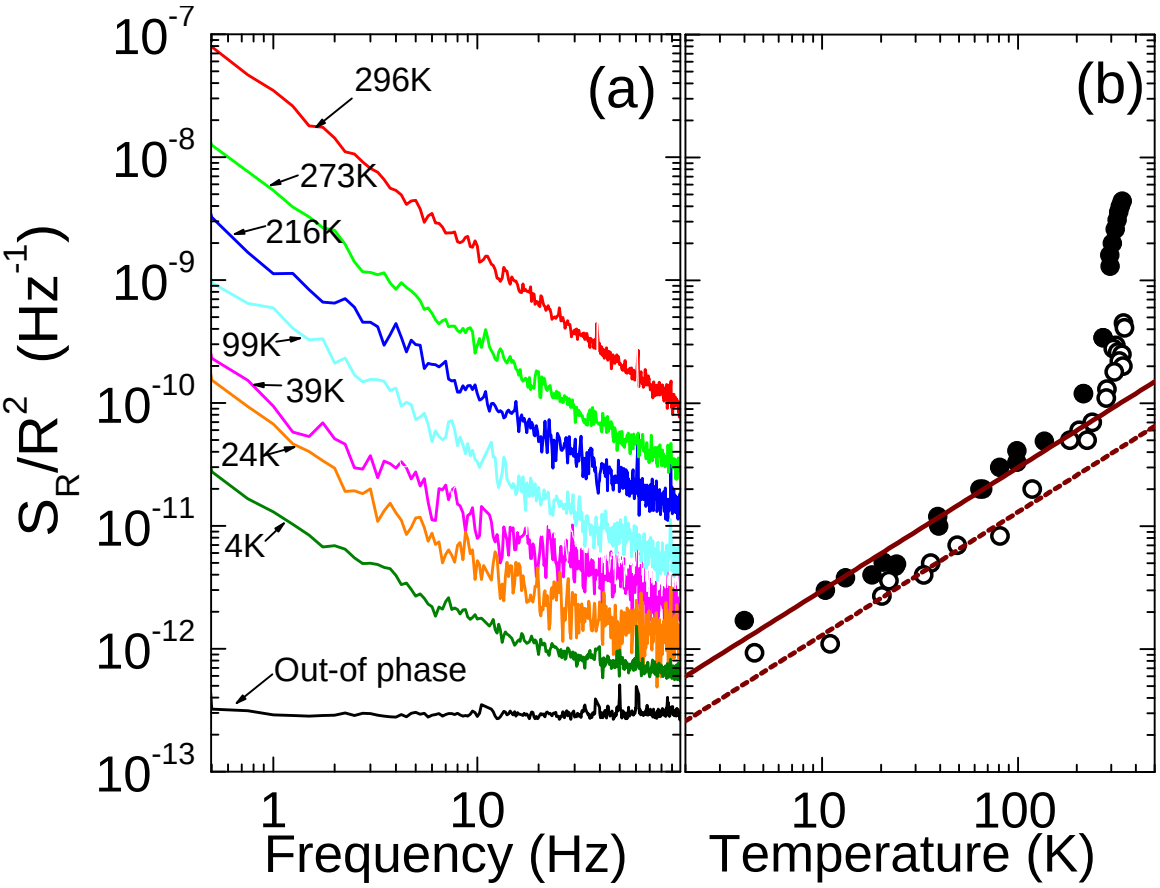

FIGURE 6.3 (a) Temperature dependence of the normalized $1/f$ resistance noise in non-annealed tunnel junctions (data from two samples with $R_T = 19\,\&\,18\,\mathrm{k}\Omega$). The lowest spectrum is the out-of phase component measured at 4 K demonstrating the baseline of the measurement setup. (b) Noise level at 10 Hz s as a function of temperature. Solid circles represent the non-annealed tunnel junctions ($R_T = 19\,\&\,18\,\mathrm{k}\Omega$), and open circles the annealed junctions ($R_T = 4\,\&\,8\,\mathrm{k}\Omega$). The lines are fits to linear temperature dependence $S_R/R^2(10\,\mathrm{Hz}) = AT$ with $A = 1.3 \cdot 10^{-13}$ and $A = 3 \cdot 10^{-13}$ $1/(\mathrm{HzK})$.

Chapter 7

Effects of annealing on the 1/f noise and subgap current in Al–AlO_X–Al:Mn tunnel junctions

The annealing study of Al–AlO_x–Al NIN junctions (article [A.I.]) raised a question about annealing NIS junctions, since in many applications (e.g. thermometry and coolers) normal metal–insulator–superconductor junctions are needed. The answer was article [A.II.], where NIS junctions made with the most commonly used normal metal materials were used with alumium as a superconductor, and in-situ oxidized alumina as the barrier. As explained before in Chapter 4.2, only Al–AlO_x–Al:Mn based NIS junctions showed good results in annealing so they were chosen for a closer examination.

Since manganese was not available in the clean UHV-evaporator, only HV1 and HV2 were used in the sample fabrication. The source material had a 2% nominal atomic concentration of manganese. The junction size was kept quite constant, around 200x300 nm, with tunneling resistances varying typically between 10–100 kΩ. The resistance increase after annealing was still present here, on the average by 80 % for HV1 and by 400 % for HV2, but there was lots of variation between samples, much more than with the Al–AlO_x–Al devices.

7.1 1/f noise in Al–AlO_X–Al:Mn tunnel junctions

The same low frequency noise study that was used for Al–AlO_x–Al samples is repeated here. $1/f$ noise was studied before and after annealing for Al–AlO_x–Al:Mn tunnel junctions. Most of the results were done at room temperature to maximize the already faint noise signal. Temperature dependence of noise at 10 Hz was also

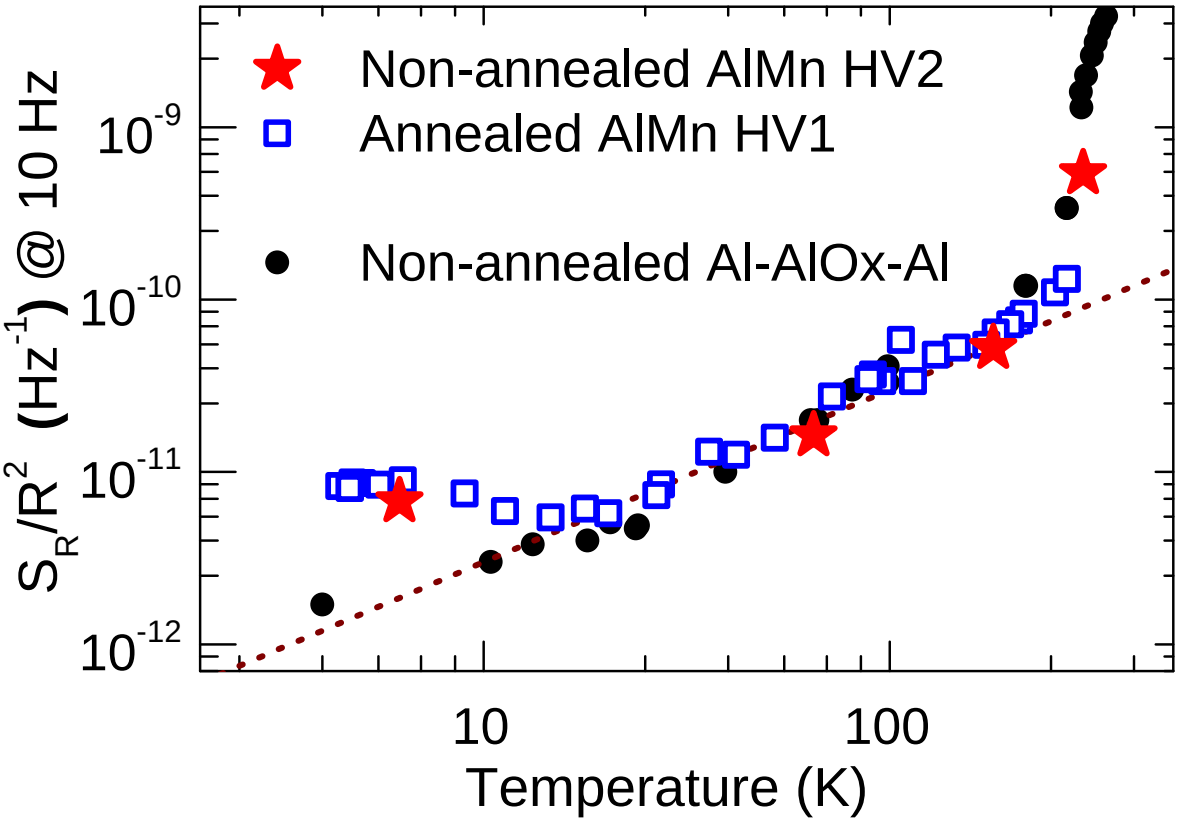

FIGURE 7.1 Temperature dependence of the $1/f$ noise in annealed Al–AlO_x–Al:Mn junctions made in HV1, similar non-annealed junctions made in HV2 and Al–AlO_x–Al junctions made in UHV.

measured down to 4 K, illustrated in Fig. 7.1. It shows a linear increase in the noise level as the temperature increases, just as it was found also in Al–AlO_x–Al junctions. The saturation and higher level of noise in Al:Mn junctions compared to Al junctions at lowest temperatures (< 10 K) is the only detectable difference in the temperature dependence between the two junction types. The result was reproducible, but it can, however, be influenced by some other noise sources, which are more prominent at low temperatures. This observation requires further study.

The room temperature $1/f$ noise measurement results before and after annealing are illustrated in in Fig. 7.2. A reduction of noise level after annealing was seen on HV1 made samples, but the normalized resistance noise levels from different annealed samples didn't normalize to the same value, but varied between different samples.

Surprisingly, $1/f$ noise was higher in non-annealed "cleaner" HV1 samples than in non-annealed "dirty" HV2 samples. After annealing, the whole situation was turned upside-down with the noise in HV1 samples decreasing well below original

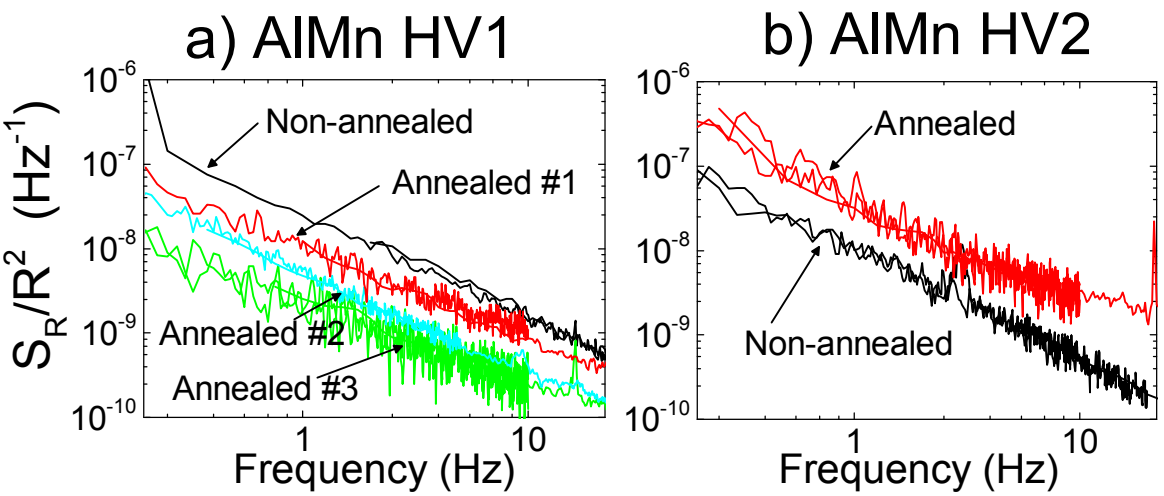

FIGURE 7.2 Room temperature resistance noise spectral densities of double Al–AlO_x–Al:Mn tunnel junction samples fabricated in a) HV1 and b) HV2 evaporators before and after annealing. The data is normalized with R_T^2. The plot represents data from different samples which were mostly consistent with each other, except in a) where it was found that the noise levels in annealed samples varied.

level of HV2 samples, while the noise in HV2 samples increased over the original HV1 level.

While looking at the plots, one might conclude that the $1/f$ noise was higher in annealed "super clean" Al–AlO_x–Al UHV samples (Fig. 6.1) than in the best annealed Al:Mn samples. However, we point out one source of possible uncertainty here: aluminium has small resistivity, thus the tunneling resistance always dominates the measured value. In contrast, manganese doped aluminium is known to be more resistive, i.e. the real tunneling resistance used in the normalization calculations could maybe be less than the one used, leading to an increase in the normalized noise level. Resistivities of separately fabricated Al and Al:Mn thin wires were also tested, with a difference of an order of magnitude. Although it is a clear increase, the total resistance of the Al:Mn wires in a sample was still estimated to be insignificant compared to the junction's tunneling resistance.

7.2 Electrical characterization of Al–AlO_x–Al:Mn NIS junctions

The current–voltage characteristics of HV1 and HV2 fabricated Al–AlO_x–Al:Mn junctions were measured at low temperatures both prior to and after annealing. Such simple DC $I-V$ measurements are a much easier task than measuring noise, but since there is the difficulty of the ^{3}He–^{4}He dilution refrigerator cooldown, only some

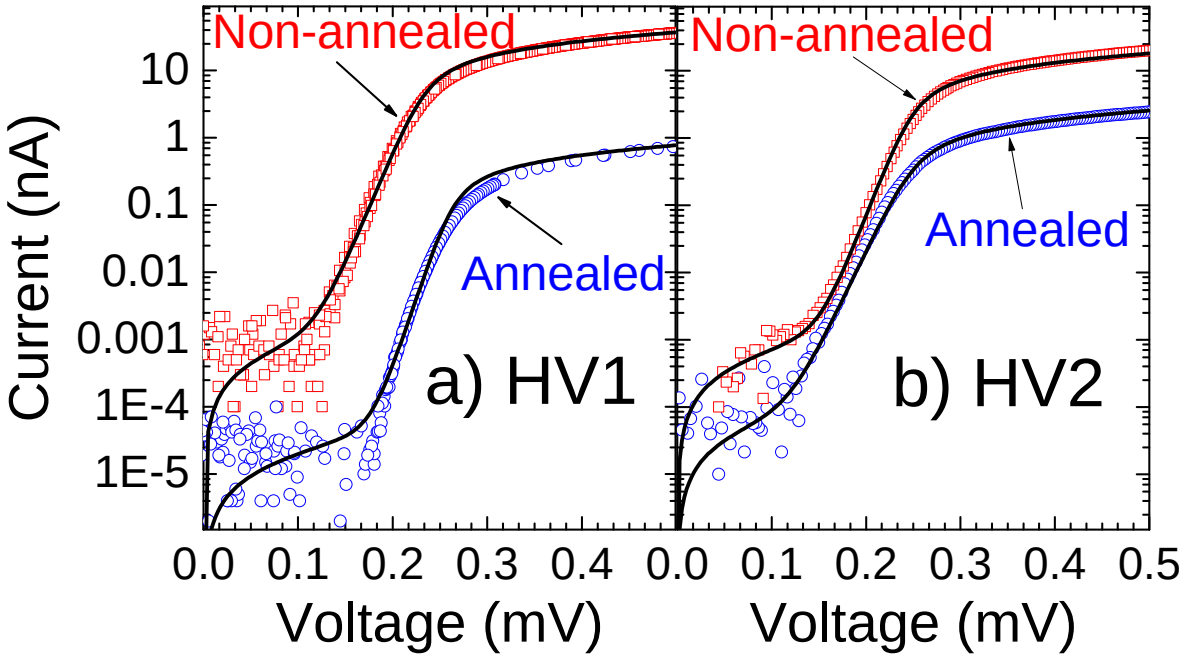

FIGURE 7.3 Current–voltage characteristics of a) HV1 and b) HV2 fabricated devices each measured at 140-160 mK before and after annealing. The open symbols denote the measured response, while the lines are the corresponding theoretical fits. Fitting to theory results in Dynes fitting parameter $\Gamma/\Delta \sim 1 \cdot 10^{-4}$ which was not significantly altered in annealing.

samples were measured.

The measurement lines in the refrigerator had two stages of filtering, pi type filters at 4 K and RC type filters at base temperature in sample stage. In addition, microwave filtering between these two types of filters was achieved with the help of Thermocoax cables of length 1.5 m. The DC current–voltage measurements were recorded with Ithaco 1201 voltage and 1211 current preamplifiers, respectively. In Fig. 7.3, such $I - V$ characteristics of a) HV1 and b) HV2 fabricated single junction devices are shown, both before and after annealing. The HV1 samples were not physically the same devices, but fabricated in the same run on the same chip, thus considered to be almost identical. The HV2 results are from the same physical junction.

Theoretical fits based on the single-particle tunneling model were made (see Chapter 2.5 about NIS tunneling), and from these fits the values of the junction temperature T, energy gap Δ, tunneling resistance R_T and Dynes parameter Γ/Δ were obtained, with the results shown in Table 7.1. The simulations match very well with the experimental data, as seen in the Fig. 7.3. The aluminium gap $\Delta_{Al} = 0.25$ meV is a bit larger than the $\sim 0.22 - 0.23$ meV what we normally measure from UHV fabricated aluminium samples in our group.

TABLE 7.1 Fitting parameters used in theoretical simulations for Al–AlO_x–Al:Mn samples

	T (mK)	T_C (K)	Γ/Δ	Δ (meV)	R_T (kΩ)
Non-ann. HV1	150	1.5	$1 \cdot 10^{-4}$	0.23	12
Ann. HV1	120	1.5	$1 \cdot 10^{-4}$	0.26	550
Non-ann. HV2	140	1.5	$1.5 \cdot 10^{-4}$	0.25	24
Ann. HV2	170	1.5	$1 \cdot 10^{-4}$	0.25	170

Annealing didn't significantly change any parameters characterizing the junction, except the increase of the tunneling resistance, of course. There were no clear changes in the values of the Dynes parameter as a result of annealing in any samples. This lack of degradation is of course a positive result. Any possible lowering of the intrinsic Γ is most likely masked by the effects of the measurement setup introducing a significant contribution due to photon-assisted tunneling [26].

7.3 Elemental analysis of Al–AlO_x–Al:Mn films

Accelerator-based elemental analysis was performed in the Accelerator laboratory at the University of Jyväskylä to "see" inside the junction films. The goal was to explain the measured electrical differences between the evaporators and the effect of annealing. For ToF-ERDA (Time-of-Flight Elastic Recoil Detection Analysis) material depth profile analysis [66], samples were fabricated using the same materials (Al:Mn and Al) and oxidation procedure than was done for actual junctions, except that the chip's surface was coated completely with the thin films, with the oxide layer between them. The analysis is destructive so the same physical samples couldn't be measured before and after annealing, but the samples were made in the same evaporation run to have identical structure and elemental content. One sample was measured as deposited while the other was annealed.

In the ToF-ERDA measurement, an ionized chlorine beam was accelerated to 7.765 MeV and was directed to hit the sample surface. Both the energy and the time-of-flight of the recoiled atoms were measured accurately, thus allowing plotting of the depth profile of different masses individually.

Unfortunately, the resolution of ToF-ERDA is not enough to probe the tunnel junction dimensions where the thin tunneling barrier is the key element and is only few nanometers thick.

Results of depth profiles of various elements are illustrated in Figs. 7.4, 7.5, 7.6 and 7.7, and average concentrations of C, H and O over the whole film are listed in Table 7.2. Different materials don't evaporate at the same rate, as is seen in Fig. 7.4

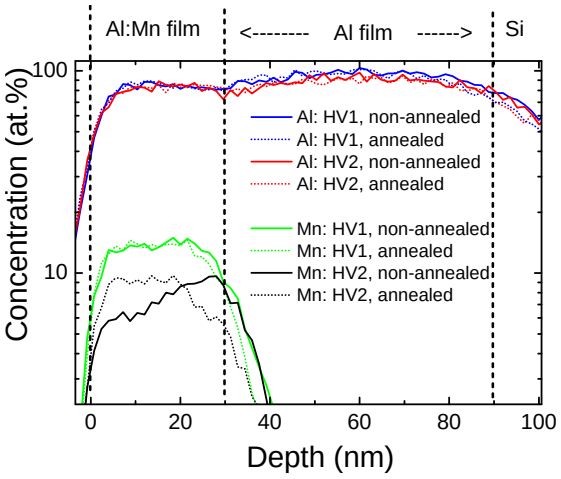

FIGURE 7.4 Aluminium and manganese concentrations as a function of film depth.

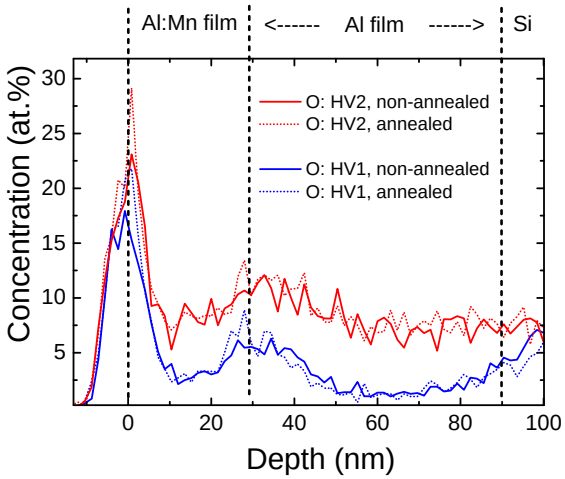

FIGURE 7.5 Oxygen concentration as a function of film depth, where can be seen more oxygen in HV2 samples.

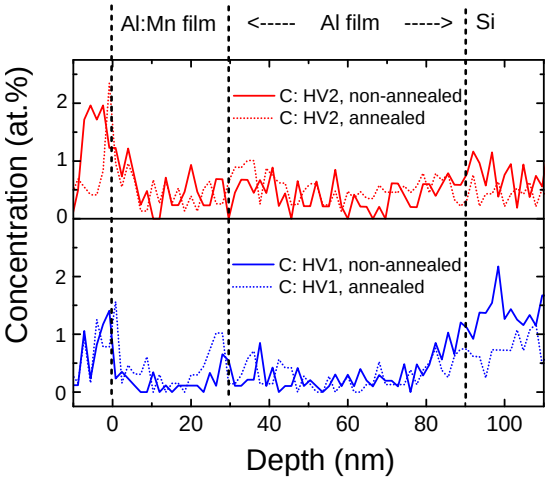

FIGURE 7.6 Carbon concentration as a function of film depth.

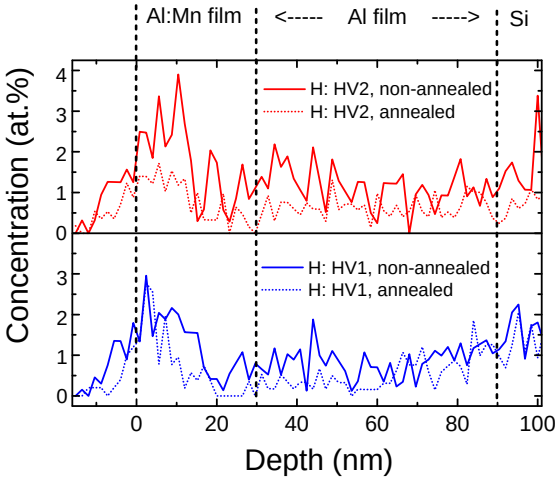

FIGURE 7.7 Hydrogen concentration as a function of film depth.

TABLE 7.2 Total average concentration of elements in samples before and after annealing with percentage change after annealing treatment.

	HV1 non-ann.	HV1 ann.	HV2 non-ann.	HV2 ann.
C (at.%)	0.401	0.3	0.398	0.334
C(change)	-25%		-16%	
H(at.%)	1.067	0.758	1.233	0.713
H(change)	-29%		-42%	
O(at.%)	3.24	2.87	5.501	5.74
O(change)	-11%		+4%	

for the manganese concentration. The measured $\sim 10\%$ Mn concentration is much more than the 2% of the source and also much higher than what would be needed to make aluminium normal [67]. A clear difference in Mn concentration is seen between the HV1 and HV2 samples, as HV1 has a higher manganese concentration. The difference between the non-annealed and annealed HV1 and HV2 samples can be explained based on the differences in evaporators. In HV1, the swept electron beam heats up the material uniformly, leading to a smooth manganese concentration in the film. This is not the case for HV2, where a stationary electron beam hits the Al:Mn target heating it up locally, evaporating more manganese in the beginning of the film than in the end. Annealing seems to reverse this concentration profile, so that in the end there is more manganese at the surface than near the barrier.

This uneven manganese concentration near the barrier in HV2 samples may be the reason for the completely opposite behavior of the $1/f$ noise after annealing as compared to what was seen for HV1 and Al–AlO_x–Al samples. The "bad" distribution of manganese still has potential for reorganization in annealing. As seen in the results, annealing slightly rearranges the concentration profile by diffusion of Mn away from the junction area. In the non-annealed HV2 samples, there is an equally nice sharp threshold between the Al:Mn film and the tunneling barrier than in the HV1 samples, which may explain the initially relatively low noise. However there is a strong change in the manganese concentration near the tunneling barrier after the annealing. This smooth slope of manganese may lead to creation of more impurity traps in the vicinity of tunneling barrier, that could lead to higher $1/f$ noise measured in such devices [58].

The aluminium concentration (Fig. 7.4) shows no major differences, it is evenly distributed and smooth. The oxygen distribution (Fig. 7.5) shows a difference between the two evaporators. HV2 makes much more oxidized films, and not only on the surface but inside the film. Pressure differences between the evaporators are not an explanation, since both chambers were pumped to the same vacuum. However, HV2 is expected to be dirtier. The visible high peak of oxygen is the oxidized surface

of the film, while the oxide in the tunneling barrier is not clearly seen since it is so thin. Figure 7.6 shows the carbon concentration as function of the film depth. There is no difference in amount of carbon between the two evaporators, but a reduction of 16% in HV2 and 25% in HV1 samples was seen after annealing. Figure 7.7 shows the hydrogen concentration as function of the film depth. There is 15% more hydrogen in non-annealed HV2 sample than in non-annealed HV1 sample. Also a reduction of 29% in HV1 sample and 42% in HV2 sample in hydrogen amount is seen after annealing.

Chapter 8

Electrical characterization of Al–AlO_X–Nb tunnel junctions

Niobium based junctions were fabricated, as discussed in article [A.III.], using the same lithography pattern and two-angle evaporation techniques as the previous samples in articles [A.I.] and [A.II.], except that the dual aluminium deposition and oxidation was used (see Chapter 4.1 where the fabrication process with its difficulties is explained). All niobium-based devices were fabricated in the UHV evaporator.

8.1 Critical temperature of niobium

The critical temperature of niobium was measured from a separately fabricated niobium wire using a dipstick lowered to a liquid helium dewar, while monitoring the sample resistance and the temperature. The wire was 600 nm wide and 50 nm thick, i.e. quite close to the dimensions used in tunnel junction samples. The measurement showed the resistivity to drop to zero at 7.9 K.

The transition temperature of niobium is sensitive to many parameters [55], e.g. the width and thickness of the wire, evaporation speed, and more importantly impurities introduced inside the film in the evaporation process. Thus, the measurements with the wires will not reflect the exact T_C of the tunnel junction samples, even though the wire's dimensions were designed to be a close match to the junction and the metal evaporator, its condition and parameters were all the same.

The critical temperature of niobium used in the actual tunnel junction samples could not be detected by searching for a sudden resistance drop to zero. This is due to the high ≈ 50 kΩ tunneling resistance that dominates over the smaller wire resistance, making it more difficult to detect the T_C of the wire. However, when ac-

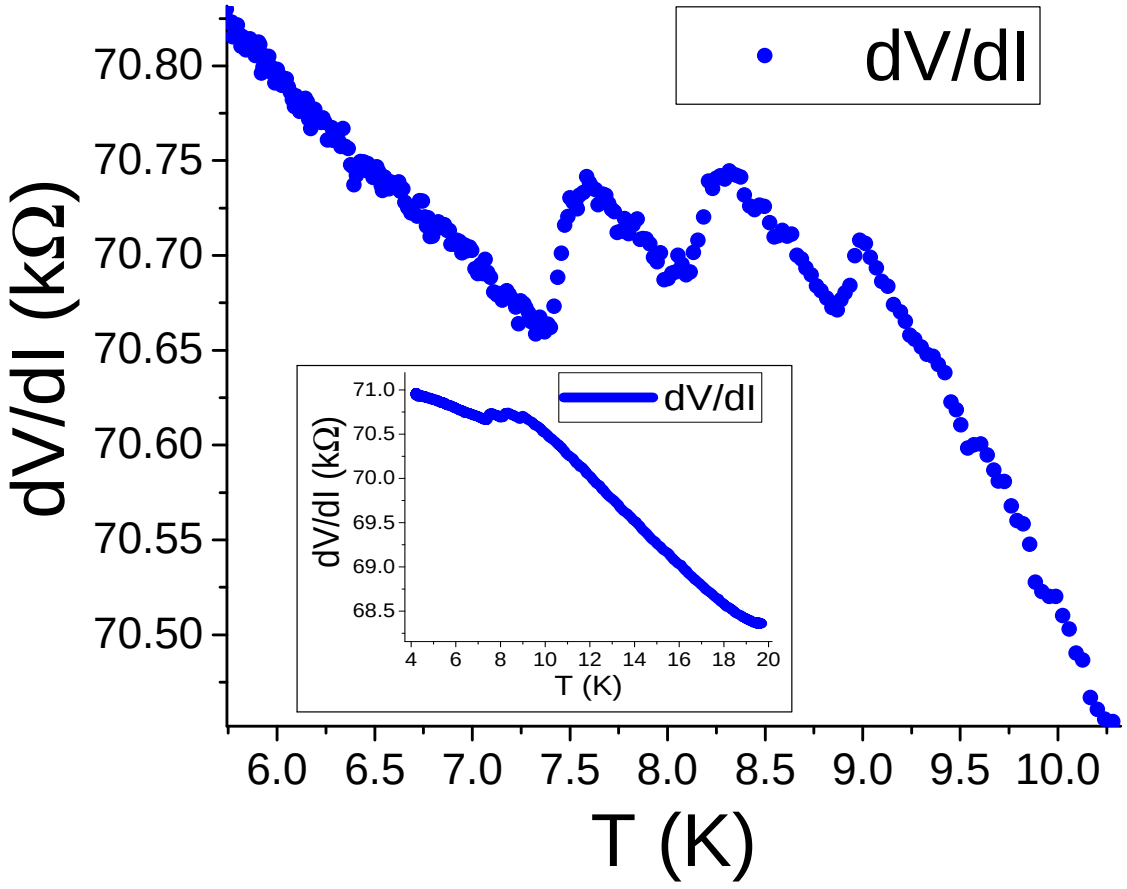

FIGURE 8.1 Measured differential resistance of an Al–AlO_x–Nb junction as a function of temperature. The jumps are due to niobium's transition to normal state in different parts of the wires of different widths.

curately examined, the differential resistance plots were found to have small jumps (see Fig. 8.1) around the expected T_C of Nb. These jumps are interpreted to happen when different parts of the niobium wires turn superconducting at slightly different critical temperatures. This is most likely due to widening of the leads as they connect the junction to the bonding pads. The smallest critical temperature corresponds the narrowest structures in the sample, the leads near the junction. The critical temperature of niobium at the junction is thus 7.5 K.

The transition temperature of the sample studied was also measured with some accuracy by performing a set of current–voltage sweeps at higher temperatures, which showed a disappearance of the niobium superconducting gap also at about 8 K (see Fig. 8.2), giving a rough estimate for the critical temperature that matches quite well with the measured transition temperature of the sample from the resistance vs. temperature data.

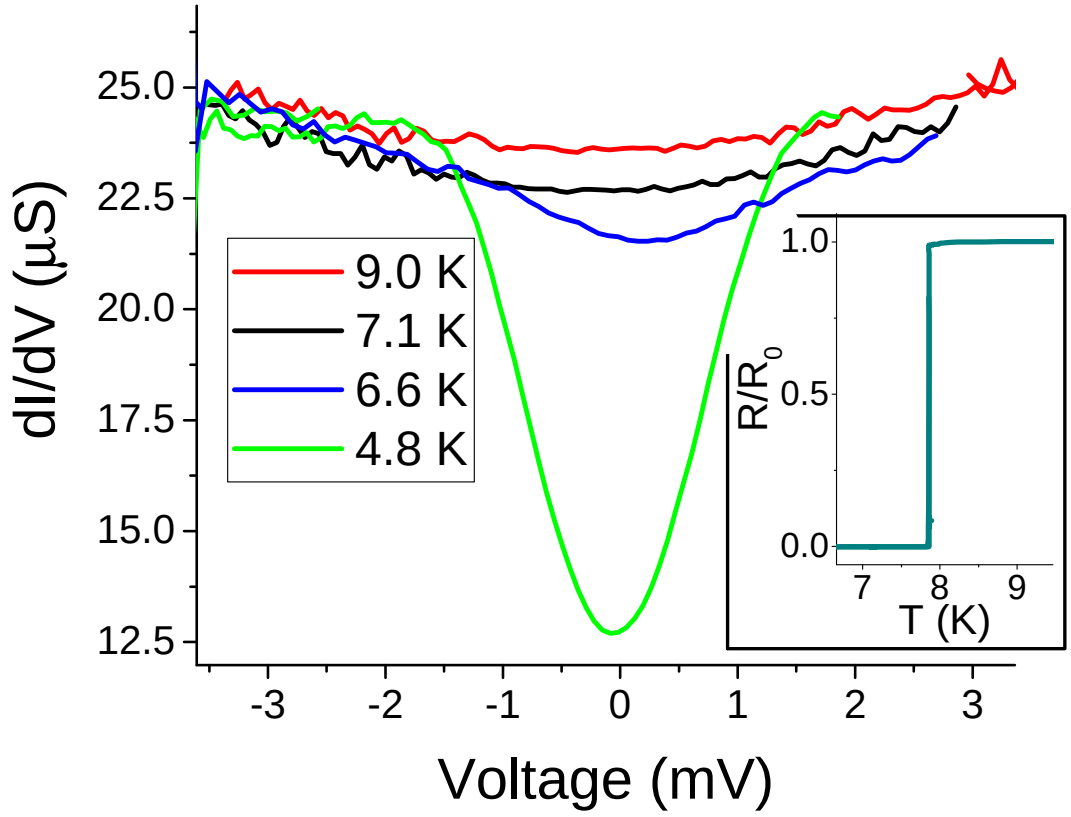

FIGURE 8.2 Measured $dI/dV - V$ data at different temperatures showing an initial buildup of the niobium gap at about 8 K. An inset shows a 600 nm wide and 50 nm thick niobium wire cooled below its transition temperature, showing a complete disappearance of its resistivity at 7.9 K.

8.2 Electrical characterization of Al–AlO_x–Nb samples

Current–voltage measurements were performed for a Al–AlO_x–Nb device at different temperatures, with a summary of the results presented here. Such a device can be either an NIN, or an NIS, or an SIS′ junction depending on the temperature and magnetic field. At temperatures lower than the critical temperature of thin film aluminium (here ≈ 1.3 K), a Al–AlO_x–Nb junction is in the SIS′ state, but at higher temperatures in the NIS state, until above the critical temperature of the niobium (> 7.8 K) the sample is in the NIN state.

An electromagnet made of a superconducting coil was placed at 4.2 K around the sample stage to create a static magnetic field perpendicular to the sample, to suppress the superconductivity in aluminium, and thus allowing the switching of the sample to the NIS state even at the lowest temperatures. The tunneling theory for NIS and SIS′ junctions explained in Chapter 2 is used to analyze the $I - V$ data. The Josephson supercurrent in the SIS′ state was also measured as a function of temperature and magnetic field.

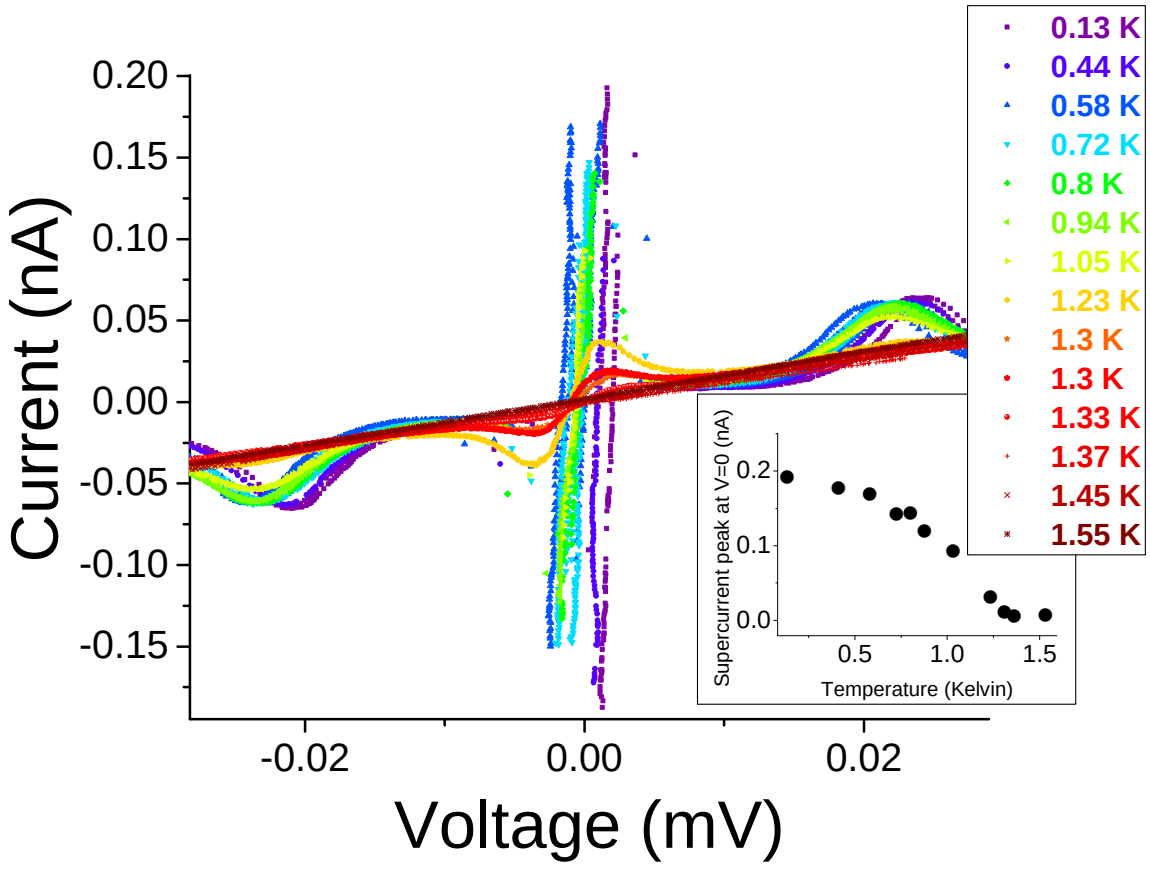

FIGURE 8.3 A $I-V$ measurement close to the supercurrent region in the Al–AlO_x–Nb SIS′ junction as a function of temperature (in the absence of applied magnetic field). At about 1.3 K the supercurrent vanishes. An inset shows the measured zero voltage supercurrent peak value as a function of temperature.

8.2.1 Josephson current

Chapter 2.6 with the SIS tunneling theory considered only quasiparticle tunneling, but in the real data of Al–AlO_x–Nb samples, a supercurrent peak around zero voltage is also seen. The zero voltage supercurrent is due to the DC Josephson effect $I(t) = I_C \sin(\phi(t))$ and is only present when there is a superconductor on both sides of the junction. The supercurrent's maximum value is the critical current I_C, but it also depends on the phase difference $\phi(t)$ between the wavefunction on both sides of the junction.

$I-V$ measurements at different temperatures illustrated in Fig. 8.3 show the reduction of the supercurrent as the temperature increases. In the inset, we plot the maximum value of the supercurrent peak at $V = 0$ as function of temperature. It completely disappears at about 1.3 K, i.e. around the aluminium transition to the

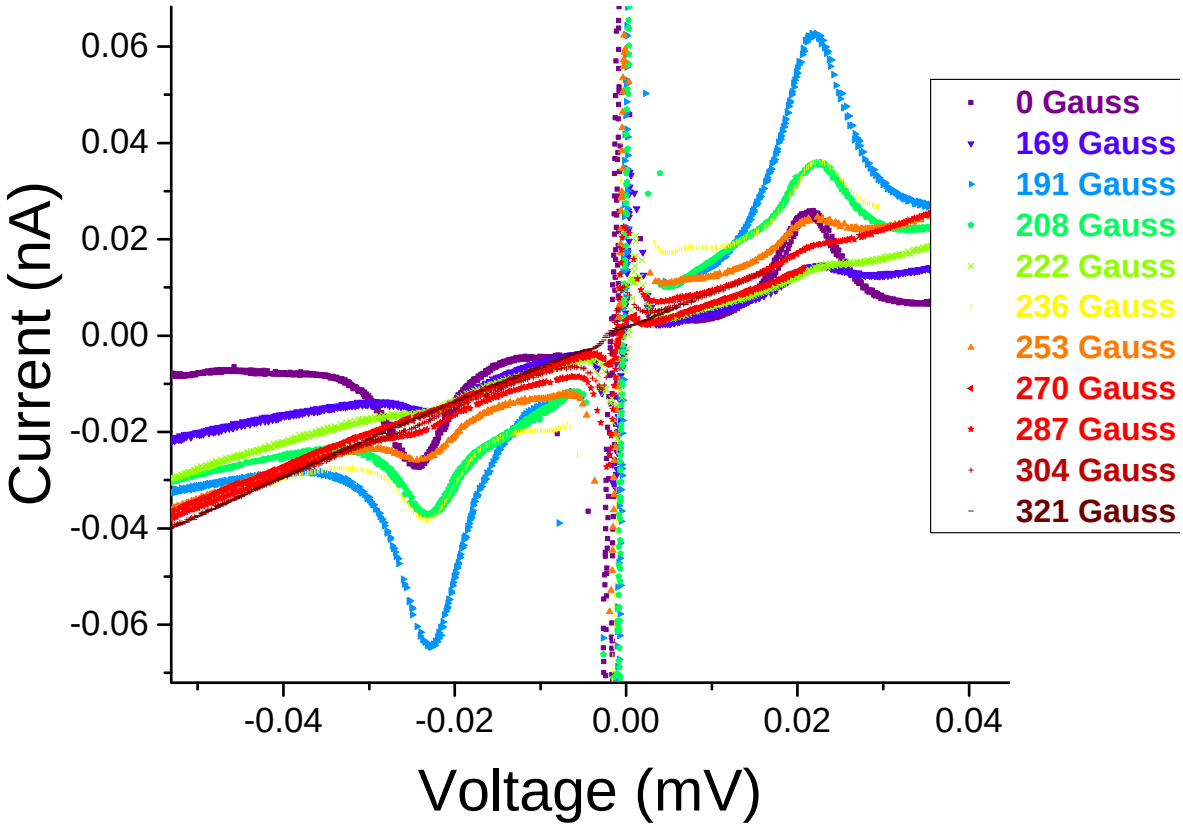

FIGURE 8.4 Supercurrent measured at different magnetic fields up to 321 G at constant temperature of 190 mK.

normal state (an NIS device doesn't show supercurrent).

Similarly the supercurrent dies out as the magnetic field is increased, as the critical magnetic field suppresses the superconductivity of aluminium. This is illustrated in Fig. 8.4, where a similar decrease and flattening of supercurrent is seen as it is in the case with varying temperature.

However, measurements with a magnetic field are a bit tricky since the field can get trapped inside the sample's superconducting films, causing inconsistency in the data and/or a hysteresis. This was found, for example, while sweeping the magnetic field up and down while measuring the zero voltage supercurrent; when returning back to the zero field the original current level didn't always return. In Fig. 8.5 the black data points (left scale) represent the initial measurement when ramping up the magnetic field where the supercurrent peak drops as the field is increased. The red points (right scale) show the same measurement but now reducing the field results in a surprising drop in the current when approaching the zero field. In the data plotted in the right side in Fig. 8.5 a secondary increase in the current can also be seen after it was already close to zero. That could be a Fraunhofer pattern

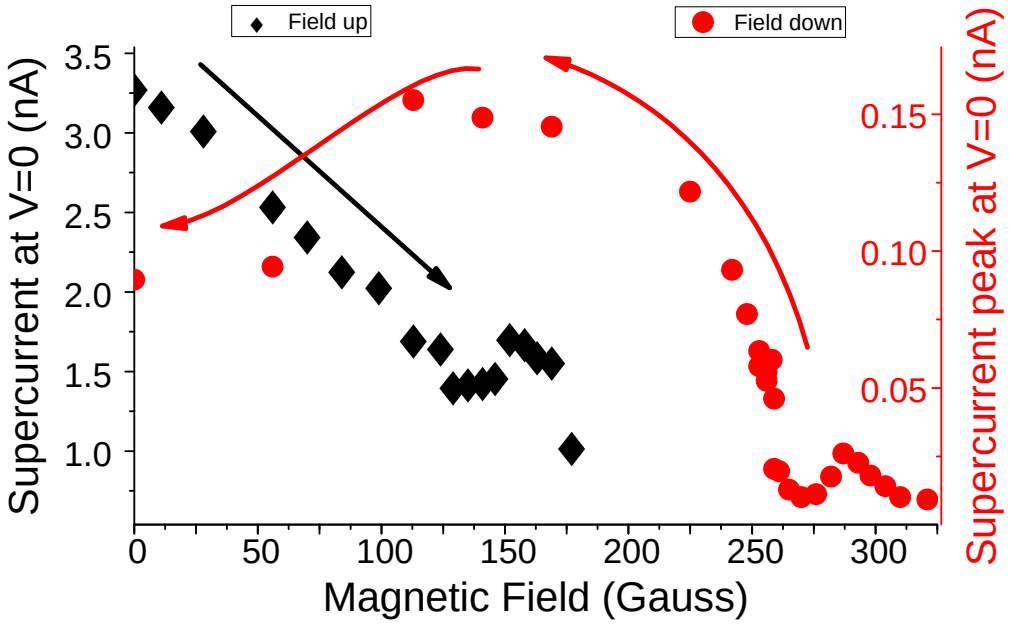

FIGURE 8.5 Supercurrent peak at zero voltage bias as a function of applied magnetic field. The black points represent the first up sweep of a field at 100 mK and the red points when ramping down the field at 190 mK. A hysteresis is apparent.

where the critical current doesn't simply die out once, but will create a decreasing oscillating pattern of minima located at multiples of a magnetic flux quantum $\Phi_0 = \frac{h}{2e}$ [68,69]. The Fraunhofer pattern is more pronounced in a magnetic field parallel to the junction, but is also observable in perpendicular fields, as well. It should be pointed out, however, that the level of the supercurrent varied a lot between different measurements, and thus one should not compare the absolute values of the currents between different measurement sets.

Figure 8.6 plots the $dI/dV - V$ response at different magnetic field values showing the disappearance of both the supercurrent and aluminium's energy gap at $V \sim 0.25$ mV with increasing magnetic field. A notable result here is that the measured aluminium gap for the quasi particle tunneling vanishes first, with the supercurrent still present at magnetic fields of 225 and 281 G. When the field is increased a bit more to 337 G, the supercurrent is also killed off (see the left inset in Fig. 8.6). A possible explanation for this would be that the sample is in SINS' state, where the normal section is only the section of Al not covered by Nb. As this normal metal part is short (< 1 μm) (Fig. 4.7), Cooper pairs can travel through such a SINS' junction, explaining the non-zero Josephson current.

In other words the picture may be the following, an intermediate range magnetic field may not penetrate into all aluminium regions leaving them in superconducting state. Due to the angle evaporation in the fabrication process, there is a niobium film on top of the aluminium everywhere, except within the short distance

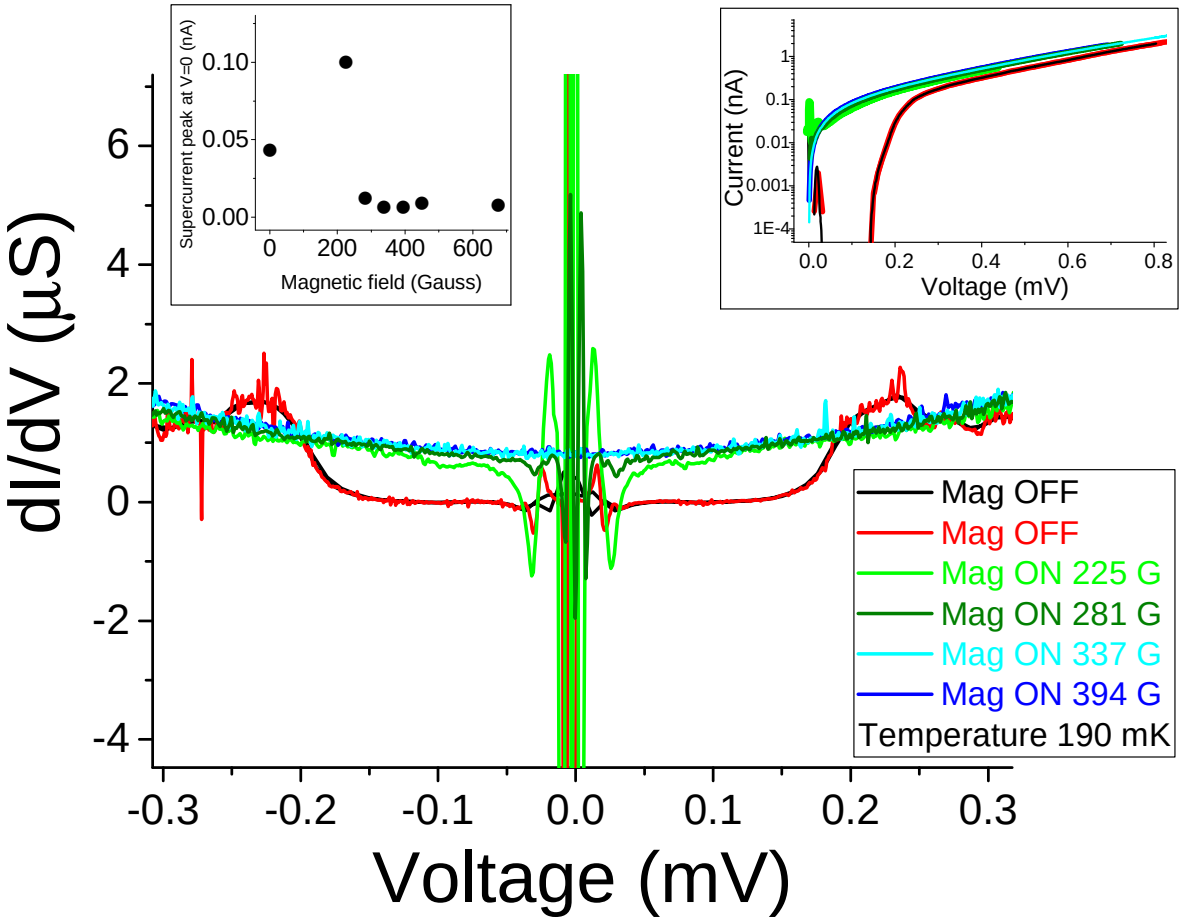

FIGURE 8.6 Differential conductance vs. voltage at different values of external perpendicular magnetic field. The supercurrent still exists at an intermediate field strength where aluminium's gap has died out. An inset shows the measured supercurrent peak at $V = 0$ as a function of applied external magnetic field.

($< 1\,\mu$m) from the tunneling area (see sample geometry figures in Chapter 4, Fig. 4.2, 4.7). The short piece of plain aluminium is easily turned into normal, but the superconducting niobium film shields (at least partially) the magnetic field to protect the superconductivity in the aluminium film beneath it. The aluminium is not completely enclosed by niobium, thus not completely shielded, but instead in the close vicinity of the niobium film will reduce magnetic field density. If the lower aluminium film still shows (some) superconductivity, an SINS' geometry is formed, as schematically illustrated in Fig. 8.7.

8.2.2 Quasiparticle tunneling

In Fig. 8.8, we show how suppression of the superconductivity in aluminium by the applied magnetic field alters the overall current–voltage characteristic, i.e. the

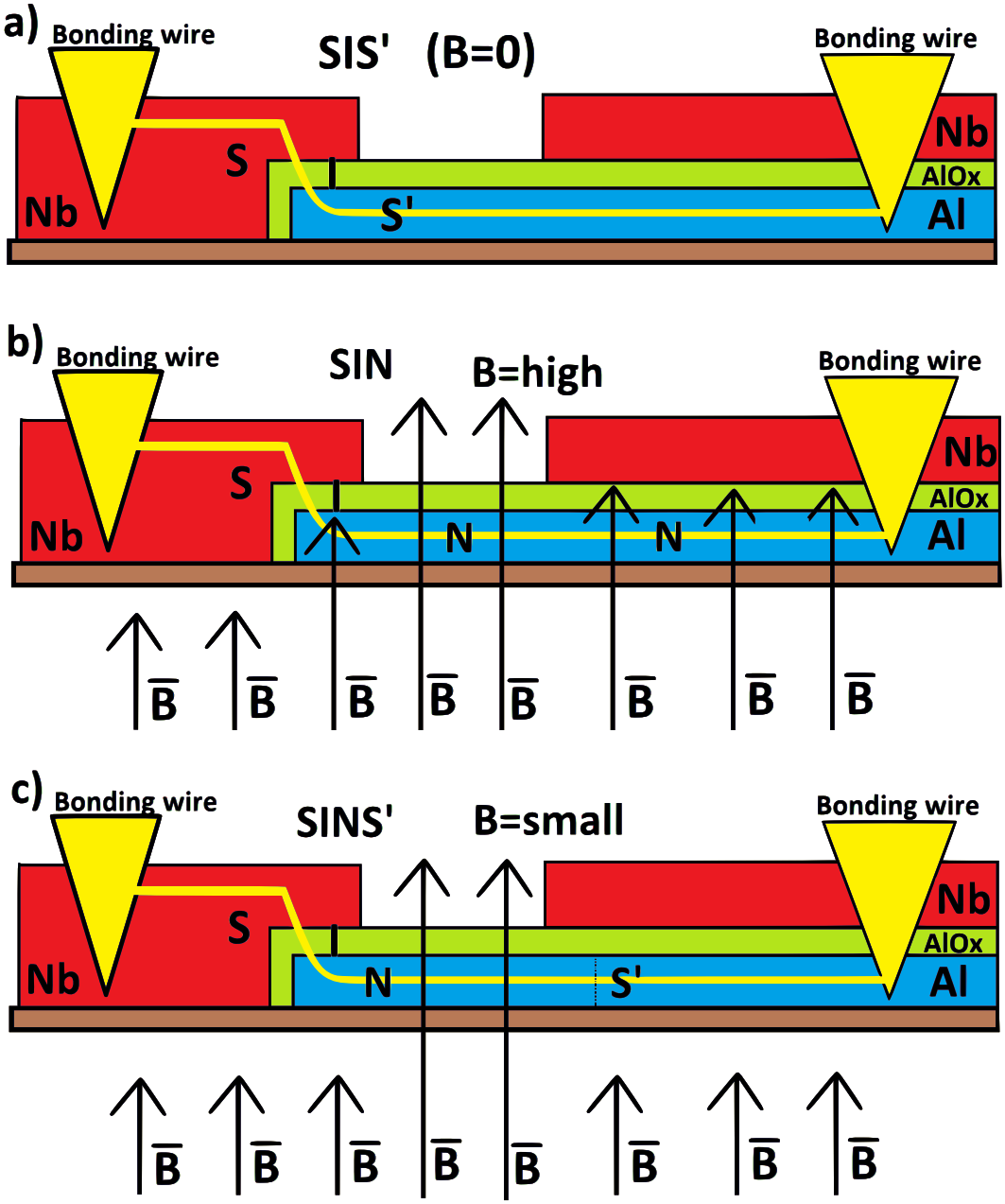

FIGURE 8.7 A Al–AlO_x–Nb tunnel junction in magnetic field. a) Without magnetic field the current flows from niobium to superconducting aluminium through the barrier (SIS'). b) In a relatively high magnetic field the superconductivity in aluminium is completely suppressed and the junction is in NIS state, and the current flows from niobium to normal state aluminium. c) In smaller fields the superconducting niobium may shield the magnetic field penetration through the aluminium film leaving it superconducting. The quasiparticle current is not affected, but the supercurrent may flow through the narrow region of normal state aluminium. As the magnetic field strength is increased, the superconducting areas in aluminium turn normal, killing off the supercurrent. (Note: Despite the 2-dimensional illustration, the B-field is simply re-routed around the superconductor, not stopped at it.)

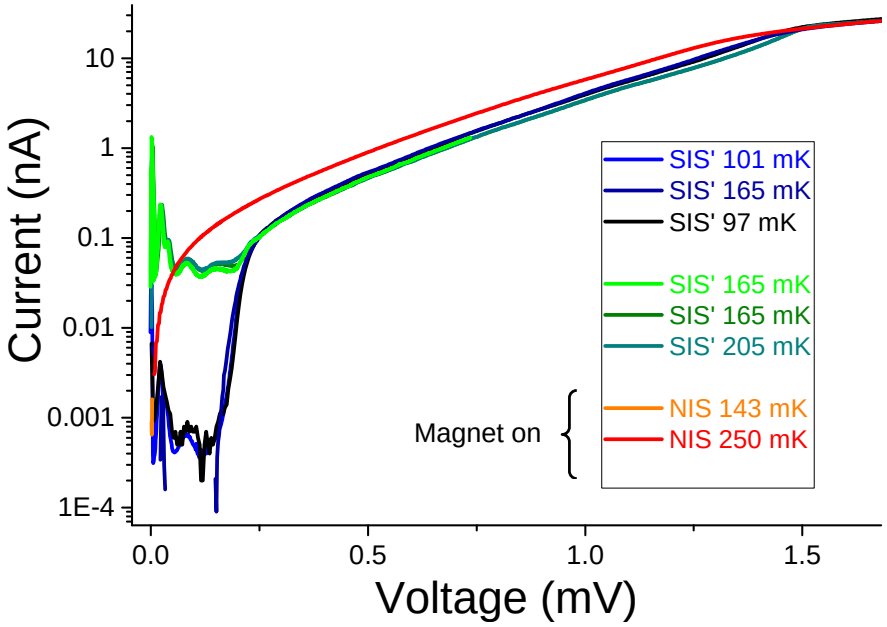

FIGURE 8.8 The difference between the magnetic field on and off, i.e. the sample measured in the NIS and SIS′ states. The SIS′ junction subgap current was found to vary between the measurements, possibly due to flux trapping. In the NIS state a field of $B = 1000$ G was applied.

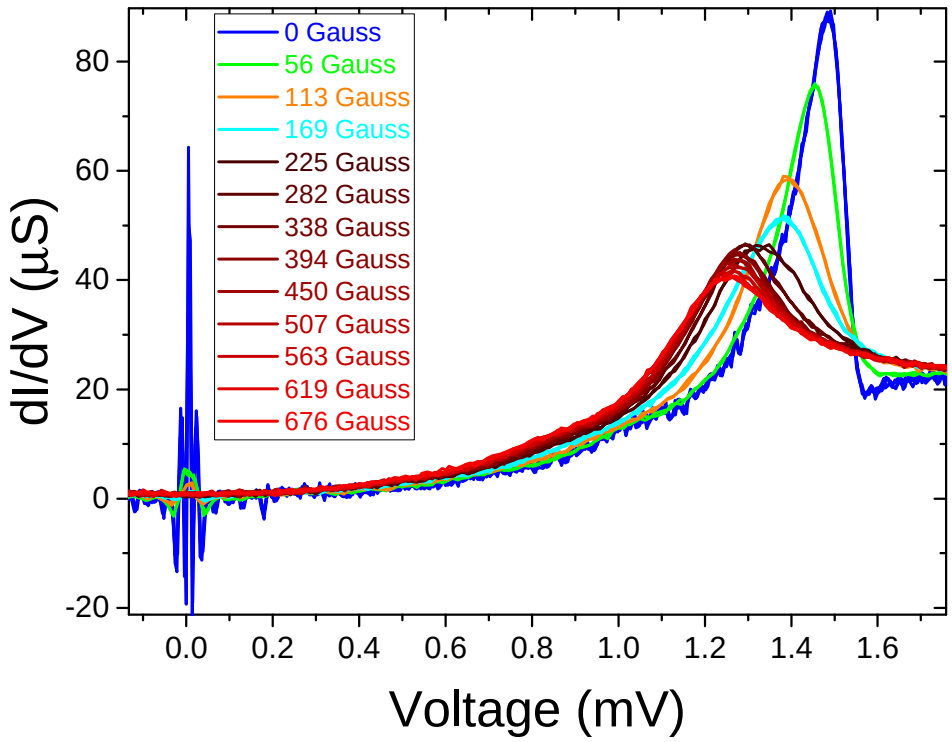

FIGURE 8.9 Measured differential conductance dI/dV at different magnetic fields at a temperature of 140 mK. Above the critical field of aluminium ($B \sim 200$ G) there is no difference between the curves with increasing B, so the effect of magnetic field on niobium is insignificant in this field range.

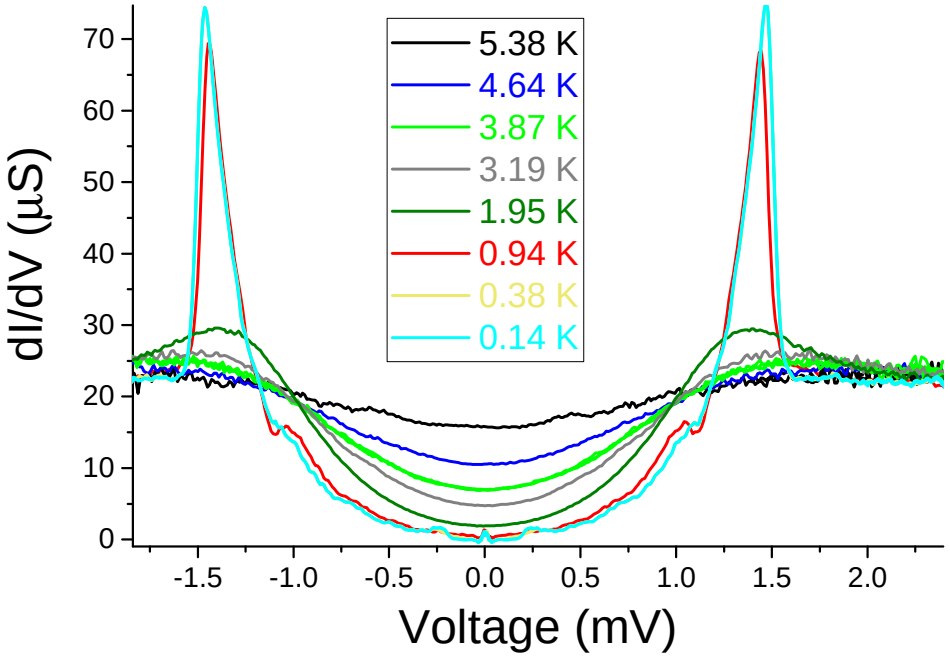

FIGURE 8.10 Measured differential conductance dI/dV without applied magnetic field. Temperatures lower than 1 K exhibit a wider gap due to the aluminium also being superconducting, i.e. the junction is SIS′. When $T \geq 1.9$ K the sample is an NIS device. Supercurrent contribution has been removed.

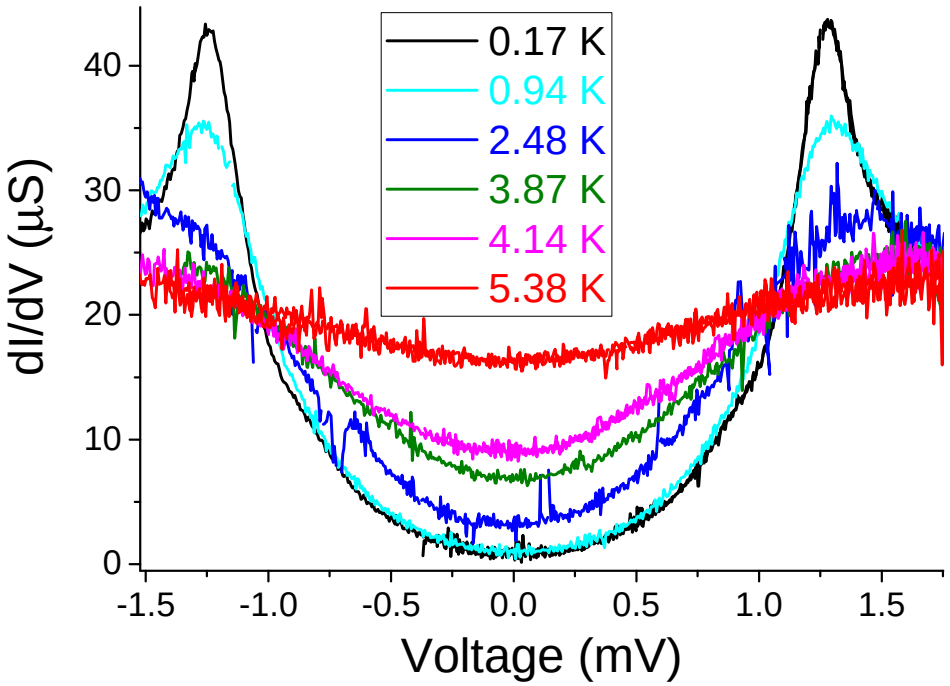

FIGURE 8.11 Differential conductance dI/dV of the junction in NIS state where the superconductivity of aluminium is suppressed with a magnetic field of $B = 450$ G at all temperatures.

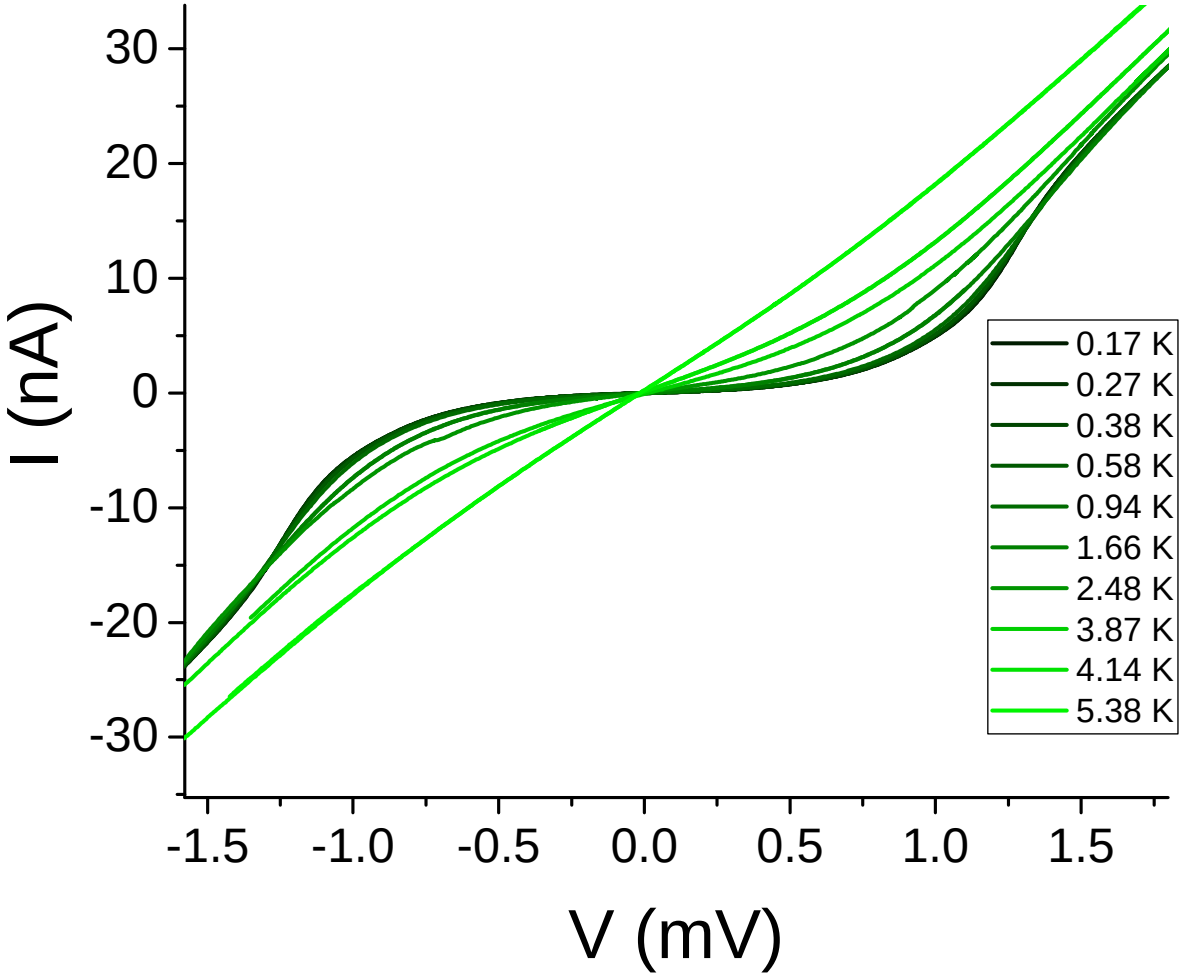

FIGURE 8.12 The $I - V$ characteristics of the junction in NIS state where the superconductivity of aluminium is suppressed with a magnetic field of $B = 450$ G at all temperatures.

difference between the SIS' and NIS states of otherwise identical samples measured at approximately the same temperature.

At zero B-field, in the SIS' state, the measured gap feature (peak in dI/dV) is given by the sum of the superconducting gaps of both materials $\Delta_{Nb} + \Delta_{Al}$, [see Chapter 2.6]. When the field is increased to ~ 200 G, the niobium gap, Δ_{Nb}, stays intact ≈ 1.3 meV but the transition to NIS state shows the disappearance of the aluminium gap contribution ($\Delta_{Al} = 0.2$ meV) together with the vanishing of the supercurrent at zero voltage. The base level of the subgap current at zero field was found to vary between otherwise identical measurements, likely due to some magnetic field trapped inside the sample (blue and green plots on the graph that were both measured with the magnet off).

The singularity matching peak predicted by the theory at $eV = \Delta_{Nb} - \Delta_{Al}$

couldn't be detected, most likely because of the large difference between the gap values, i.e. $\Delta_{Nb} - \Delta_{Al} \approx \Delta_{Nb}$. At a voltage so close to the sum gap feature the conductivity was already quite high due to the larger Dynes smearing in niobium's density of states [55]. The larger Dynes parameter of niobium also explains why the aluminium gap in the SIS' measurements at $eV < \Delta_{Al} \approx 0.2$ meV is sharper, as aluminium has orders of magnitude lower Dynes-parameter, and thus the subgap current is significantly smaller.

The external magnetic field can quite easily suppress superconductivity in aluminium, but these field strengths are not even close to what would be needed to suppress the superconductivity in niobium. This is shown in Fig. 8.9 where the differential conductance is measured around niobium's gap. Above the field strength where aluminium turns into normal state, there is no difference in the dI/dV curves.

Figure 8.10 shows the differential conductance of the junction at different temperatures, where the transition from SIS' to NIS happens at temperatures higher than 1 K as the aluminum changes from superconducting to normal state.

In Figs. 8.11 and 8.12 we plot the results where a magnetic field higher than the critical field of the aluminium ($B = 450$ G) was used to keep the device in the NIS state even at the lowest temperatures. The data shows the niobium gap only. Here, it is also possible to see how the plots show saturation towards the lowest temperatures: there is not much difference in the curves between 0.93 K and 0.16 K, except that the gap edge is a little bit sharper seen as a higher differential conductance peak. In comparison to Nb–Al–AlO_x–Cu NIS samples in Ref. [70] there is no extra feature due to Al in the dI/dV curves, because no Al layer is required on the Nb side of the barrier, in contrast to the work in [70].

The value $\Delta_{Nb} \sim 1.27$ meV obtained from Fig. 8.11 is fairy high, almost at the level of highest values $\Delta_{Nb} \sim 1.4$ meV for submicron junctions in the literature [71–73]

8.2.3 Theoretical fits for the $I - V$ and $V - T$ data

Theoretical fits based on the single-particle tunneling model were also made for the SIS' and NIS $I - V$ measurements. They are illustrated in Figs. 8.13 and 8.14. The calulated curves don't match so well with the experimental data, in particular at bias voltages around ~ 1 mV where the theory is much below the data especially at low temperatures. However, the aluminium gap feature ($V \lesssim 0.25$ mV) in the SIS' data is fitted quite well with reasonable parameters, e.g. the simulation temperatures correspond the measured sample temperatures (see Fig. 8.13) and Dynes from [70,71].

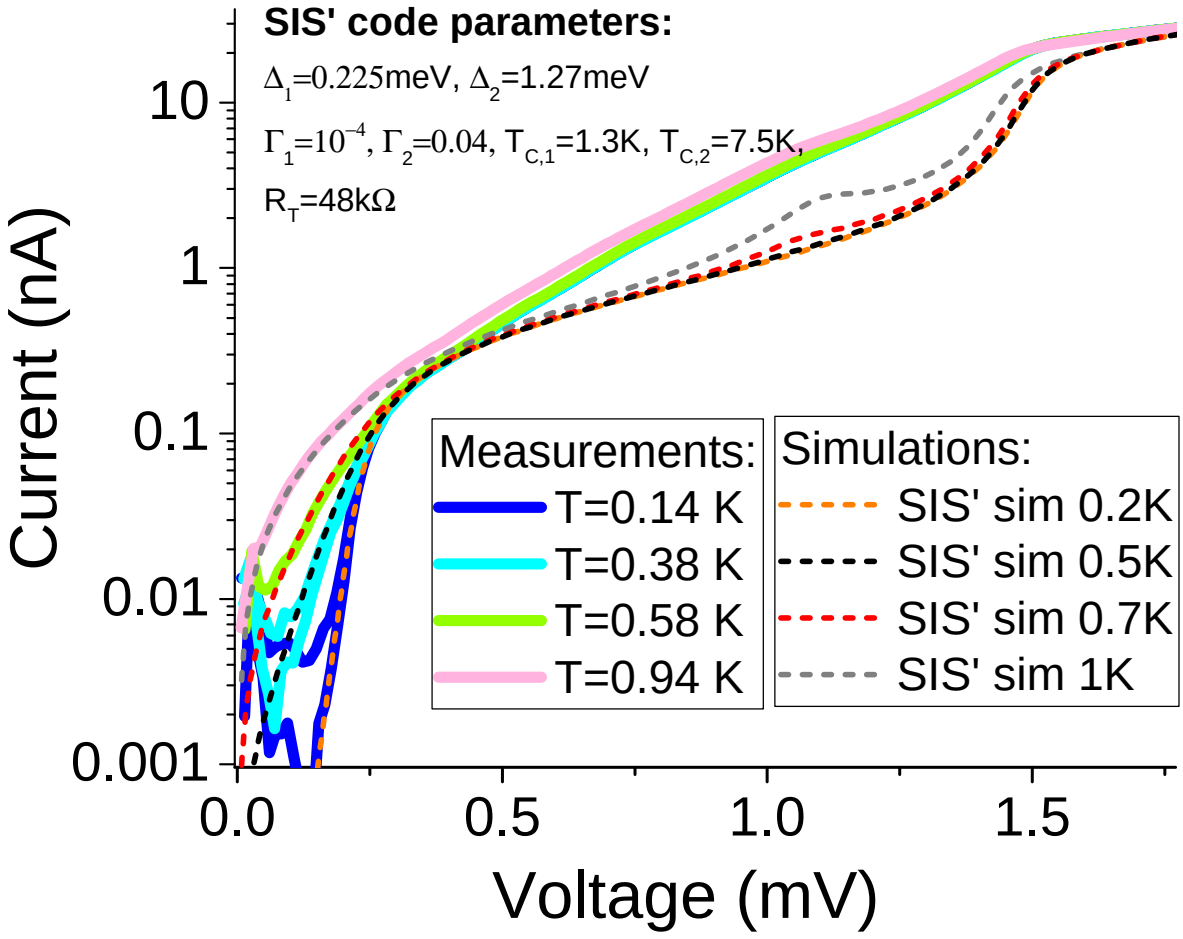

FIGURE 8.13 $I-V$ characteristics of measured single junction SIS' samples, together with simple theoretical simulations at different temperatures. Since the temperature is much lower than the critical temperature of niobium, a difference is seen only at lowest voltages where the aluminium's gap is visible and thus the temperature difference is relatively large compared to aluminium's critical temperature. The theoretical model doesn't fit here accurately, except into the aluminium feature at lowest voltages.

The same mismatch between the theory and measurements was also found in the NIS data (Fig. 8.14), i.e. the "dip" around 1 mV predicted by the theoretical model is missing in the experimental data. One can't avoid noticing that the shape of the experimental curve looks like the sample was much hotter than the measured temperature (see the simulated theoretical curves in Fig. 2.6 in Chapter 2.5), so here we gave a try to have the closest fit calculated at much higher temperatures than what the sample stage thermometer measured. This seemed to work for the highest temperatures leading to a good match between the theory and measurement, but at such high temperatures the curve was already almost linear. At all lower temperatures, the $I-V$ model doesn't lead to perfect fitting even when we used the

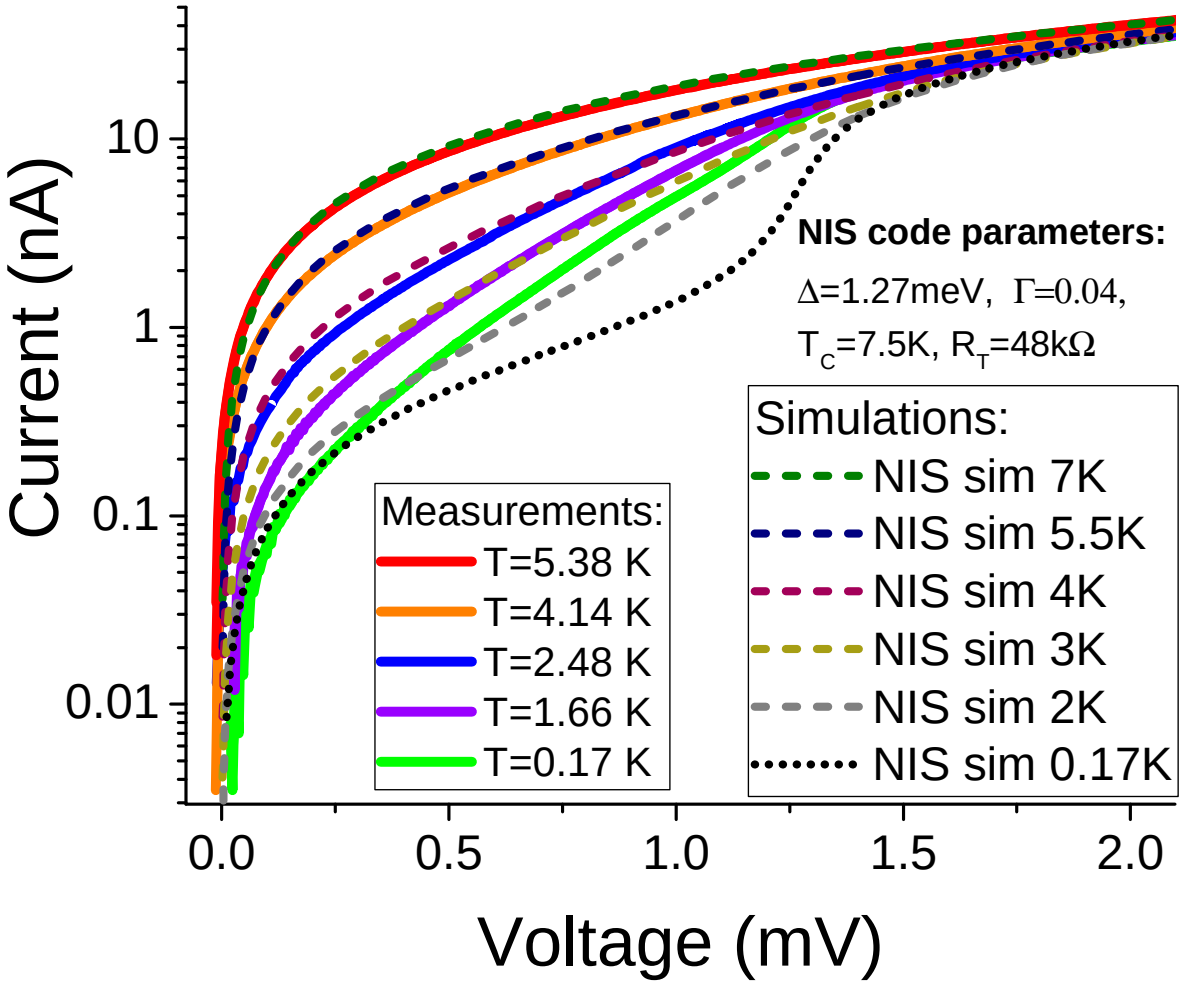

FIGURE 8.14 Measured $I - V$ characteristics of a single NIS junction, together with simple theoretical simulations at different temperatures. The theoretical curves were calculated using higher temperatures in trying to make the data fit.

higher temperature as a fitting parameter. However, we point out that in this simple model the bath temperature and the electron temperature are equal, so self heating as a function of bias voltage is missing. Even though the sample can heat up, the closest fits were calculated at surprisingly high temperatures that can't be easily justified, especially since the aluminium gap feature was fitted well at reasonable temperatures in the SIS' data. In the SIS' case, on the other hand, higher temperatures can't be used at all, since they would kill off the highly temperature dependent aluminium gap. It looks like heating of the sample can't explain this phenomenon.

The fitting issue between the measurement and the theory was only present in these Al–AlO_x–Nb junctions where the niobium was deposited last. The Nb junctions studied in Ref. [55], with the niobium evaporated first, didn't have any issues in fitting the data with the Dynes model. Since we have a clear evidence that the

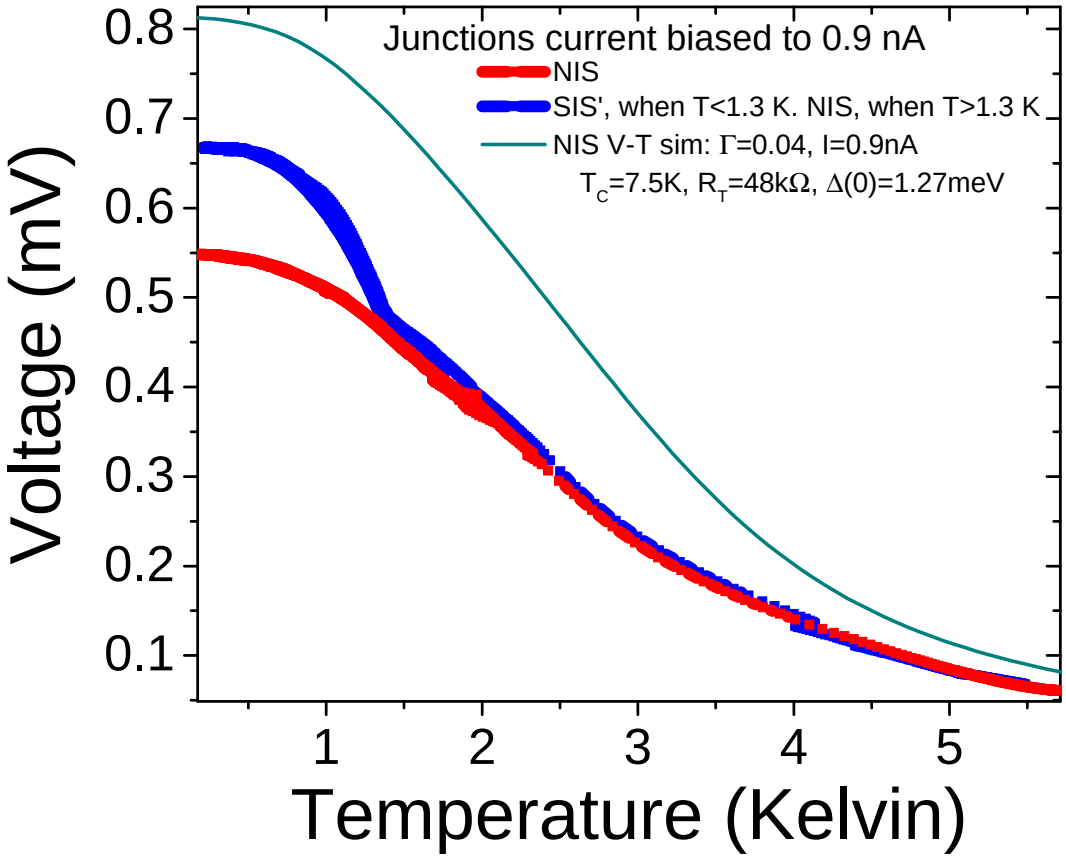

FIGURE 8.15 Voltage vs. temperature dependence of both NIS (B-field on) and SIS' junctions when constant current biased to ~ 0.9 nA. $V - T$ theoretical simulation is included in the graph for the NIS data.

finally evaporated niobium makes damage to the aluminium oxide, and even penetrates through it (thus the two consecutive Al evaporations and subsequent oxidations), we can make assumption that the finally evaporated niobium may change some characteristics of the barrier when penetrating into it, and thus creating a more complex tunneling scheme that the Dynes broadening can't accurately model. More understanding of these non-idealities is required.

In another measurement the sample was biased with constant current just below the gap value at ~ 0.9 nA, and the voltage across the junction was measured as the cryostat temperature was swept between 100 mK and 6.5 K, both in the SIS' and in the NIS state. This type of measurement is typically used in NIS thermometry, i.e. converting a voltage into temperature. We see that the device works well as thermometer between 0.5 K up to the T_C of Nb with only slightly smaller responsibility than in [70]. The data is shown in Fig. 8.15. The SIS' sample obviously changes to the NIS state at temperatures higher than aluminium's critical temperature leading to an identical result above 1.3 K. The low temperature saturation below 0.5 K can

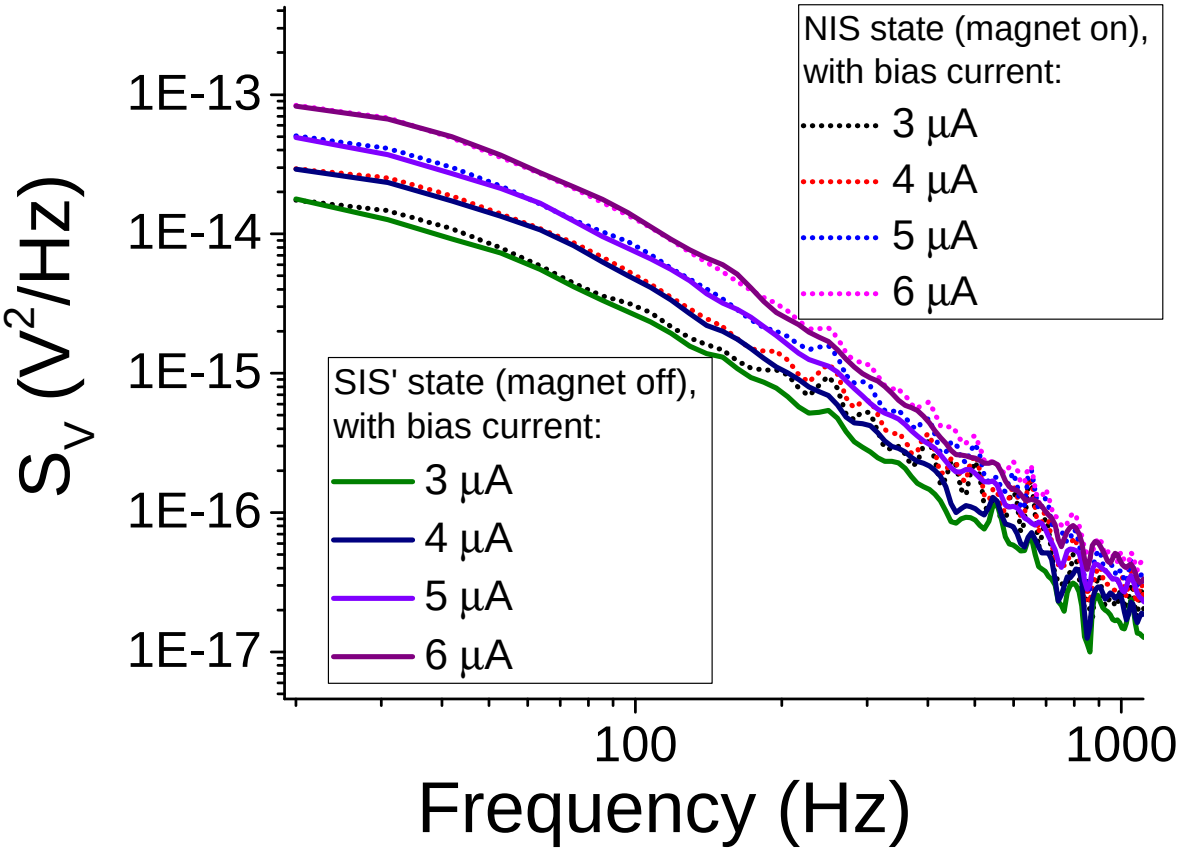

FIGURE 8.16 Measured $1/f$ noise from an Al–AlO_x–Nb tunnel junction at different bias currents with and without magnetic field to suppress superconductivity in aluminium. No difference in noise between the NIS and SIS′ states is seen. The temperature was 160 mK.

be explained by the Dynes broadening of the Nb, with a value in agreement with Ref. [70]. However, it is clear that the theory does not work, since it can be seen already from the $I-V$ plots in Fig. 8.14 that at $I \sim 0.9$ nA the theory and experimental data deviates a lot.

NIS devices are known to work as coolers as well [14]. The observed value of Γ would still allow for some cooling if the junction resistance were lower [33]. However, the observed excess current prevents cooling.

8.3 1/f noise in the NIS and the SIS′ states

An important test was to check if the $1/f$ noise changes between superconducting and normal state samples. Magnetic field was again used to switch between NIS and SIS′ states below aluminium's critical temperature in Al–AlO_x–Nb junctions. In Fig. 8.16 we show the measured voltage noise of the sample when changing the bias

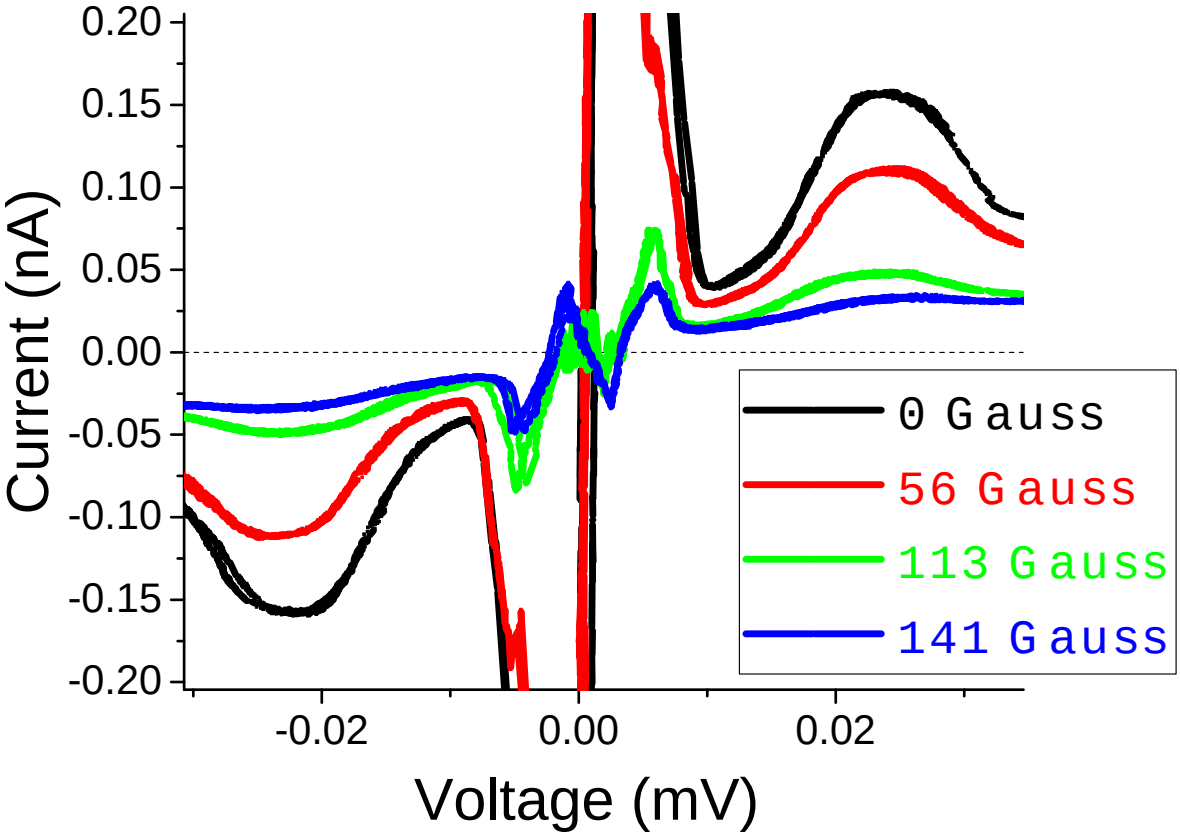

FIGURE 8.17 Negative absolute resistance clearly seen when changing the magnetic field value close to the critical field. Temperature was 800 mK.

voltage and switching the sample between NIS and SIS' states at 160 mK. The results show the expected increase in the noise level as the current is increased, but there is no measurable difference between the magnetic field on or off. This gives more evidence that the $1/f$ noise origins from the barrier, and the state of the leads do not contribute much, if at all. This is in contrast to some theories of $1/f$ noise [74].

8.4 Negative absolute resistance

Some anomalies were also discovered while doing the measurements. One was the presence of negative absolute resistance when carefully studying the supercurrent close to the critical field or critical temperature of aluminium. Tunnel junctions are highly nonlinear and shows negative differential resistance in many occasions but the absolute negative resistance should not be possible in a passive system due to Joule's law: $P = I^2R$, as a passive device consumes power, i.e. $P > 0$ [75].

Figure 8.17 shows $I - V$ measurements at 800 mK at different magnetic field values and clearly shows such a negative resistance, i.e. when the voltage increases

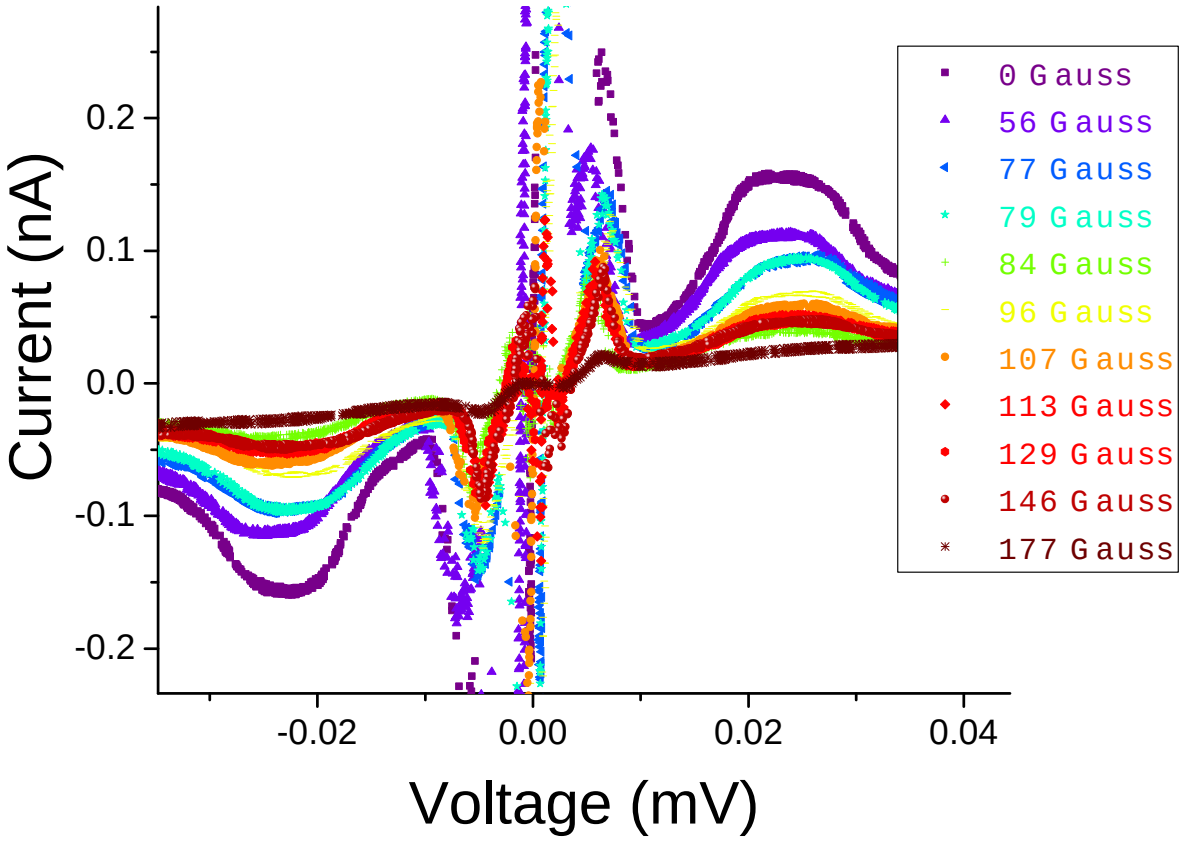

FIGURE 8.18 Supercurrent measured at different magnetic fields at constant temperature of 720 mK. Negative absolute resistance is seen as the field strength approaches the critical field.

from zero to positive side the current immediately flows in the opposite direction. The phenomenon was visible close to the critical field, but was reproducible.

Figure 8.18 shows another measurement set with lots of data at different magnetic fields where the narrow window of field strength where the absolute negative resistance exists can be seen, just before all the supercurrent peaks vanish and aluminium turns normal. Notice here that the bath temperature was also quite high so low field strengths were enough to turn aluminium normal.

The negative absolute resistance was also detected when measuring the device at different temperatures very close to the critical temperature without any external magnetic field, but with possible trapped flux inside superconducting electrodes, since prior to the measurements the magnetic field was applied over the device. The data is visible in Fig. 8.19, where the negative resistance signal is much weaker than what it was when sweeping the magnetic field (cf. Figs. 8.17 and 8.18).

However, it is important to point out that the data was not reproducible from cooldown to cooldown. Even though all the same temperature and magnetic field

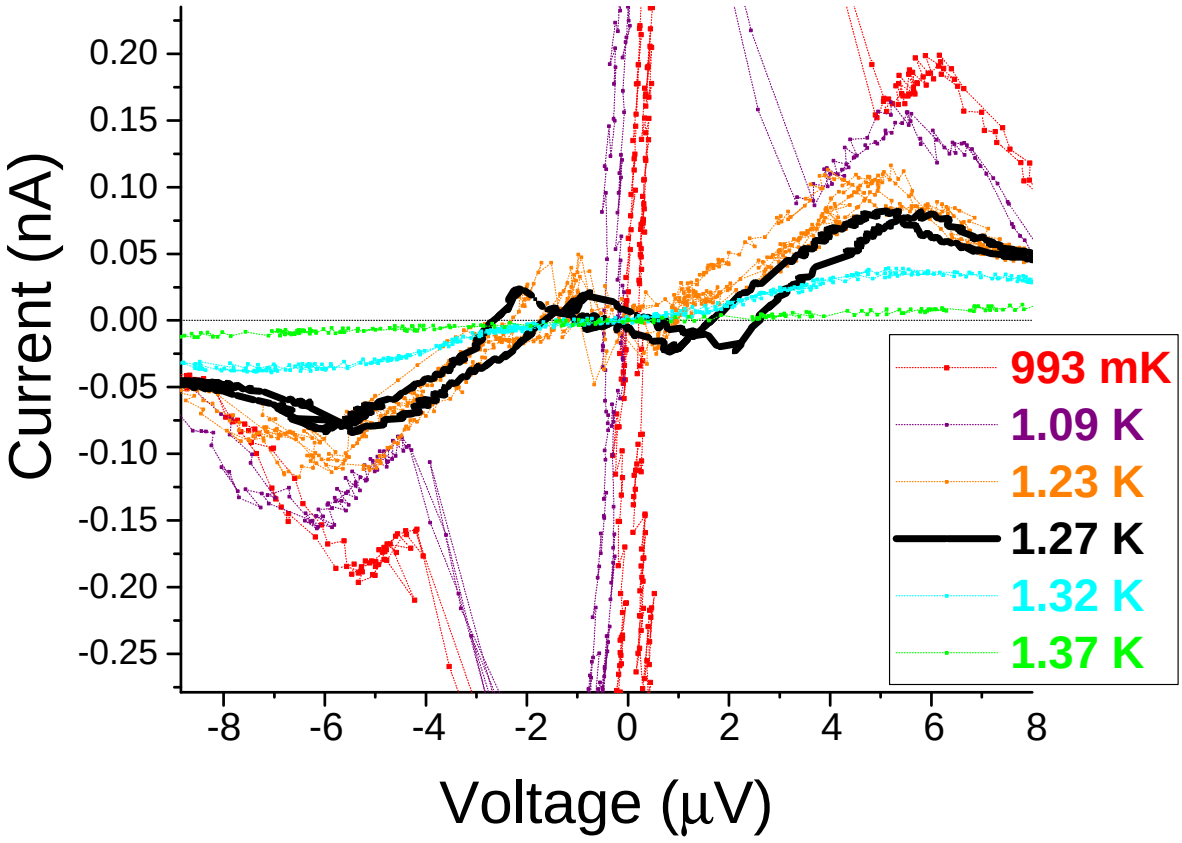

FIGURE 8.19 Supercurrent measured at different temperatures. There was no external magnetic field present, but instead possibly a trapped flux inside the superconductor, since before the measurement the field was ramped up and down. Negative absolute resistance is visible close to the aluminium's T_C, however, the signal is not as clear as in the measurement with the external magnetic field close to the critical field (Figs. 8.17 and 8.18).

values, as in Fig. 8.18, were tested multiple times, results sometimes showed a conventional supercurrent feature, as seen for example in Fig. 8.4. When comparing the Figs. 8.18 and 8.4, there is also some obvious differences in the shape of the adjacent peaks around $V = 0$, as in the former case there is a huge extra peak just next to the zero voltage peak, which is missing in the latter data.

The real nature of the phenomenon remains a mystery, at this point, but trapping of magnetic field is probably important.

Chapter 9

Conclusions

Al–AlO_x–Al and Al–AlO_x–Al:Mn NIN and NIS tunnel junctions were fabricated and successfully stabilized by thermal annealing. Stabilization depended on the evaporator and there was lots of deviation between different samples, but on the average the evidence of stabilization after annealing was clear. This is a clear benefit for a wide range of applications since having a device with stable characteristics with minimal aging is desirable.

Annealing mostly increased the junction quality by lowering the characteristic $1/f$ noise, however it was not the case for all junctions since the type of sample and used evaporator played a role in the noise levels, in both before and after annealing. The reduction of $1/f$ noise after annealing was found in all Al–AlO_x–Al samples, regardless of the used evaporator.

Al–AlO_x–Al:Mn junctions fabricated in two different evaporators behaved more complexly. Al:Mn samples fabricated in the "dirtier" HV2 evaporator suffered an increase in noise. Similar Al:Mn samples fabricated in cleaner conditions in HV1 evaporator showed decrease in their $1/f$ noise levels after annealing. The reason is not necessarily the evaporator's poor vacuum chamber quality, but the deposited film. Material analysis showed how the evaporated manganese concentration varied between different evaporators, being quite uneven in the HV2 evaporator since the lack of electron-beam sweeping while evaporating metal. Annealing also changed the manganese concentration profile.

Noise reduction is a desired result, since the intrinsic noise is limiting the performance of most applications. Especially in the case of superconducting qubits, low-frequency $1/f$ noise of the junction resistance (critical current) leads to dephasing of the qubit [76,77].

$1/f$ noise was studied at different temperatures and found to show almost an identical temperature response in both Al and Al:Mn samples, except at the lowest temperatures. The $1/f$ noise has an approximately linear temperature dependence

between 10 K and 200 K, but then showing a strong increase in temperature dependence at temperatures approaching the room temperature.

Current–voltage characteristics were measured from Al–AlO_x–Al:Mn tunnel junctions at cryogenic temperatures before and after annealing. There was no difference in the subgap current or the energy gap, the results showed that only the tunneling resistance increased. Based on theoretical models the reduced Dynes parameter was always $\Gamma \sim 1 \cdot 10^{-4}$.

Good quality niobium-based junctions were fabricated with the niobium's critical temperature measured to be 7.5 K in the narrowest structures. Al–AlO_x–Nb junctions were measured at temperatures between $\sim$ 100 mK and $\sim$ 9 K. Such junctions are SIS' type at low temperatures, but a perpendicular magnetic field was used to suppress superconductivity in aluminium leading to an NIS junction.

$I - V$ characteristics were measured and analyzed based on theoretical model of tunneling in both NIS and SIS' states, revealing a clear mismatch between the experimental data and theory in the sub-gap current. The measured data showed excess current, which could be interpreted as additional quasiparticle states in the gap of Nb, that cannot be described by the Dynes model. We think the non-ideality is due to some Nb/AlO_x interface issues where the finally evaporated hot niobium is damaging the barrier, since the Nb-based samples where the niobium is evaporated first obeys the Dynes model [55]. However, the advantages in this process are that there is no proximity effect issue of the extra Al layer and the fabrication method is simple and straightforward to utilize in many designs. The excess sub-gap current prevents NIS cooler applications, but the junction still shows a good $V - T$ response that can be used for thermometry. This geometry requires more study - possibly a thin protection layer between the AlO_x and Nb could protect the barrier against the damage.

$1/f$ noise was also measured from the Al–AlO_x–Nb samples. The 1/f noise was found to be independent on sample's superconducting state, i.e. its SIS' or NIS state, that was switched using an external magnetic field.

Results showed clearly the two different gaps from both superconductors (Al and Nb), as the theory predicts, and the vanishing of aluminium's gap when above its critical temperature or critical magnetic field. The measured Nb gap $\Delta \sim 1.3$ meV is consistent with the measured transition temperature.

Supercurrent at zero voltage bias was measured at different temperatures and magnetic fields. The height of the supercurrent peak depended on both the temperature and magnetic field, as expected based on Ambegaokar-Baratoff's theory [78] and as the external field penetrates through the superconductor [79]. Some more complex results were also found; when sweeping the magnetic field up and then

back down the supercurrent didn't always return back to the original maximum value (at zero field), but remained at a lower level. This can be explained to arise due to field trapping.

Negative absolute resistance was present in some data when the external magnetic field was close to the critical field value or the device was close to the critical temperature after being under the influence of an external magnetic field, thus most likely also having trapped field.

Bibliography

[1] TINKHAM, M., *Introduction to Superconductivity* (McGraw-Hill, New York, USA, 1996), 2nd ed.

[2] RJABININ, J. AND SHUBNIKOW, L., *Magnetic properties and critical currents of superconducting alloys*. Nature **135** (1935) 581–582. URL https://dx.doi.org/10.1038%2F135581a0.

[3] TINKHAM, M., *Effect of fluxoid quantization on transitions of superconducting films*. Physical Review **129** (1963) 2413–2422. URL http://link.aps.org/doi/10.1103/PhysRev.129.2413.

[4] DEW-HUGHES, D., *Flux pinning mechanisms in type ii superconductors*. Philosophical Magazine **30** (1974) 293–305. URL http://www.tandfonline.com/doi/abs/10.1080/14786439808206556#.

[5] BARDEEN, J., COOPER, L. N., AND SCHRIEFFER, J. R., *Theory of superconductivity*. Physical Review **108** (1957) 1175–1204. URL http://link.aps.org/doi/10.1103/PhysRev.108.1175.

[6] DROZDOV, A., EREMETS, M., TROYAN, I., KSENOFONTOV, V., AND SHYLIN, S., *Conventional superconductivity at 203 kelvin at high pressures in the sulfur hydride system*. Nature **525** (2015) 73–76. URL http://dx.doi.org/10.1038/nature14964.

[7] GRIFFITHS, D., *Introduction to Quantum Mechanics*, Pearson international edition (Pearson Prentice Hall, 2005).

[8] RICH, J., *Fundamentals in Nuclear Physics* (2005). URL http://adsabs.harvard.edu/abs/2005fnp..book.....B.

[9] MISHRA, U. AND SINGH, J., *Semiconductor Device Physics and Design* (Springer, 2008).

[10] SEABAUGH, A., *The tunneling transistor* URL http://spectrum.ieee.org/semiconductors/devices/the-tunneling-transistor.

[11] AGARWAL, A. AND LANG, J., *Foundations of Analog and Digital Electronic Circuits*, Morgan Kaufmann series in computer architecture and design (Elsevier : Morgan Kaufman Publishers, 2005).

[12] JOSEPHSON, B., *Possible new effects in superconductive tunnelling*. Physics Letters **1** (1962) 251 – 253. URL http://www.sciencedirect.com/science/article/pii/0031916362913690.

[13] KOCHSIEK, M. AND GLÄSER, M., *Handbook of Metrology* (John Wiley & Sons, 2010).

[14] GIAZOTTO, F., HEIKKILÄ, T. T., LUUKANEN, A., SAVIN, A. M., AND PEKOLA, J. P., *Opportunities for mesoscopics in thermometry and refrigeration: Physics and applications*. Reviews of Modern Physics **78** (2006) 217–274. URL http://link.aps.org/doi/10.1103/RevModPhys.78.217.

[15] PEKOLA, J. P., HIRVI, K. P., KAUPPINEN, J. P., AND PAALANEN, M. A., *Thermometry by arrays of tunnel junctions*. Physical Review Letters **73** (1994) 2903–2906. URL http://link.aps.org/doi/10.1103/PhysRevLett.73.2903.

[16] AVERIN, D. V. AND LIKHAREV, K. K., *Single-Electron Tunneling and Mesoscopic Devices: Proceedings of the 4th International Conference SQUID '91 (Sessions on SET and Mesoscopic Devices), Berlin, Fed. Rep. of Germany, June 18–21, 1991* (Springer Berlin Heidelberg, Berlin, Heidelberg, 1992), pp. 3–12. URL http://dx.doi.org/10.1007/978-3-642-77274-0_1.

[17] GALLOP, J. AND PIQUEMAL, F., *The SQUID Handbook* (Wiley-VCH, Weinheim, 2006).

[18] ENSS, C., *Cryogenic particle detection*, Topics in applied physics (Springer, 2005).

[19] NIELSEN, M. AND CHUANG, I., *Quantum Computation and Quantum Information*, Cambridge Series on Information and the Natural Sciences (Cambridge University Press, 2000).

[20] SEDRA, A. S. AND SMITH, K. C., *Microelectronic circuits*, vol. 1 (New York: Oxford University Press, 1998).

[21] PALADINO, E., FAORO, L., FALCI, G., AND FAZIO, R., *Decoherence and* $1/f$ *noise in josephson qubits*. Physical Review Letters **88** (2002) 228304. URL http://link.aps.org/doi/10.1103/PhysRevLett.88.228304.

[22] DEVORET, M. H., WALLRAFF, A., AND MARTINIS, J. M., *Superconducting qubits: A short review*. arXiv preprint cond-mat/0411174 (2004). URL http://arxiv.org/abs/cond-mat/0411174.

[23] CLARKE, J. AND WILHELM, F. K., *Superconducting quantum bits*. Nature **453** (2008) 1031–1042. URL http://dx.doi.org/10.1038/nature07128.

[24] GENG, Z., *Development of an inductive NIS thermometer* (University of Jyväskylä, 2012). URL http://urn.fi/URN:NBN:fi:jyu-201201301102.

[25] REIF, F., *Fundamentals of statistical and thermal physics, 1965*. McGrawHill Book Company, New York .

[26] PEKOLA, J. P., MAISI, V. F., KAFANOV, S., CHEKUROV, N., KEMPPINEN, A., PASHKIN, Y. A., SAIRA, O.-P., MÖTTÖNEN, M., AND TSAI, J. S., *Environment-assisted tunneling as an origin of the dynes density of states*. Physical Review Letters **105** (2010) 026803. URL http://link.aps.org/doi/10.1103/PhysRevLett.105.026803.

[27] DYNES, R. C., NARAYANAMURTI, V., AND GARNO, J. P., *Direct measurement of quasiparticle-lifetime broadening in a strong-coupled superconductor*. Physical Review Letters **41** (1978) 1509–1512. URL http://link.aps.org/doi/10.1103/PhysRevLett.41.1509.

[28] DYNES, R. C., GARNO, J. P., HERTEL, G. B., AND ORLANDO, T. P., *Tunneling study of superconductivity near the metal-insulator transition*. Physical Review Letters **53** (1984) 2437–2440. URL http://link.aps.org/doi/10.1103/PhysRevLett.53.2437.

[29] HEKKING, F. W. J. AND NAZAROV, Y. V., *Subgap conductivity of a superconductor–normal-metal tunnel interface*. Pysical Review B **49** (1994) 6847–6852. URL http://link.aps.org/doi/10.1103/PhysRevB.49.6847.

[30] FAIVRE, T., GOLUBEV, D. S., AND PEKOLA, J. P., *Andreev current for low temperature thermometry*. Applied Physics Letters **106** (2015) 182602. URL http://scitation.aip.org/content/aip/journal/apl/106/18/10.1063/1.4919892.

[31] ROUKES, M. L., FREEMAN, M. R., GERMAIN, R. S., RICHARDSON, R. C., AND KETCHEN, M. B., *Hot electrons and energy transport in metals at millikelvin temperatures*. Physical Review Letters **55** (1985) 422–425. URL http://link.aps.org/doi/10.1103/PhysRevLett.55.422.

[32] DUZER, T. V. AND TURNER, C. W., *Principles of Superconductive Devices and Circuits, (Second Ed.)* (Prentice Hall PTR, Upper Saddle River, NJ, USA, 1999).

[33] CHAUDHURI, S. AND MAASILTA, I. J., *Superconducting tantalum nitride-based normal metal-insulator-superconductor tunnel junctions*. Applied Physics Letters **104** (2014) 122601. URL http://scitation.aip.org/content/aip/journal/apl/104/12/10.1063/1.4869563.

[34] ULLOM, J. N. AND FISHER, P. A., *Quasiparticle behavior in tunnel junction refrigerators*. Physica B Condensed Matter **284** (2000) 2036–2038. URL http://adsabs.harvard.edu/abs/2000PhyB..284.2036U.

[35] O'NEIL, G. C., LOWELL, P. J., UNDERWOOD, J. M., AND ULLOM, J. N., *Measurement and modeling of a large-area normal-metal/insulator/superconductor refrigerator with improved cooling*. Physical Review B **85** (2012) 134504. URL http://link.aps.org/doi/10.1103/PhysRevB.85.134504.

[36] KOPPINEN, P. J. AND MAASILTA, I. J., *Phonon cooling of nanomechanical beams with tunnel junctions*. Physical Review Letters **102** (2009) 165502. URL http://link.aps.org/doi/10.1103/PhysRevLett.102.165502.

[37] CHAUDHURI, S. AND MAASILTA, I. J., *Cooling, conductance, and thermometric performance of nonideal normal metal-superconductor tunnel junction pairs*. Physical Review B **85** (2012) 014519. URL http://link.aps.org/doi/10.1103/PhysRevB.85.014519.

[38] KARVONEN, J. T. AND MAASILTA, I. J., *Influence of phonon dimensionality on electron energy relaxation*. Physical Review Letters **99** (2007) 145503. URL http://link.aps.org/doi/10.1103/PhysRevLett.99.145503.

[39] FISHER, P. A., ULLOM, J. N., AND NAHUM, M., *High-power on-chip microrefrigerator based on a normal- metal/insulator/superconductor tunnel junction*. Applied Physics Letters **74** (1999) 2705–2707. URL http://scitation.aip.org/content/aip/journal/apl/74/18/10.1063/1.123943.

[40] KOGAN, S., *Electronic Noise and Fluctuations in Solids* (Cambridge University Press, 1996). Cambridge Books Online, URL http://dx.doi.org/10.1017/CBO9780511551666.

[41] MOTCHENBACHER, C. AND CONNELLY, J., *Low noise electronic system design* (J. Wiley & Sons, 1993).

[42] STEINBACH, A. H., MARTINIS, J. M., AND DEVORET, M. H., *Observation of hot-electron shot noise in a metallic resistor*. Physical Review Letters **76** (1996) 3806–3809. URL http://link.aps.org/doi/10.1103/PhysRevLett.76.3806.

[43] ROGOVIN, D. AND SCALAPINO, D. J., *Fluctuation phenomena in tunnel junctions*. Annals of Physics **86** (1974) 1–90. URL http://adsabs.harvard.edu/abs/1974AnPhy..86....1R.

[44] *Scholarperdia: 1/f noise* URL http://www.scholarpedia.org/article/1/f_noise.

[45] MARTINIS, J. M., COOPER, K. B., MCDERMOTT, R., STEFFEN, M., ANSMANN, M., OSBORN, K. D., CICAK, K., OH, S., PAPPAS, D. P., SIMMONDS, R. W., AND YU, C. C., *Decoherence in josephson qubits from dielectric loss*. Physical Review Letters **95** (2005) 210503. URL http://link.aps.org/doi/10.1103/PhysRevLett.95.210503.

[46] JULIN, J. K., KOPPINEN, P. J., AND MAASILTA, I. J., *Reduction of low-frequency 1/f noise in Al-AlO$_x$-Al tunnel junctions by thermal annealing*. Applied Physics Letters **97** (2010) 152501 (pages 3). URL http://link.aip.org/link/?APL/97/152501/1.

[47] JULIN, J., *Reducing 1/f noise in Al-AlOx-Al tunnel junctions by thermal annealing* (University of Jyväskylä, 2009). URL http://urn.fi/URN:NBN:fi:jyu-200910053963.

[48] SCOFIELD, J. H., *ac method for measuring low-frequency resistance fluctuation spectra*. Review of Scientific Instruments **58** (1987) 985–993. URL http://scitation.aip.org/content/aip/journal/rsi/58/6/10.1063/1.1139587.

[49] COSENS, C. R., *A balance-detector for alternating-current bridges*. Proceedings of the Physical Society **46** (1934) 818. URL http://stacks.iop.org/0959-5309/46/i=6/a=310.

[50] MICHELS, W. C. AND CURTIS, N. L., *A pentode lock-in amplifier of high frequency selectivity*. Review of Scientific Instruments **12** (1941) 444–447. URL http://scitation.aip.org/content/aip/journal/rsi/12/9/10.1063/1.1769919.

[51] NIEMEYER, J., *Eine einfache methode zur herstellung kleinster josephson-elemente*. Physikalisch-Technische Bundesanstalt Mitteilungen **84** (1974) 251–253.

[52] DOLAN, G. J., *Offset masks for lift-off photoprocessing*. Applied Physics Letters **31** (1977) 337–339. URL http://scitation.aip.org/content/aip/journal/apl/31/5/10.1063/1.89690.

[53] GURVITCH, M., WASHINGTON, M. A., AND HUGGINS, H. A., *High quality refractory josephson tunnel junctions utilizing thin aluminum layers*. Applied Physics Letters **42** (1983) 472–474. URL http://scitation.aip.org/content/aip/journal/apl/42/5/10.1063/1.93974.

[54] GOVENIUS, J., LAKE, R. E., TAN, K. Y., PIETILÄ, V., JULIN, J. K., MAASILTA, I. J., VIRTANEN, P., AND MÖTTÖNEN, M., *Microwave nanobolometer based on proximity josephson junctions*. Physical Review B **90** (2014) 064505. URL http://link.aps.org/doi/10.1103/PhysRevB.90.064505.

[55] NEVALA, M., *Development of niobium-based superconducting junctions* (University of Jyväskylä, 2012). URL http://urn.fi/URN:ISBN:978-951-39-4789-7.

[56] HOUWMAN, E. P., VELDHUIS, D., FLOKSTRA, J., AND ROGALLA, H., *Fabrication and properties of nb/al, alox/nb josephson tunnel junctions with a double oxide barrier*. Journal of Applied Physics **67** (1990) 1992–1994. URL http://scitation.aip.org/content/aip/journal/jap/67/4/10.1063/1.345579.

[57] HOLMQVIST, T., MESCHKE, M., AND PEKOLA, J. P., *Double oxidation scheme for tunnel junction fabrication*. Journal of Vacuum Science & Technology B **26** (2008) 28–31. URL http://scitation.aip.org/content/avs/journal/jvstb/26/1/10.1116/1.2817629.

[58] TAN, E., MATHER, P. G., PERRELLA, A. C., READ, J. C., AND BUHRMAN, R. A., *Oxygen stoichiometry and instability in aluminum oxide tunnel barrier layers*. Physical Review B **71** (2005) 161401. URL http://link.aps.org/doi/10.1103/PhysRevB.71.161401.

[59] OH, S., CICAK, K., MCDERMOTT, R., COOPER, K. B., OSBORN, K. D., SIMMONDS, R. W., STEFFEN, M., MARTINIS, J. M., AND PAPPAS, D. P., *Low-leakage superconducting tunnel junctions with a single-crystal al 2 o 3 barrier*. Superconductor Science and Technology **18** (2005) 1396. URL http://stacks.iop.org/0953-2048/18/i=10/a=026.

[60] OH, S., CICAK, K., KLINE, J. S., SILLANPÄÄ, M. A., OSBORN, K. D., WHITTAKER, J. D., SIMMONDS, R. W., AND PAPPAS, D. P., *Elimination of two level fluctuators in superconducting quantum bits by an epitaxial tunnel barrier*. Physical Review B **74** (2006) 100502. URL http://link.aps.org/doi/10.1103/PhysRevB.74.100502.

[61] BARENDS, R., KELLY, J., MEGRANT, A., SANK, D., JEFFREY, E., CHEN, Y., YIN, Y., CHIARO, B., MUTUS, J., NEILL, C., O'MALLEY, P., ROUSHAN, P., WENNER, J., WHITE, T. C., CLELAND, A. N., AND MARTINIS, J. M., *Coherent josephson qubit suitable for scalable quantum integrated circuits*. Physical Review Letters **111** (2013) 080502. URL http://link.aps.org/doi/10.1103/PhysRevLett.111.080502.

[62] KOPPINEN, P. J., VÄISTO, L. M., AND MAASILTA, I. J., *Complete stabilization and improvement of the characteristics of tunnel junctions by thermal annealing*. Applied Physics Letters **90** (2007) 053503. URL http://dx.doi.org/10.1063/1.2437662.

[63] LOUNASMAA, O., *Experimental principles and methods below 1 K* (Academic press, 1974).

[64] NUGROHO, C. D., ORLYANCHIK, V., AND VAN HARLINGEN, D. J., *Low frequency resistance and critical current fluctuations in al-based josephson junctions*. Applied Physics Letters **102** (2013) 142602. URL http://scitation.aip.org/content/aip/journal/apl/102/14/10.1063/1.4801521.

[65] EROMS, J., VAN SCHAARENBURG, L. C., DRIESSEN, E. F. C., PLANTENBERG, J. H., HUIZINGA, C. M., SCHOUTEN, R. N., VERBRUGGEN, A. H., HARMANS, C. J. P. M., AND MOOIJ, J. E., *Low-frequency noise in Josephson junctions for superconducting qubits*. Applied Physics Letters **89** (2006) 122516. URL http://adsabs.harvard.edu/abs/2006ApPhL..89l2516E.

[66] LAITINEN, M., ROSSI, M., JULIN, J., AND SAJAVAARA, T., *Time-of-flight energy spectrometer for elemental depth profiling jyvaskyla design*. Nuclear Instruments and Methods in Physics Research Section B: Beam Interactions with Materials and Atoms **337** (2014) 55 – 61. URL http://www.sciencedirect.com/science/article/pii/S0168583X14006284.

[67] O'NEIL, G. C., SCHMIDT, D. R., TOMLIN, N. A., AND ULLOM, J. N., *Quasiparticle density of states measurements in clean superconducting almn alloys*. Journal

of Applied Physics **107** (2010) 093903. URL http://scitation.aip.org/content/aip/journal/jap/107/9/10.1063/1.3369280.

[68] HEBARD, A. F. AND FULTON, T. A., *Josephson junctions in transverse magnetic fields*. Physical Review Letters **35** (1975) 1310–1311. URL http://link.aps.org/doi/10.1103/PhysRevLett.35.1310.

[69] UCHIDA, N., ENPUKU, K., MATSUGAKI, Y., TOMITA, S., IRIE, F., AND YOSHIDA, K., *Flux trapping in josephson tunnel junctions*. Journal of Applied Physics **54** (1983) 5287–5292. URL http://scitation.aip.org/content/aip/journal/jap/54/9/10.1063/1.332704.

[70] NEVALA, M. R., CHAUDHURI, S., HALKOSAARI, J., KARVONEN, J. T., AND MAASILTA, I. J., *Sub-micron normal-metal/insulator/superconductor tunnel junction thermometer and cooler using nb*. Applied Physics Letters **101** (2012) 112601. URL http://scitation.aip.org/content/aip/journal/apl/101/11/10.1063/1.4751355.

[71] TOPPARI, J. J., KÜHN, T., HALVARI, A. P., KINNUNEN, J., LESKINEN, M., AND PARAOANU, G. S., *Cooper-pair resonances and subgap coulomb blockade in a superconducting single-electron transistor*. Physical Review B **76** (2007) 172505. URL http://link.aps.org/doi/10.1103/PhysRevB.76.172505.

[72] DOLATA, R., SCHERER, H., ZORIN, A. B., AND NIEMEYER, J., *Single-charge devices with ultrasmall nb/alox/nb trilayer josephson junctions*. Journal of Applied Physics **97** (2005) 054501. URL http://scitation.aip.org/content/aip/journal/jap/97/5/10.1063/1.1855399.

[73] WATANABE, M., NAKAMURA, Y., AND TSAI, J.-S., *Circuit with small-capacitance high-quality nb josephson junctions*. Applied Physics Letters **84** (2004) 410–412. URL http://scitation.aip.org/content/aip/journal/apl/84/3/10.1063/1.1640798.

[74] FAORO, L. AND IOFFE, L. B., *Microscopic origin of critical current fluctuations in large, small, and ultra-small area josephson junctions*. Physical Review B **75** (2007) 132505. URL http://link.aps.org/doi/10.1103/PhysRevB.75.132505.

[75] KARADY, G. AND HOLBERT, K., *Electrical Energy Conversion and Transport: An Interactive Computer-Based Approach*, IEEE Press Series on Power Engineering (Wiley, 2013).

[76] VAN HARLINGEN, D. J., ROBERTSON, T. L., PLOURDE, B. L. T., REICHARDT, P. A., CRANE, T. A., AND CLARKE, J., *Decoherence in josephson-junction qubits due to critical-current fluctuations*. Physical Review B **70** (2004) 064517. URL http://link.aps.org/doi/10.1103/PhysRevB.70.064517.

[77] MARTINIS, J. M., NAM, S., AUMENTADO, J., LANG, K. M., AND URBINA, C., *Decoherence of a superconducting qubit due to bias noise*. Physical Review B **67** (2003) 094510. URL http://link.aps.org/doi/10.1103/PhysRevB.67.094510.

[78] AMBEGAOKAR, V. AND BARATOFF, A., *Tunneling between superconductors*. Physical Review Letters **10** (1963) 486–489. URL http://link.aps.org/doi/10.1103/PhysRevLett.10.486.

[79] DELIN, K. A. AND KLEINSASSER, A. W., *Stationary properties of high-critical-temperature proximity effect josephson junctions*. Superconductor Science and Technology **9** (1996) 227. URL http://stacks.iop.org/0953-2048/9/i=4/a=001.